

UC Berkeley

UC Berkeley Electronic Theses and Dissertations

Title

Development of a Small Unmanned Aerial System Composed of Structural Pulse Shape Discriminating Plastic Scintillators

Permalink

<https://escholarship.org/uc/item/8bs5w7q6>

Author

Bondin, Michael

Publication Date

2023

Peer reviewed|Thesis/dissertation

Development of a Small Unmanned Aerial System Composed of Structural Pulse Shape
Discriminating Plastic Scintillators

By

Michael Bondin

A dissertation submitted in partial satisfaction of the

requirements for the degree of

Doctor of Philosophy

in

Engineering – Nuclear Engineering

in the

Graduate Division

of the

University of California, Berkeley

Committee in charge:

Professor Kai Vetter, Chair

Professor Karl van Bibber

Professor Edward Morse

Summer 2023

Development of a Small Unmanned Aerial System Composed of Structural Pulse Shape
Discriminating Plastic Scintillators

Copyright 2023
by
Michael Bondin

Abstract

Development of a Small Unmanned Aerial System Composed of Structural Pulse Shape Discriminating Plastic Scintillators

by

Michael Bondin

Doctor of Philosophy in Engineering – Nuclear Engineering

University of California, Berkeley

Professor Kai Vetter, Chair

In this work, the feasibility of utilizing a new generation of pulse shape discriminating plastic scintillators as structural materials is evaluated. The capacity to employ radiation detectors in structural roles provides potential advantages in mass-constrained and volume-constrained systems. This technology is particularly applicable to mobile-platform deployed detection payloads in which layouts can be augmented either by the addition of radiation detectors into currently incompatible placements and orientations, or through the replacement of inert structural mass by active-volume structural detector components. Additionally, the development of such materials enables the construction of payload-less radiation-detecting small unmanned aerial systems (sUASs), allowing for the miniaturization and consequent reduction of minimum source-detector measurement distances beyond currently achievable means.

This work describes the design, construction, and evaluation of a payload-less radiation-mapping sUAS, originating with the development of novel PSD plastic scintillators suitable for use in the intended structural application. A comprehensive study of the PSD and mechanical properties of novel scintillator compositions, in collaboration with Lawrence Livermore National Laboratory, is described. Detector design is accomplished by simulation of complex active-volume sUAS frame geometries in GEANT4 optimizing light collection efficiency and detection efficiency, followed by experimental validation. Following computational modeling of optimal structural detector geometries, experimental active-volume sUAS frames were fabricated from which complete sUAS prototypes were constructed demonstrating semi-autonomous flight capability and onboard PSD spectroscopy. A series of prototypes was constructed, initially to prove structural feasibility in a 19 inches diameter, 2kg mass configuration, and subsequently improved upon to demonstrate PSD capability. The end result is the construction of a radiation-detecting sUAS constructed of four PSD plastic active-volume frame arms, with an overall diameter of 12 inches and approximately 1kg system dry mass. Proximity radiation mapping performance of the constructed systems was

evaluated in γ -ray and neutron source localization field tests.

To my parents,
my brother Natan,
my loving girlfriend Kalie,
and my boy, Enrico Fermi.

Contents

Contents	ii
List of Figures	v
List of Tables	x
1 Introduction	1
1.1 Proposed solution	2
1.2 Applications	3
2 Background	4
2.1 Detectable Signatures of Interest	4
2.1.1 γ -rays	4
2.1.2 Neutrons	5
2.2 Scintillation Detectors	5
2.2.1 Plastic Scintillators	6
2.2.2 Scintillator Readout	7
2.3 Radiation Detection Theory of Plastic Scintillators	9
2.3.1 γ -Ray Detection	9
2.3.2 Fast Neutron Detection	10
2.3.3 Thermal Neutron Detection	11
2.3.4 PSD	11
2.4 PSD Method	13
2.4.1 Tail Fraction Integration	13
2.4.2 Energy Calibration	18
2.4.3 Time-Invariant Pulse Shaping	19
2.5 Structural Plastic Scintillators	19
2.6 Aerial Radiation Detection	20
2.6.1 Source Localization Methods	20
2.7 Scientific Hypothesis	21
3 Evaluation of PSD Plastic Compositions	22

3.1	Target Requirements	22
3.1.1	PSD Capability	23
3.1.2	Mechanical Requirements	23
3.1.3	Proof-of-Concept sUAS Structural Component Replacement	24
3.1.4	Dynamic Stress Simulation	25
3.2	Materials	26
3.3	PSD Characterization	28
3.3.1	PSD Characterization Results	32
3.4	Mechanical Properties Evaluation	37
3.4.1	Methods	38
3.4.2	Mechanical Evaluation Results	39
3.4.3	Curing Conditions	42
3.5	Analysis of Results	43
3.6	Proof-of-Concept Experimental Component Replacement	45
4	Simulation-informed Geometric Evaluation	48
4.1	Model Construction	48
4.2	Experimental Validation	52
4.2.1	Measurements - Uncollimated	52
4.2.2	Collimated Model Validation	56
4.3	Optimal Shape Determination	58
5	sUAS Construction	65
5.1	Active Frame Fabrication	65
5.2	Detection Electronics, Associated Circuitry, and Data Communication	69
5.3	Power, Propulsion, and Flight Control	70
5.3.1	Components	70
5.3.2	Equipment Considerations	72
5.3.3	Thermal Considerations	73
5.4	RF/EMI Mitigation	74
5.4.1	Affected Components and Significance	75
5.4.2	Sources of EMI	76
5.4.3	Mitigation	76
6	Detection Circuitry and Data Communication	79
6.1	Biasing	79
6.1.1	Step-Down Approach	80
6.1.2	Step-Up Approach	82
6.2	Readout	83
6.2.1	Peripheral SiPM Boards	84
6.2.2	Signal Series Summation	84
6.2.3	Signal-Driven Multiplexing	84

6.3	Signal Processing	86
6.3.1	nanoPSD Parameters	87
6.4	Electronics Wiring	88
6.5	Data Communication	90
6.5.1	Raspberry Pi - nanoPSD Communication	90
6.5.2	Raspberry Pi - Pixhawk Cube Communication	96
6.5.3	Raspberry Pi - Ground Station Communication	98
7	Measurements	101
7.1	Initial Prototype Field Measurements	101
7.1.1	Setup and Configuration	103
7.1.2	Safety	103
7.2	Initial Prototype Field Measurement	104
7.2.1	Field Measurement Results	105
7.3	Analysis Techniques	108
7.4	Performance assessment	109
7.4.1	Initial Prototype	109
7.5	Second-Generation Prototype	112
7.5.1	Laboratory measurements	114
7.6	Discussion	118
8	Concluding Remarks	120
	Bibliography	122

List of Figures

2.1	Chemical structures of common primary fluors PPO (left) and p-terphenyl (right) demonstrating aromatic ring structure	7
2.2	Logarithmic plot depicting the dominant γ -ray interaction mode as a function of atomic number (Z) and incident γ -ray energy in MeV [6]	10
2.3	Electron energy levels diagram for an organic molecule with π -electron orbitals, depicting excited singlet ($S_1, S_2, S_3\dots$) and triplet ($T_1, T_2, T_3\dots$) states, as well as vibrational sub-levels ($S_{11}, S_{12}\dots$) [10]	12
2.4	Plot comparison of sample 1 MeVee γ -ray and neutron SiPM signal pulse shape differences collected for PuBe-emitted radiation detected by a SiPM-coupled PSD plastic scintillator (Table 3.3 composition V)	13
2.5	Plot of raw digitized SiPM pulse waveform of a ^{137}Cs -emitted γ -ray interaction in a SiPM-coupled PSD plastic scintillator (Table 3.3 composition V) in ADC units as a function of sample number (left), and voltage as a function of sample relative time (right)	14
2.6	Histogram and corresponding double Gaussian fit of calculated tail pulse fraction values for detected signal pulses of PuBe-emitted γ -ray and fast neutron interactions of 475 ± 75 keVee energy deposition in a SiPM-coupled PSD plastic scintillator (Table 3.3 composition V)	15
2.7	Histograms of tail pulse fraction values and associated FOMs for three separate interaction energy ranges of signal waveforms collected during a single measurement of PuBe-emitted radiation by a SiPM-coupled PSD plastic scintillator (Table 3.3 composition V)	16
2.8	Histogram of tail pulse fraction values, demonstrating pronounced thermal neutron capture “hump”, for signal waveforms of recorded interaction energies within 450 ± 50 keVee of PuBe-emitted radiation by an SiPM-coupled ^6Li -doped PSD plastic scintillator (Table 3.2 composition B)	17
2.9	2-dimensional contour plot of tail pulse fraction values as a function of energy for signal waveforms collected during a measurement of PuBe-emitted radiation by a SiPM-coupled ^6Li -doped PSD plastic scintillator (Table 3.3 composition B)	18
3.1	Schematic of DJI Matrice 600 flying platform with landing gear replaced by a structural scintillator rod in blue (associated detection equipment not depicted) [26]	25

3.2	SolidWorks dynamic simulation depicting locations of sustained mechanical stress by structural PSD plastic scintillator landing gear induced in scenarios of level landing (left) and uneven landing with initial ground contact on landing foot corner (right) [27]	26
3.3	Photo of selected evaluated compositions, in order from left to right: J*, I, D, F, V, K*, L*, M*, N*, O*, C**	27
3.4	Photo of experimental setup for PSD evaluation of 1" cylindrical compositions	30
3.5	Energy calibration of SiPM-coupled PSD plastic scintillator (Table 3.3 composition V), with Compton edge peak channel marked by right-facing triangle, Compton edge half-maximum channel marked by left-facing triangle, and estimated true Compton edge channel marked by the letter 'X'.	31
3.6	Plot of calculated PSD FOM values as a function of solvent matrix PS percentage for evaluated compositions. Filled markers indicate ⁶ Li doping.	34
3.7	Fig. 3.6 with axes bounds focusing on cluster of compositions at 65-95% PS. Filled markers indicate ⁶ Li doping.	35
3.8	Generated PSD plots for compositions A (left) and B (right)	35
3.9	Generated PSD plots for compositions P (left) and F (right)	36
3.10	Plot of calculated PSD FOM values as a function of curing time, in hours, for curing effects evaluation samples K*-O*. Oven temperature over time is indicated by the horizontal bar above the horizontal axis, with the region between 0 and 3 hours representing the oven warming period from 60°to 75°C	37
3.11	Schematic of SSJ tensile-testing sample geometry machining blueprint; dimensions in millimeters	38
3.12	Birds-eye view of tensile/compression module containing SSJ sample of PSD plastic scintillator at its center prior to pulling	38
3.13	Plot of sample σ - ϵ curve of an evaluated PSD plastic SSJ sample (Composition H) demonstrating 0.02%-offset σ_y determination method	39
3.14	Plot of measured σ_y values in MPa as a function of PS solvent matrix percentage of evaluated compositions. Marker shape and fill are as described for Fig. 3.6	41
3.15	Fig. 3.14 with axes bounds focusing on cluster of compositions at 65-95% PS	41
3.16	Plot of measured Young's Modulus, in GPa, as a function of yield strength, in MPa, of evaluated compositions depicting a strong linear relationship. Marker shape and fill are as described for Fig. 3.6	42
3.17	Plots of measured σ_y values in MPa (left) and measured E values in GPa (right) as a function of curing time in hours for curing effects evaluation samples K*-O*. Oven temperature over time is indicated by the horizontal bar above the horizontal axis, with the region between 0 and 3 hours representing the oven warming period from 60°to 75°C	43
3.18	Plot of calculated PSD FOM values as a function of σ_y in MPa of evaluated compositions; separated into four quadrants by dashed lines horizontally at FOM = 1.27 and vertically at $\sigma_y = 30$ MPa. Marker shape and fill are as described for Fig. 3.6	44

3.19	Photos of LBNL operated DJI Matrice 600 sUAS platform depicting the replacement of a landing foot with a structural PSD plastic detector assembly (left, center), as well as the replacement of the second carbon-fiber foot with a PMMA 16" long 1" x 1" square rod (right)	46
4.1	GEANT4 extended optical example <i>LXe</i> , depicting simulated scintillation photon tracks (green) generated by a primary particle (blue) interaction	49
4.2	GEANT4 G4UnionSolid volume simulating a PSD plastic scintillator with three geometrically-adjustable sections	49
4.3	Eljen EJ-276 and EJ-276G (green-shifted) PSD plastic scintillation photon emission spectra	50
4.4	Spectrum of simulated energy depositions of Compton scattering interaction events in a PSD plastic scintillator volume, depicting 478 keV Compton edge	51
4.5	Photo of polished GEANT4 model validation experimental scintillator geometries	52
4.6	PSD Plots of 100 cm × 35 cm × 35 cm PSD plastic scintillator unaltered rectangular prism (left) and 45° 4-sided readout face taper (right) configurations . .	53
4.7	PSD Plots of 100 cm elongated frustum tapering configuration for SiPM coupled at tapered face (left) and frustum base (right)	54
4.8	Simulated elongated frustum geometry in GEANT4 demonstrating reflection of scintillation photons toward the untapered base	54
4.9	Comparison of simulated (dashed line) and experimental (solid line) ¹³⁷ Cs energy spectra for the three model validation PSD plastic scintillator geometries, using a fixed ADC conversion factor	55
4.10	Simulated elongated frustum collimated beam rotation	57
4.11	Comparison of simulated and experimental ¹³⁷ Cs spectra at collimated positions of 10% and 90% of the scintillator length from the photocathode, for 45° taper configuration	57
4.12	Comparison of simulated and experimental ¹³⁷ Cs spectra at collimated positions of 10% and 90% of the scintillator length from the photocathode for 45° taper configuration, with noise added to the simulated spectra	58
4.13	CAD model of DJI F450 sUAS platform [34]	59
4.14	Example simulated configurations of 45° readout face taper (top), 45° taper of scintillator end opposite the readout face (middle), and dual taper with junction at 40% scintillator length from the photocathode (bottom)	60
4.15	Plot of simulated LCE as a function of photocathode face tapering angle, with error bars representing LCE uniformity	61
4.16	Plot of simulated LCE as a function of tapering angle of face opposing photocathode, with error bars representing LCE uniformity	61
4.17	Plot of simulated LCE as a function of dual-ended tapering junction position, with error bars representing LCE uniformity	62
4.18	Optimized sUAS structural component scintillator geometry	63

5.1	Left: Photo of bulk scintillator material block, composition 1. Center: Photo of bulk scintillator material block, composition 2. Right: Photo of bulk scintillator material block, composition 1, illuminated by UV lamp.	66
5.2	Left: Photo of bulk scintillator material block (composition 2) in preparation for bandsaw cuts. Right: 1.5" × 1.5" × 9.5" cut sections	66
5.3	Left: Photo of PSD plastic cut to structural sUAS component geometry. Right: Photo of drill pressing motor bolt holes into PSD plastic scintillator component	67
5.4	Polished PSD plastic structural sUAS components	68
5.5	Polished PSD plastic structural sUAS components	68
5.6	Photo of optically-sealed PSD plastic structural sUAS component assembly	69
5.7	Photo of spectrometer location at sUAS center, with non-scintillator plastic frame arms for prototyping	70
5.8	Exploded component diagram of sUAS vertical center stack arrangement	72
5.9	Photo of assembled sUAS with RFD900x telemetry module in the foreground	78
6.1	ULLDO SiPM biasing circuit diagram, providing four Vbias outputs	80
6.2	Fabricated ULLDO 29.5V output SiPM bias supply used in laboratory bench-testing	81
6.3	Plot comparison of collected ¹³⁷ Cs energy spectra by a SiPM-coupled PSD plastic scintillator, biased using the fabricated ULLDO and a benchtop power supply	81
6.4	Start-up output voltage curve for ULLDO powered by Tenma 72-6905 benchtop power supply (voltage not to scale).	82
6.5	Circuit diagram of 5V-29.5V step-up SiPM bias voltage source, utilizing a MAX5026 buck/boost DC-DC converter	83
6.6	Circuit diagram of signal-driven multiplexing implemented for readout of the four structural-scintillator sUAS frame arm SiPMs	85
6.7	Example screenshot of labZY analysis software	87
6.8	Organizational diagram of inter-component communication for the constructed sUAS	89
6.9	Photo of Raspberry Pi Zero 2 W soldered TELEM cable GPIO connections	89
6.10	Terminal output of <i>lsusb</i> command for nanoPSD connected to micro USB	91
6.11	labZY Device Response to Host Write Command structure [42]	93
6.12	Terminal output of <code>sudo dmesg — grep tty*</code> command	95
6.13	Raspberry Pi Zero 2 W Terminal output displaying enabled GPIO serial port 1	97
6.14	Terminal output following successful MAVLink 2 connection to the flight controller using mavproxy	98
6.15	Structure of assembled data packet depicting the header lines and initial three channels of a recorded TIPS spectrum	99
7.1	Initial sUAS prototype consisting of 7.5-inch long structural PSD plastic scintillator frame component arms	102
7.2	GEANT4 model of initial sUAS prototype extended-length detector geometry	102

7.3	Screen capture of QGroundControl raster scan automatic course planning tool . . .	103
7.4	Photo of initial prototype field measurement demonstrating the sUAS in flight, with locations depicted of the mixed γ -n source, launch position, LAN router, and RTK base station, from the visual perspective of the GCS.	105
7.5	Plot of detected count rate with respect to relative coordinates position for one-second interval data packets collected during field measurement by constructed initial sUAS prototype	106
7.6	Screen capture of measurement path recorded by the sUAS flight controller . . .	107
7.7	Fig. 7.5 overlaid onto 7.6, revealing a count rates distribution concentrated around the true source location	107
7.8	Standard MLEM reconstruction of measured position-dependent detected radiation counts by the sUAS. Multiple source hotspots along the measurement path are indicated by the colorized pixel clusters. Measurement points are indicated by the directional vectors, colorized by detected counts	108
7.9	KL-divergence MLEM reconstruction of measured position-dependent detected radiation counts by the sUAS. A prominent source hotspot is indicated by the figure's center pixels. Measurement points are indicated by the directional vectors, colorized by detected counts	109
7.10	Cumulative TIPS spectrum streamed by prototype sUAS at the conclusion of field measurement exercise, indicating lack of separation between γ -ray and neutron TIPS differences	110
7.11	Reconstruction of measured source location predicted by KL-divergence MLEM overlaid onto the measurement flight path plotted on a 2D satellite image of the measured space. The true source location is indicated by the trefoil	111
7.12	Overlaid comparison of the reconstructed source location pixels to the true source location indicated by the trefoil, reference to the measurement path line in red	112
7.13	CAD exploded component diagram of second-generation structural PSD plastic scintillator sUAS configuration	113
7.14	Photograph of second-generation sUAS prototype, composed of 4.5-inch structural PSD plastic frame arm components, in guided flight	114
7.15	Laboratory PSD characterization setup for assembled sUAS	115
7.16	PSD plot of sUAS component arm prior to system assembly	116
7.17	Comparison of simulated and experimental detected energy spectra of uncollimated incident 661.7 keV γ -rays	117
7.18	Comparison of Gaussian-fitted TIPS spectra for laboratory measurements of ^{252}Cf for disarmed sUAS (left) and armed sUAS with applied 50% motor throttle (right)	118

List of Tables

3.1	Table listing reference tensile strength, elastic modulus, and density ranges of common materials used in sUAS construction including aerospace-grade aluminum, extruded acrylonitrile butadiene styrene, nylon 66 30% glass fiber filled, nylon 66 30% carbon fiber filled, and FR-4 G-10 fire-retardant glass-epoxy laminate used in printed circuit boards [20][21][22][23][24]. Values for tensile (Young's) elastic modulus are provided for all materials except G-10, FR-4, for which flexural modulus of elasticity is listed.	24
3.2	Table of evaluated PSD plastic compositions containing PS:PMAA solvent matrix in various proportions as well as their respective primary dye, λ -shifting dye, and ^6Li doping matrix type and content	28
3.3	Table of evaluated PSD plastic compositions containing PS:PMMA solvent matrix in various proportions, as well as their respective primary dye, λ -shifting dye, and ^6Li doping matrix type and content	28
5.1	Compositions of received PSD plastic bulk material for structural sUAS component fabrication	65
5.2	Table containing measured component masses of the constructed sUAS	73
6.1	labZY nanoPSD spectrometer PSA Tab Parameters calibrated for constructed sUAS	88
6.2	Table of rated power draws of constructed sUAS peripherals powered by Pixhawk Cube carrier board	90
6.3	Structure of intercepted 9-byte RX message payload	92

Acknowledgments

I would like to thank my academic advisor Professor Kai Vetter for your endless support, unconditional kindness, and encouragement to develop my sense of creativity through science.

Thank you to Professor Karl van Bibber for your guidance and dedication to my academic success, and to Professor Ed Morse for your valuable lessons communicated through a uniquely real-world perspective.

I owe my gratitude to Dr. Natalia Zaitseva for your invaluable commitment to ensuring I have the means to turn my ideas into reality, as well as to Dr. Michael Ford for your close collaboration and to the late Dr. Andrew Mabe for building the foundations of our work.

I would like to thank Dr. Valentin Jordanov for your generosity and aid enabling the continuation of my research through the most uncertain times, and Dr. Radoslav Radev for your mentorship and friendship.

Thank you to Dr. Alan Bolind, Jeff Bickel, Dr. Justin Ellin, and AJ Gubser for your mentorship in developing my skills as an experimentalist, and to Raymon Cheng, Ivan Cho, Jessica Elder, Nolan Kowitt, Jaewon Lee, Mark Ma, Shubham Mandot, Arthur Shurley, and Alec Zerza for your extensive contributions through all stages of this endeavor.

Finally, I would like to extend a special thank you to Dr. Grey Batie, Dr. Aaron Berliner, Alex Christensen, Alex Droster, Dr. Dinara Ermakova, Jake Hecla, Dr. Austin Mullen, and Andrew Scott for your close companionship and the cherished memories defining our graduate school years.

Chapter 1

Introduction

In the 21st century, humanity has found itself increasingly exposed to nuclear and radiological hazards. Amid high-profile radiological environmental releases such as the Fukushima accident, rising international nuclear tensions including the revival of nuclear weapons testing by North Korea, and damage to the Chernobyl Exclusion Zone and the Zaporizhzhia Nuclear Power Plant by the continuing Russian occupation of Ukraine, the necessity for accurate and efficient mapping of unknown radiological hazards has become a forefront of nuclear research. Research and development into creating tools to meet this demand has become a multidisciplinary endeavor, synthesizing the fields of radiation detection, robotics, computer science, and electrical and mechanical engineering. This has led to the availability of a variety of specialized equipment intended to identify and localize the presence of radioactive isotopes in a wide range of environments and missions, taking various forms such as handheld, backpack-carried, and vehicle-deployed devices.

Of these varied means for deploying radiation detection equipment in measurement areas, significant interest has been placed on vehicle-deployed radiation detection platforms; particularly unmanned vehicle systems. Unmanned vehicle-deployed radiation mapping systems provide the crucial capability to map radioactivity without the need to expose human operators to radiation dose. These systems can take on many forms as unmanned ground vehicle (UGV) robots or unmanned aerial systems (UASs).

UAS-deployed radiation mapping systems are particularly useful in hazardous or inaccessible areas, due to their excellent maneuverability, ability to approach and measure sources from different angles in three dimensions to allow them to overcome the inverse-square law of radiation intensity, and relative safety from ground contamination. Due to the rapid advancement of novel radiation detectors and cost-effective commercial small unmanned aerial systems (sUASs) with payload-transporting capabilities, the field of aerial radiation detection has rapidly matured over the past decade toward increasingly powerful detection packages aboard increasingly compact aerial platforms maximizing detection capabilities. Today's state-of-the-art systems employ advanced radiation detectors complemented by complex sensor suites and onboard processing capabilities to map radiation source locations onto reconstructed scanned environments, measuring sources from distances of a few meters.

As these systems mature, further optimization becomes dependent on improving the ability to collect more radiation information, either by improving the efficiency, sensitivity, resolution and/or quantity of deployed detectors, or by reducing source-detector distances through technological advancements in compact carrier vehicle platforms. This is a direct result of the fundamental limitation of the maximum takeoff weight (MTOW) of a deployed aerial system. Therefore, optimal configuration of a constructed radiation-detecting sUAS relies on a balance between deployed detection payload mass and the required carrier vehicle size.

1.1 Proposed solution

A recent technological innovation in plastic scintillators has enabled the manufacturing of γ -ray and neutron particle-discriminating materials with mechanical properties similar to conventional plastics, making them potentially utilizable as structural materials [1], [2]. These light-weight materials can be manufactured into complex geometries, making them ideal candidates for use in mass-constrained systems such as highly compact sUASs. One approach of incorporating this advancement into today's systems is by replacing non-detector components with structural detectors. This can manifest as the replacement of inert polyethylene moderators in thermal-neutron detecting systems by γ -ray and fast neutron discriminating plastics to yield "trimodal" particle detection capabilities, or through the incorporation of radiation detectors outside a centralized payload into previously inaccessible configurations. As an example, this could entail replacing a radiation-detecting sUAS' frame components, such as its landing gear, with high-aspect ratio, mechanically capable active detector materials.

More advantageously, the combination of mechanical and radiation detection capabilities of structural detectors can be leveraged to circumvent current limitations preventing the consolidation of radiation-detecting sUASs to enable source-detector distances below one meter. By utilizing radiation detectors as structural components onboard, the currently necessary distinction between detector payload and carrier vehicle is eliminated, and a higher fraction of the MTOW can be dedicated to active detector material.

The fraction of a radiation-detecting system's total mass composed of active detector mass can be termed its *active mass utilization*; with a maximum value of 1 denoting 100% of the system's mass is composed of active detector material.

Through the replacement of "dead" sUAS mass with structural detectors, active mass utilization can be raised beyond currently available means. In addition to allowing more detector mass to be transported by a given sUAS footprint, an increased active mass utilization allows for system form factors previously incapable of transporting sufficient detector payloads to be constructed. By constructing compact systems with high active mass utilization, source-detector measurement distances can be reduced beyond the typical current minimum standoff of several meters.

The reduction of source-detector distances can additionally reduce the complexity of required onboard mapping electronics equipment, further increasing a system's maximum achievable active mass utilization. The reduction of system size and complexity through the use of structural detectors can translate to reduced unit construction and operation cost, as compared with current state-of-the-art high-resolution aerial radiation imaging systems.

1.2 Applications

The technological development of compact, low-cost aerial radiation mapping systems composed of structural scintillators holds promise for use in a variety of applications. As standalone systems, these systems can enable economically-realistic multiple-deployment of low unit-value operation modes. These systems are particularly advantageous for deployment in hazardous areas, providing redundancy and diversification of resources, with potential for single-use operation in environments too contaminated or otherwise hazardous to expect unit recovery.

Radiation-mapping sUASs constructed of structural γ -n discriminating structural detectors may serve as complementary units to higher-value radiation-mapping mobile systems (e.g. aerial, UGV, manned operations) as well, offering initial reconnaissance to efficiently direct resources to areas of interest, identify hazardous areas, or provide additional neutron particle sensitivity for mapping shielded γ -n sources.

Chapter 2

Background

The following chapter provides an overview of scintillation detectors, radiation detection physics and measurement techniques pertaining to organic scintillation detectors, as well as an introduction to radiation mapping and aerial platforms. The concepts discussed in the following sections provide a foundation for understanding the context of the concluding section of this Chapter; Section 2.7. Section 2.7 introduces the scientific hypothesis for this work and defines the metrics for its accomplishment.

2.1 Detectable Signatures of Interest

The objective of radiation mapping of unknown environments is to identify the presence of radioactive isotopes of interest and localize their distributions in space. The presence of radioactive isotopes is not directly detected, but rather informed by characteristic radiation emitted isotropically, known as signatures, from radioactive sources. These signatures can take the form of different types of radiation, such as α particles, β particles, γ -rays, and neutrons, and can be emitted either at distinct known energies - commonly utilized in γ -ray detection for isotope identification - or as a continuous spectrum of energies, for example as observed for neutron emission in fission. When discussing radiation mapping, it is important to establish what signatures are of interest in order to understand the application scope and the capabilities of the detector of choice. In the context of mapping radioactivity of a large area, such as in scenarios of source search, incident response, or contamination remediation, the most common signatures of interest are γ -rays and neutrons.

2.1.1 γ -rays

γ -rays are photons emitted from the nuclei of atoms undergoing radioactive decay at distinct energies. Processes that emit γ -rays do so at distinct energies. As a result, the energy of a γ -ray can serve as a “fingerprint” signature, potentially informing not only of the emitter’s location, but its originating isotope as well. The information provided by these energy

signatures allow for naturally occurring radioactive materials, such as ^{40}K and ^{238}U , to be distinguished from radioactive isotopes of more significant interest, such as ^{137}Cs , ^{241}Am , ^{60}Co , ^{235}U , ^{239}Pu , and ^{240}Pu .

2.1.2 Neutrons

Neutrons are subatomic particles typically present in the nuclei of atoms, possessing a magnetic moment and no electrical charge. As free particles, neutrons have a half-life of approximately 10.2 minutes, and are thus rarely found in nature. Free neutrons detected on Earth are typically created as a result of neutron-producing nuclear reactions, such as $(n,2n)$, (γ,n) , (p,n) , (α,n) , or nuclear fission. Therefore, the detection of neutrons in the environment signifies the presence of materials of high interest, such as special nuclear materials: ^{235}U , ^{233}U or ^{239}Pu , or other human-made neutron sources such as ^{240}Pu , ^{252}Cf , AmBe, PuBe, neutron generators, or nuclear fuel.

2.2 Scintillation Detectors

One of the most commonly employed types of radiation detectors is the scintillation detector. Fundamentally, a scintillation detector is composed of two components: the scintillator - a material which emits light when interacted with by ionizing radiation - and the photodetector - a surface which utilizes the photoelectric effect to convert scintillation light into electrons (ultimately producing an electrical signal). Scintillators can be organic (carbon-based) or inorganic, crystalline or amorphous, solid, liquid, or gaseous, with each variation exhibiting unique physical properties and radiation detection characteristics.

Scintillators are traditionally divided into two major classes: inorganic and organic. Inorganic scintillators are typically composed of single crystals containing elements of high atomic numbers (Z) in ionic bonds, although liquid inorganic scintillators such as liquid xenon exist as well. Scintillation is facilitated through the excitation and subsequent de-excitation of valence electrons by interacting radiation. Inorganic scintillators are primarily used for the detection of γ -ray radiation, but can additionally be employed for neutron detection by the addition of specific isotopes possessing neutron capture reaction cross-sections; emitting heavy charged particles or γ -rays of characteristic energy signatures which can subsequently be detected by the scintillator.

Due to their high average Z , the probability of photoelectric absorption of incident γ -rays is favorable, and thus scintillation light output and resolution are typically relatively high. The most commonly used inorganic scintillator, sodium iodide ($\text{NaI}(\text{Tl})$), has a light output of approximately 40,000 photons/MeV and an energy resolution of 6-8%. Photoelectric absorption of incident γ -rays yields a characteristic full-energy deposition “photopeak” observable in a collected energy spectrum, using which isotope identification can be performed (conditional on the resolution of the detector).

Organic scintillators are composed of low- Z hydrocarbon molecules containing aromatic ring structures. Organic scintillators may be crystalline, plastic, glass, or liquid in nature, although the term “organic scintillator” is colloquially reserved for single-crystal organic scintillators. Scintillation is facilitated through the excitation and subsequent de-excitation of electrons in hybridized orbitals as a result of incident radiation interactions within the active volume. Due to their lower average Z , energy from incident γ -rays is predominantly deposited by Compton scattering interactions, resulting in lower light output and resolution. Anthracene’s light output, the highest achieved by organic scintillators, is 17,400 photons/MeV. Due to the absence of a prominent characteristic photoelectric absorption photopeak, limited isotope identification can be performed using the Compton edge energy of collected energy spectra.

In contrast to disadvantages in γ -ray detection, the low- Z composition of organic scintillators favors the efficient detection of fast neutrons through elastic and inelastic nuclear collisions. This is due to the higher possible transfer of energy, E_{Max} , from an interacting neutron with mass m_n and kinetic energy E_n to the target nucleus of mass M_{target} within the scintillator volume. In the case of an incident neutron on a hydrogen (proton) target, as much as 100% of the neutron’s incident kinetic energy can be transferred (equation 2.1). Examples of organic scintillators include single-crystal stilbene and anthracene, liquid organic scintillators such as Eljen EJ-309, and plastic scintillators such as EJ-201.

$$E_{max} = E_n \times \frac{4M_{target}m_n}{(M_{target} + m_n)^2} \quad (2.1)$$

Some organic scintillators are capable of pulse shape discrimination (PSD); a technique by which interacting radiation of different particle types can be distinguished according to time-dependent differences in emitted scintillation light. This technique is discussed in detail in Section 2.3.

2.2.1 Plastic Scintillators

2.2.1.1 Composition

Plastic scintillators are amorphous organic solids composed of polymerized chains of aromatic molecules, known as fluor or scintillating dye, dissolved in a non-scintillating organic solvent matrix or base [3]. The fluor serves as the primary compound responsible for converting absorbed energy from radiation interactions to fluorescent light, while the solvent matrix serves to provide physical strength, environmental stability, a medium for dissolving other useful compounds, and bulk active volume. A key factor in the effective performance of the scintillator is the efficient transfer of energy deposited by radiation interactions, in the form of excited electrons, from the solvent matrix to the scintillating dye. Commonly used fluors are 2,5-Diphenyloxazole (PPO) and p-terphenyl, with their aromatic molecular structures depicted in Fig. 2.1. Commonly used bases include polystyrene (PS) and polyvinyl-toluene (PVT).

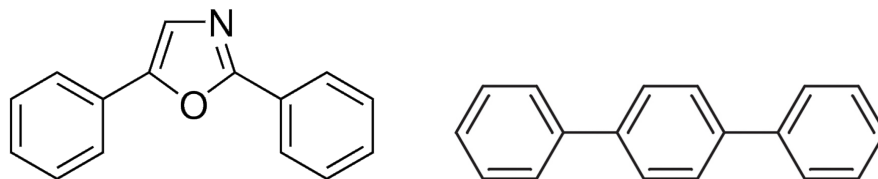


Figure 2.1: Chemical structures of common primary fluors PPO (left) and p-terphenyl (right) demonstrating aromatic ring structure

In addition to the solvent matrix and scintillating dye, other compounds are often added to enhance various physical and optical properties. Among these are wavelength-shifting dyes, thermal neutron absorbing dopants, cross-linking agents, and compounds enhancing optical clarity or resistance to degradation (aging).

Wavelength-shifting dyes, also known as secondary fluors, are employed for the purpose of shifting the emitted scintillation light spectrum of the primary fluor to more closely overlap the absorption spectrum of the photodetector, as well as to increase the attenuation length of scintillation light within the scintillator volume. These compounds function by absorbing and quickly re-emitting at longer wavelengths the scintillation photons produced by the primary fluor.

In addition to wavelength-shifting dyes, doping agents containing thermal neutron absorber isotopes, such as ^6Li and ^{10}B , serve to provide additional sensitivity to thermal neutrons by possessing thermal neutron absorption cross-sections several orders of magnitude greater than the fast neutron scattering cross-sections of hydrogen and carbon.

Cross-linking agents, such as divinylbenzene (DVB), connect polymer chains to provide physical strength and molecular stability.

2.2.1.2 PSD Plastic Scintillators

Conventional plastic scintillators, while sensitive to both γ -ray and neutron radiation interactions, do not possess the ability to distinguish detected radiation by particle type. A recently developed class of plastic scintillators, however, provides this capability through pulse shape discrimination (PSD). Efficient PSD was first achieved in plastic scintillators in 2012 by Zaitseva et al. of Lawrence Livermore National Laboratory; accomplished by significantly increasing the weight concentration of scintillating dye from $<10\%$ to 30% [1]. Prior to this development, PSD was only viable in single-crystal and liquid organic scintillators.

2.2.2 Scintillator Readout

The conversion of produced scintillation light from radiation interaction events into electrical signals measurable by pulse-processing equipment is accomplished in a series of steps by devices known as photodetectors. Two classes of photodetectors are primarily utilized in

scintillator readout: photomultiplier tubes (PMTs) and silicon photomultipliers (SiPMs). In both PMTs and SiPMs, the conversion of incident photons into an electrical signal is performed by the use of a material which utilizes the photoelectric effect to produce free electrons upon the absorption of light. Its performance is characterized by the photocathode intrinsic quantum efficiency for PMTs, and the particle detection efficiency for SiPMs. Electrons (and in the case of SiPMs, electron holes) produced by photoelectric absorption are subjected to an internal electric field sufficiently strong to induce charge carrier migration and avalanche signal multiplication. The signal multiplication process, following electron conversion, is performed differently by PMTs and SiPMs as discussed in the following paragraphs.

2.2.2.1 Photomultiplier Tubes

Photomultiplier tubes, or PMTs, are the traditional equipment class used to convert scintillation light to measurable electrical signal pulses. They are functionally composed of a photocathode paired to a series of electron-multiplying dynode stages. The photocathode surface, protected by a glass screen, is coupled to the scintillator volume using refractive index matching grease or epoxy cement. Free electrons produced by the photocathode are subjected to a strong electric field and accelerated within a sealed vacuum enclosure through a series of dynodes. At each dynode stage, the kinetic energy of the accelerated electrons induces the emission of new electrons with a characteristic dynode multiplication factor, creating an exponential cascade. Therefore, high voltage is required for PMT operation, typically between 1,000-2,000V.

Due to the transport of electron charge carriers occurring in a vacuum, PMT signal collection is typically very fast, with rise times on the order of several nanoseconds. Typical values for photocathode quantum efficiency are 20-40 % and $10^5 - 10^8$ for gain [4].

2.2.2.2 Silicon photomultipliers

Silicon photomultipliers, or SiPMs, are a subclass of single-photon avalanche photodiodes (SPADs). They are functionally composed of P-N junctions with reverse-bias applied in excess of the chip's breakdown voltage, operating in Geiger mode. Photoelectric absorption in the SiPM produces electron-hole charge-carrier pairs which are accelerated in opposite directions, inducing avalanches and resulting in a measurable electrical current.

Due to the migration of electron-hole pair charge-carriers through a silicon crystal lattice, the timing performance of SiPMs is generally worse than that of than PMTs. SiPMs, however, possess characteristically high photon detection efficiency values of up to 0.5 and typical gain values on the order of $10^5 - 10^6$, linearly dependent on applied overvoltage. Bias voltage requirements are significantly lower for SiPMs than PMTs, on the order of a few tens of Volts [5].

2.3 Radiation Detection Theory of Plastic Scintillators

The following section describes the theoretical processes of detecting γ -ray and neutron radiation in PSD plastic scintillators on an atomic level; independent of individual scintillator properties and composition. The mechanisms of γ -ray and neutron detection and their differences are described, from which time-dependent differences in emitted scintillation light arise. The subsequent section, *PSD Method*, describes the implementation of PSD techniques for particle identification of detected radiation electrical signal pulses.

2.3.1 γ -Ray Detection

γ -ray detection by scintillators in the energy realm relevant to radioactive isotope decay occurs primarily through three processes: photoelectric absorption - in which a γ -ray is completely absorbed by an electron, Compton scattering - in which a photon scatters off an electron and deposits a fraction of its incident energy with respect to the scattering angle, and pair production - in which an energetic γ -ray in the vicinity of a nucleus produces an electron-positron pair. The probability of each of these interaction types is dependent on the incident γ -ray energy, as well as the atomic number of the target atom (Fig. 2.2).

As plastic scintillators are primarily composed of hydrogen ($Z = 1$) and carbon ($Z = 6$), the photoelectric effect, which scales with Z^{4-5} , rarely occurs and consequently a distinct photopeak in collected energy spectra is generally not observed. For incident γ -ray energies relevant to radioactive decay, between 100 keV - 10 MeV, the Compton scattering interaction process dominates. Observable spectral features thus include the Compton continuum and a Compton edge, with which energy calibration can be performed and energy resolution obtained.

The energy E' of a γ -ray following a Compton scattering interaction off an electron of mass m_e , as a function of scattering angle θ and incident γ -ray energy E , can be approximated using equation 2.2.

$$E' = \frac{E}{1 + \frac{E}{m_e c^2} (1 - \cos\theta)} \quad (2.2)$$

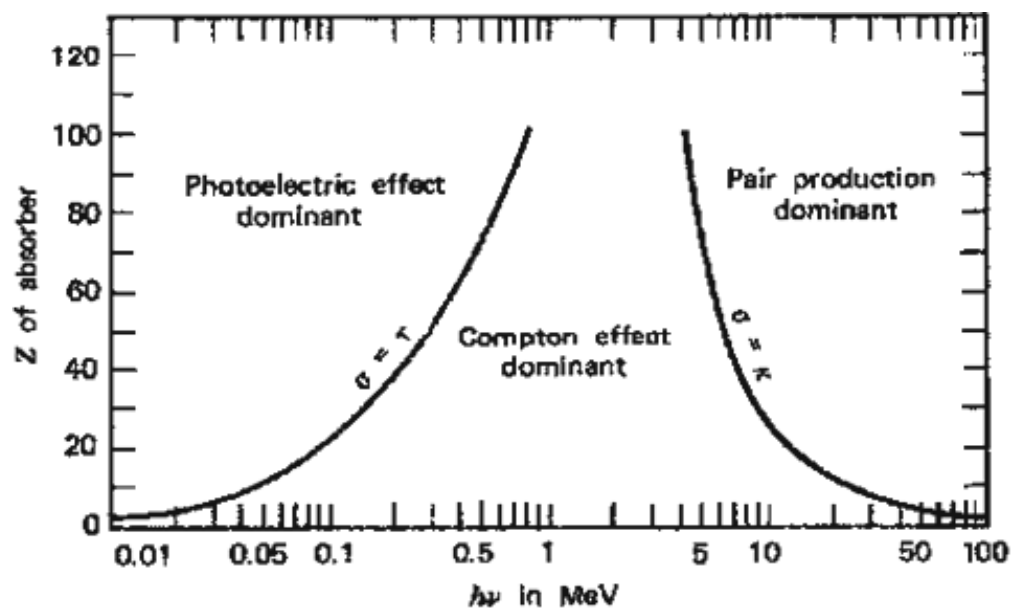


Figure 2.2: Logarithmic plot depicting the dominant γ -ray interaction mode as a function of atomic number (Z) and incident γ -ray energy in MeV [6]

In plastic scintillators, electrons that undergo Compton scattering interactions become ionized, electromagnetically energizing nearby electrons into excited states over the particle's range. The delocalized molecular π orbitals structure formed by the scintillator's aromatic rings facilitates migration and efficient exchange of energy between nearby electrons. Through this process, thousands of electrons are excited per MeV deposited by the original interaction; each emitting a photon upon de-excitation to their ground state. The energy of the emitted photons is dictated by the excited state to ground state transition energy.

2.3.2 Fast Neutron Detection

As mentioned in Section 2.2, organic plastic scintillators are capable of efficiently detecting fast neutrons through elastic and inelastic nuclear collisions. The energy deposited by a fast neutron interaction is dependent on the collision angle and the target nucleus' mass.

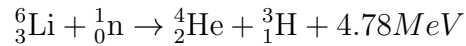
Due to the low- Z composition of approximately 50% hydrogen and 50% carbon by atomic fraction, organic and plastic scintillators are particularly sensitive to fast neutron interactions, with the possibility of full energy deposition events by incident neutrons colliding with hydrogen atoms. Energy deposited through fast neutron interactions ionizes the target nuclei, producing heavy charged particles (HCPs). HCPs transfer their kinetic energy to surrounding atoms through electromagnetic excitation of nearby electrons, followed by de-ionization when thermalized - an effect known as the Bragg curve.

The energy deposition pattern of HCPs is characterized as high linear energy transfer (LET). Due to the concentrated deposition of energy along a short travel path, produced scintillation light is disproportionately reduced; a phenomenon known as quenching. For neutron interactions in plastic scintillators, this quenching factor is on the order of 0.2-0.25 [7]. Therefore, calibrated neutron energy spectra are denoted in units of keVee (keV electron equivalent).

2.3.3 Thermal Neutron Detection

Due to the low thermal neutron interaction cross-sections of natural hydrogen and carbon, PSD plastics are not inherently sensitive to thermal neutron interactions. However, compositions can be doped with isotopes possessing higher thermal neutron absorption cross sections to provide this additional particle detection sensitivity. Notable dopant isotopes include ${}^6\text{Li}$, ${}^{10}\text{B}$, ${}^{155}\text{Gd}$ and ${}^{157}\text{Gd}$.

In this work, ${}^6\text{Li}$ doping is used to enable trimodal (γ -ray, fast neutron, and thermal neutron) particle detection sensitivity. Thermal neutron detection is facilitated by the ${}^6\text{Li}$ neutron capture reaction, producing α and triton HCPs with a combined kinetic energy of 4.78 MeV:



The respective particle energies can be calculated, in accordance with conservation of energy and momentum, using equation 2.3; yielding kinetic energies of 2.73MeV for the triton and $(4.78 \text{ MeV} - 2.73\text{MeV}) = 2.05 \text{ MeV}$ for the α particle.

$$E_T = \frac{m_{\alpha}}{m_T + m_{\alpha}} \times Q \approx \frac{4}{3 + 4} \times 4.78\text{MeV} \quad (2.3)$$

The HCPs created locally as a result of this neutron capture reaction possess greater momenta than those of recoil protons produced by fast neutron collisions, and thus have even greater characteristic LETs. As a result of quenching effects, the observed scintillation response is approximately 400-500 keVee [8], [9].

2.3.4 PSD

Pulse shape discrimination (PSD) is a signal-processing technique that works on the understanding that interacting particles with different LETs excite electrons into states with different characteristic decay times at different proportions. Low LET particle interactions, such as those of electrons ionized by γ -rays, primarily excite electrons primarily into singlet (S) states. Higher LET particle interactions, such as those of HCPs, excite electrons into singlet states as well as higher-energy triplet (T) states.

De-excitation of singlet states is rapid, on the order of tens of nanoseconds, and is referred to as fluorescence. The direct decay of a triplet state to ground, however, is a spin-forbidden

transition with a significantly longer decay time of 1-2 μ s, and is referred to as phosphorescence. Triplet state decay to ground can alternatively occur by means of triplet-triplet annihilation, in which two triplet states are converted to one ground state and one singlet state, which then decays to ground to fluorescence (Fig. 2.3). This process is termed delayed fluorescence [10].

The dense, localized energy deposition pattern of high LET particle interactions produces a high concentration of triplet states in close proximity, which combined with the delocalized electron orbital structure of PSD plastic scintillators, promotes efficient triplet state migration and annihilation. These time differences in emitted scintillation photons result in different pulse signal shapes (photomultiplier time-dependent charge collection patterns) for low and high LET radiation interactions of equivalent energy deposition (Fig. 2.4).

In practice, the inability of conventional plastic scintillators to perform PSD was attributed by Zaitseva et al. to the lack of efficient triplet-triplet annihilation, caused by excitation traps [11]. By significantly increasing the concentration of scintillating dye to 30 wt.%, this deficiency was overcome, enabling pulse shape discrimination comparable to contemporary organic crystal and liquid organic scintillator detectors [1].

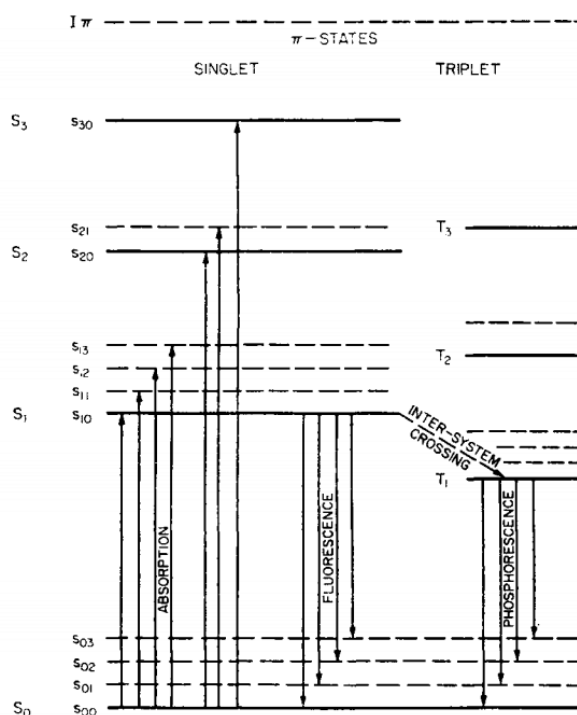


Figure 2.3: Electron energy levels diagram for an organic molecule with π -electron orbitals, depicting excited singlet ($S_1, S_2, S_3\dots$) and triplet ($T_1, T_2, T_3\dots$) states, as well as vibrational sub-levels ($S_{11}, S_{12}\dots$) [10]

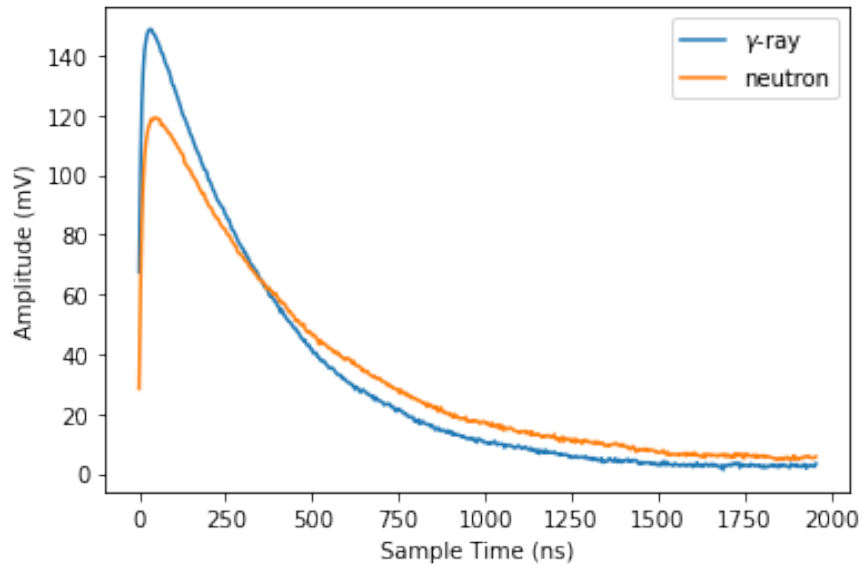


Figure 2.4: Plot comparison of sample 1 MeVee γ -ray and neutron SiPM signal pulse shape differences collected for PuBe-emitted radiation detected by a SiPM-coupled PSD plastic scintillator (Table 3.3 composition V)

2.4 PSD Method

Numerous PSD methods exist, utilizing different means to differentiate particle interactions based on their recorded time-dependent pulse shapes. In addition to analog methods, digital methods employ high-speed digitizers to store and process individual waveforms using computational methods. The following section describes the implementation of PSD on a high level, including discussion of waveform digitization and energy calibration for plastic scintillation detectors. Two separate digital PSD techniques utilized in this work: the tail fraction integration technique, used in laboratory measurements, as well as the time-invariant pulse shaping technique, used in mobile sUAS measurement applications.

2.4.1 Tail Fraction Integration

The tail fraction integration method, alternatively known as the tail-to-total ratio method, is a digital PSD technique which classifies digitized pulse waveforms according to incident particle type by evaluating the prominence of the waveform region following its peak amplitude (the “tail fraction”) as a metric of the proportion of detected delayed fluorescence scintillation light. The tail fraction integration method relies on high-speed digitization with common sampling rates of 100MHz and above.

PMT or SiPM analog output signals of detected scintillation events are converted to digital waveforms comprised of chronological arrays of voltages at fixed time intervals. The length of time between data points is set by the digitizer's sampling frequency. Voltage values are represented in integer analog-to-digital converter (ADC) units according to the employed digitizer's dynamic range its respective number of channels. Fig. 2.5, left, demonstrates a sample waveform of a 1" cylinder PSD plastic scintillator coupled to a SiPM array. The same pulse can be represented by more meaningful axes of voltage and sample time, by multiplying ADC units by the employed digitizer's (a Struck Systeme SIS3316 module) dynamic range (1.9V) and dividing by its number of channels (2^{14}), and dividing sample number by the sampling frequency (250MHz) (Fig. 2.5, right).

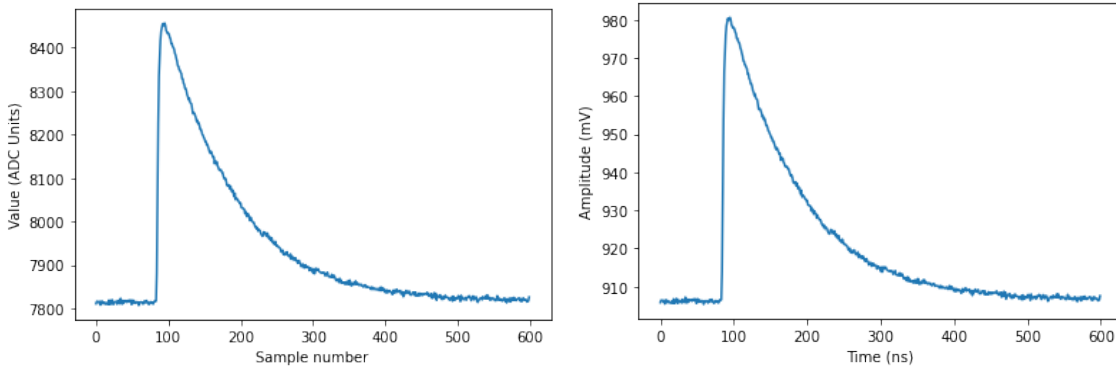


Figure 2.5: Plot of raw digitized SiPM pulse waveform of a ^{137}Cs -emitted γ -ray interaction in a SiPM-coupled PSD plastic scintillator (Table 3.3 composition V) in ADC units as a function of sample number (left), and voltage as a function of sample relative time (right)

For all recorded waveforms of a measurement, baseline is subtracted, signals trimmed, and aligned by starting or peak pulse index. An energy calibration is applied for evaluating waveforms within a desired energy region. Three parameters are then iteratively optimized: signal pulse starting index, signal pulse window length, and signal pulse tail starting index. For each iteration of the three parameters, a tail pulse fraction is calculated as the tail pulse integral, from the signal pulse tail starting index to the end of the signal pulse window, divided by the total pulse integral, from the signal pulse starting index to the end of the signal pulse window.

The calculated tail pulse fractions are plotted as a histogram, with a bimodal distribution indicative of PSD capability. Gaussian fits are applied to each region, and a figure of merit (FOM) calculated to quantify PSD. Values for the three parameters are iterated until those yielding the highest FOM are identified.

The figure of merit of a bimodal Gaussian distribution, such as of a tail pulse fraction histogram, is calculated according to Equation 2.4 as the absolute difference between the centroids (μ) of the two modes divided by the sum of their full-width at half-maximum

(FWHM) values (Fig. 2.6). For Gaussian distributions, FWHM can be mathematically related to the standard deviation σ . A FOM value greater than 1.27 represents 99% regional (γ -neutron particle) discrimination ability.

$$FOM = \frac{|\mu_n - \mu_\gamma|}{FWHM_n + FWHM_\gamma} = \frac{|\mu_n - \mu_\gamma|}{2\sqrt{2\ln 2}(\sigma_n + \sigma_\gamma)} \quad (2.4)$$

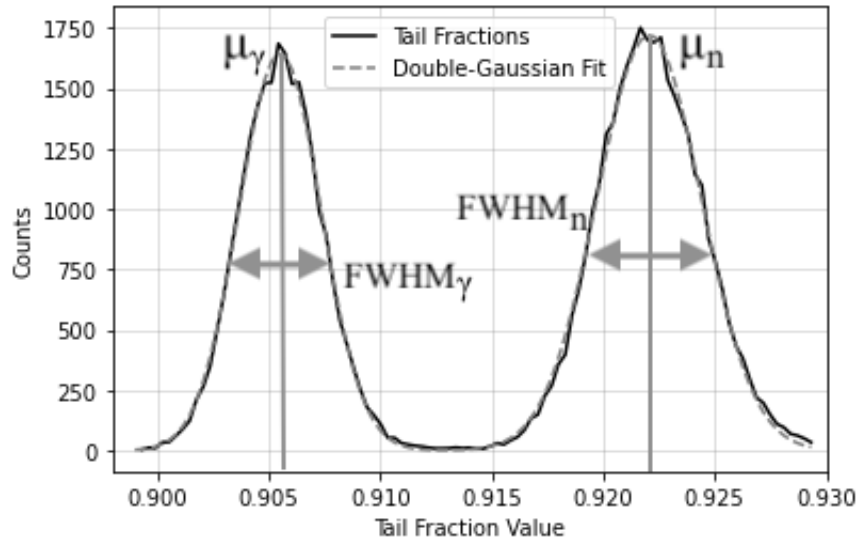


Figure 2.6: Histogram and corresponding double Gaussian fit of calculated tail pulse fraction values for detected signal pulses of PuBe-emitted γ -ray and fast neutron interactions of 475 ± 75 keV energy deposition in a SiPM-coupled PSD plastic scintillator (Table 3.3 composition V)

PSD FOM exhibits an energy dependence, as discernible differences in pulse shape for interactions of different particle types are limited by the signal-to-noise ratio (SNR). The effect of random noise fluctuations is more pronounced for lower-amplitude signal pulses of lower-energy detected interactions, widening FWHMs and reducing separation between the centroids. This effect is demonstrated in Fig. 2.7, displaying the variation in calculated FOM for three different waveform energy ranges obtained during a single measurement.

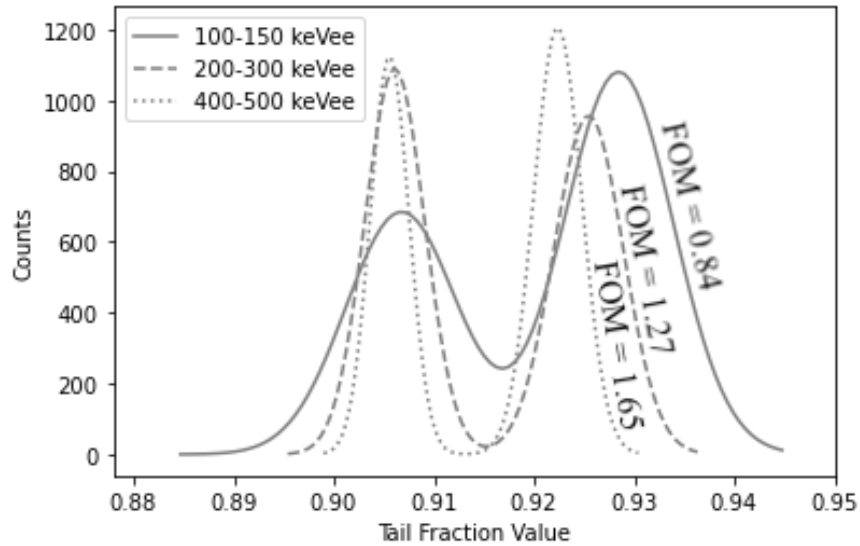


Figure 2.7: Histograms of tail pulse fraction values and associated FOMs for three separate interaction energy ranges of signal waveforms collected during a single measurement of PuBe-emitted radiation by a SiPM-coupled PSD plastic scintillator (Table 3.3 composition V)

In the case of a trimodal PSD plastic scintillator, a characteristic thermal neutron absorption “hump” may be present on the right-hand slope of the neutron region of generated tail pulse fraction histograms. This effect is demonstrated in Fig. 2.8 for calibrated waveform energies within 480 ± 50 keVee, of a γ -neutron source measured by a ^6Li -doped PSD plastic scintillator. If significant enough, this observed histogram feature may erroneously skew the calculated FOM to a lower value due to the widening of the neutron-pulse region’s FWHM. To account for this, either a triple-Gaussian fit can be utilized, or the left-hand half of the neutron region can be mirrored and a double-Gaussian fit applied to the modified histogram.

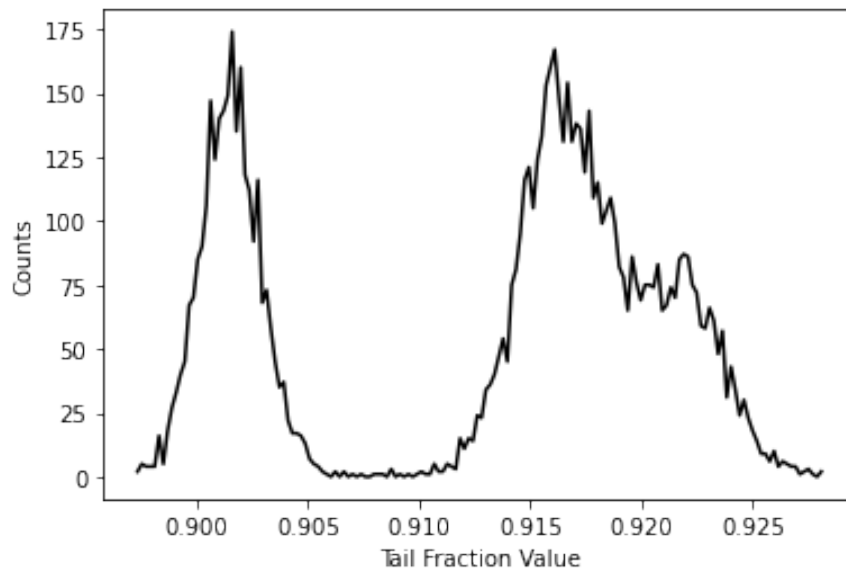


Figure 2.8: Histogram of tail pulse fraction values, demonstrating pronounced thermal neutron capture “hump”, for signal waveforms of recorded interaction energies within 450 ± 50 keV of PuBe-emitted radiation by an SiPM-coupled ${}^6\text{Li}$ -doped PSD plastic scintillator (Table 3.2 composition B)

The energy relationship of PSD FOM can be visualized by 2-dimensional contour plots, illustrating the distribution of tail pulse fractions as a function of their calibrated interaction energy. Using these figures, particle classification curves can be drawn to separate interactions by particle type according to their tail pulse fraction value and interaction energy, as demonstrated in Fig. 2.9.

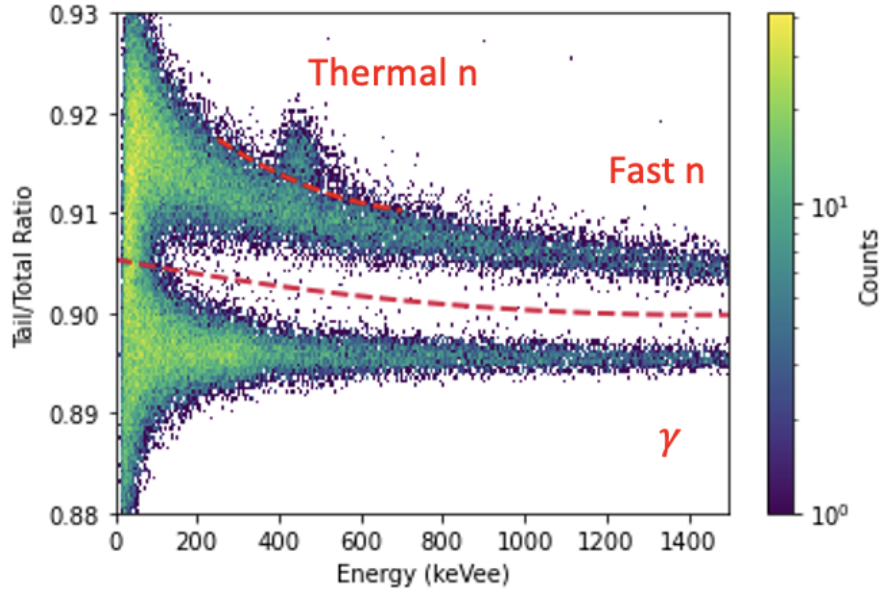


Figure 2.9: 2-dimensional contour plot of tail pulse fraction values as a function of energy for signal waveforms collected during a measurement of PuBe-emitted radiation by a SiPM-coupled ${}^6\text{Li}$ -doped PSD plastic scintillator (Table 3.3 composition B)

2.4.2 Energy Calibration

Energy calibration of plastic scintillators is performed using the known energy of the Compton edge of collected energy spectra of γ -ray sources. The Compton edge energy, or the maximum energy E_{max} deposited by an incident γ -ray of Energy E through Compton scattering, occurs for a scattering angle of 180-degrees θ . Equation 2.2 can be simplified for this case to

$$E_{max} = E - E' = E - \frac{E}{1 + \frac{E}{m_e c^2}(1 - \cos\pi)} = E - \frac{E}{1 + 2\frac{E}{511\text{keV}}} \quad (2.5)$$

Experimental energy spectra of γ -ray calibration sources yield broadened Compton edge regions, rather than a definitive Compton edge feature. Due to the relatively low light output resulting in poor energy resolution of plastic scintillators, the true Compton edge spectrum channel is often approximated as a percentage of the experimental peak channel height, typically 50-80%.

For a more accurate method of determining the location of the actual Compton edge, an empirical relation can be utilized to associate the measured energy resolution of the Compton edge with its true location, as a fraction of the peak height [12].

The resolution of the Compton edge is calculated as the peak channel (centroid) divided by the half-width at half-maximum (HWHM) value. In practice, this can be performed by

fitting a Gaussian curve to the Compton edge slope, and calculating resolution using the fitted centroid μ and standard deviation σ according to Equation 2.6.

$$Resolution = \frac{\mu}{HWHM} = \frac{\mu}{\sqrt{2\ln 2}\sigma} \approx 0.8493 \frac{\mu}{\sigma} \quad (2.6)$$

For each calibration source energy, a Compton edge channel is determined. A polynomial fit is then applied to the obtained calibration channel-energy pairs. The calibrated detector can then be used to evaluate PSD for specific energy regions.

The experimental implementation of the calibration procedure is described in detail in Section 3.3.

2.4.3 Time-Invariant Pulse Shaping

A second method of performing PSD is using Time-Invariant Pulse-Shape Signatures (TIPS). A proprietary implementation of this technique for real-time PSD is employed by the spectrometer of the sUAS in this work. In this method, TIPS are calculated for analog pulses and used to differentiate signals by particle type.

For an incoming PMT or SiPM signal pulse, TIPS is calculated by applying two trapezoidal filters: a fast shaper yielding an inverse sawtooth pulse and a slow shaper yielding a trapezoidal pulse, with the ratio of the heights of the slow to the fast shaped pulses defined as the TIPS [13]. When set correctly, the fast shaper output is proportional to the fast scintillation (fluorescence) component of the detected scintillation pulse, while the slow shaper is proportional to the total light detected. In a similar procedure as described for the tail fraction integration method, TIPS for the measured pulses are plotted as a histogram to yield a bimodal distribution in the case of PSD. Distribution fits are applied, from which FOM is calculated.

2.5 Structural Plastic Scintillators

Published research investigating the mechanical properties of plastic scintillation detectors supports their potential use as structural components.

Zaitseva et al. of Lawrence Livermore National Laboratory have identified compositional elements which affect mechanical strength and resistance to deformation, indicating the utility of cross-linking agents in enhancing mechanical stability of PSD plastic compositions containing increased concentrations of scintillating dye. Additional works identify compositional modifications, including cross-linkers and oxygen-containing compounds, resulting in enhancements of physical properties such as resistance to aging, radiation damage, moisture effects, and temperature variations [14], [15]. Favorable effects of cross-linking on mechanical and temperature stability have been additionally supported by [2].

Research from the University of Tennessee, Knoxville investigates the tensile, flexural, and light output properties of several commercial plastic scintillators, comparing differences in

polymer bases (polyvinyl toluene and polystyrene), cross-linking, and organometallic complexes [16]. The study's findings show that plastic scintillator compositions can achieve tensile and flexural strengths similar to those of commercial structural plastics, and can be enhanced mechanically by the use of cross-linking compounds with minimal degradation to light output values.

The effects of neutron, γ -ray, and proton-beam radiation on structural and optical properties of plastic scintillators have been characterized by [17], [18], and [19], among others.

2.6 Aerial Radiation Detection

Aerial radiation detection utilizes radiation detectors deployed on aerial platforms to localize sources of detected radiation signatures in an environment. Radiation detection from an aerial platform possesses distinct advantages to other deployment means, including increased mobility in 3D, the ability to measure sources from a wide range of angles, maneuverability in areas restricting ground vehicles, and in the case of unmanned aerial systems (UASs), reduced operator dose.

Technological developments in modern sUASs have enabled the deployment of complex radiation detection payloads on compact, commercial multirotor vehicles. This approach allows for the minimization of source-detector distances, paramount for efficient measurement of radiation data. The intensity of radiation, interpretable as available detectable information, is inversely proportional to the square of the distance between the source and the point of measurement, according to the inverse square law of radiation intensity. As a result, mass-constrained systems such as radiation-detecting sUASs balance source-detector distance with detector and associated deployment platform size in order to achieve optimal system capabilities.

2.6.1 Source Localization Methods

Different methods are available for localizing sources with respect to detected radiation in space, commonly categorized as either proximity mapping or imaging.

2.6.1.1 Proximity Mapping

Proximity mapping is performed by varying the detector location around a measurement space and utilizing location-dependent differences in measured count rates to identify the most probable locations of emitting sources. Depending on detector capabilities, such as spatial resolution, analysis of measured count rates can be done either manually, such as by visual inspection of plotted detected counts overlaid on a map of the measurement space, or algorithmically using reconstruction techniques such as maximum likelihood expectation maximization (MLEM) and Gaussian Process Prior (GPP).

2.6.1.2 Imaging

The second category of source localization methods is radiation imaging. Conceptually, radiation imaging is performed by applying knowledge of the underlying physics processes of radiation interactions in a detector to correlate the incident direction of radiation. By aggregating the incident directions of a large number of detected events, source location(s) can be determined. Various techniques for imaging γ -rays and neutrons are available, such as coded aperture, Compton imaging, and time-of-flight.

2.7 Scientific Hypothesis

The aim of this work is to demonstrate the feasibility of leveraging together the optical and mechanical properties of PSD plastic scintillators to employ detectors in structural roles while maintaining PSD capability. In doing so, the potential for fabricating systems composed of majority active scintillator by mass (active mass utilization > 0.5) is tested. The benefit of this technology is most prominent in volume-constrained and mass-constrained systems. In volume-constrained systems such as compact mobile devices (e.g. handheld, backpack), multi-functional utilization of components allows for increased total detector volume. In mass-constrained systems such as aerial vehicles, the use of structural detectors allows for increased active mass utilization and potential reduction of source-detector distances.

Specifically, this work seeks to evaluate the feasibility of fabricating a radiation-detecting sUAS composed structurally of PSD plastic scintillators with a target active mass utilization of 0.5 (50% active detector by mass). The construction of a payload-less radiation-detecting sUAS will additionally evaluate the feasibility of overcoming current limitations of conventional payload-carrier configurations in achieving sub-1 meter source-detector distances.

Chapter 3

Evaluation of PSD Plastic Compositions

The first step to integrating PSD plastic scintillators as structural components is the identification of a suitable scintillator material. To successfully serve as an active-volume structural component, the PSD plastic scintillator must possess optical properties enabling PSD capability in its final structurally-serving geometry, while simultaneously exhibiting adequate intrinsic mechanical properties to fulfill its load-bearing demands. Both composition and preparation conditions affect the resulting optical and mechanical properties of a PSD plastic scintillator, and can be altered with the objective to achieve desired properties. In this chapter, PSD plastic scintillators of varying compositions and curing conditions were evaluated to assess whether scintillators with favorable material properties can be developed meeting target performance requirements for PSD figure of merit, tensile strength, and elastic modulus.

3.1 Target Requirements

The following section establishes a characterization baseline for evaluating a PSD plastic scintillator's viability for use as an active-volume structural component in consideration of its optical (PSD) and mechanical (strength) performance. While the criteria for adequate PSD capability and mechanical strength are dependent on the application and individual system constructed, the requirements established below are initially derived as a conservative set of minimum requirements applicable for a broad range of structural applications, and later refined by an experimentally-validated computational study of mechanical forces experienced by a sUAS.

3.1.1 PSD Capability

A composition's PSD capability is evaluated by characterizing its PSD FOM. For the purposes of establishing a PSD evaluation metric to determine a composition's viability for use as a structural detector, the minimum FOM threshold is set at 1.27 for detected γ -ray and neutron radiation interactions with energy deposition between 405-555 keVee. The specified energy region is selected in order to assess the capability of ^6Li -containing compositions to distinguish both fast and thermal neutron detected interactions from γ -ray detected interactions within the characteristic energy region for thermal neutron absorption.

3.1.2 Mechanical Requirements

The mechanical properties requirements for structural implementation of PSD plastic scintillators are dependent a variety of factors, such as the intended system application, component requirements within an assembly, as well as component operating environment. For the case of constructing a sUAS using structural PSD plastics, general mechanical requirements can be inferred from examining the materials used in conventional sUAS frame construction. More specific requirements can be obtained by conducting computer model simulations to quantify predicted stresses withstood by structural elements in representative operating environments.

3.1.2.1 Conventional sUAS Frame Materials

Conventional sUAS frames are composed primarily of materials possessing high strength-to-weight ratios, with commonly employed materials in aerospace applications found in commercially-available sUASs. Frame materials are selected for structural strength with minimal required mass, in order to maximize the thrust:weight ratio of constructed systems, as well as for rigidity to minimize frame flex and vibration during flight. Example materials include lightweight aluminum alloys, high-strength plastic composites, fiberglass-reinforced plastics, and increasingly in recent years carbon fiber and carbon fiber composites. Values for yield strength and Young's modulus (stiffness) of selected sample materials are listed in Table 3.1.

Table 3.1: Table listing reference tensile strength, elastic modulus, and density ranges of common materials used in sUAS construction including aerospace-grade aluminum, extruded acrylonitrile butadiene styrene, nylon 66 30% glass fiber filled, nylon 66 30% carbon fiber filled, and FR-4 G-10 fire-retardant glass-epoxy laminate used in printed circuit boards [20][21][22][23][24]. Values for tensile (Young’s) elastic modulus are provided for all materials except G-10, FR-4, for which flexural modulus of elasticity is listed.

Material	Tensile Strength (MPa)	Elastic Modulus (GPa)	Density (g/cm ³)
Aluminum 2024-T3	345	72	2.768
ABS, Extruded	13 - 65	1.00-2.65	1.01-1.2
Nylon 66, 30% GF	18.8-290	0.08-16.2	1.14-1.82
Nylon 66, 30% CF	137-350	14-33.1	1.20-1.57
G-10, FR-4	262-310	16.5-18.6	2.7

For the application of an active-volume sUAS frame, employed structural scintillators must withstand the same dynamic stress conditions experienced by conventional sUAS frames. While an active-volume sUAS frame seeks to maximize frame mass relative to the total sUAS mass, rather than minimize it, the intrinsic mechanical properties of the component scintillators must still meet the mechanical requirements for flight. These intrinsic mechanical properties are evaluated as the material yield strength and elastic (Young’s) modulus.

While often overlooked in favor of strength and stiffness in conventional sUAS frame material selection, the fracture behavior of structural PSD plastic scintillators should be considered. Conventional sUAS frame materials typically exhibit brittle fracture behavior, creating the potential for catastrophic failure modes in the event of frame damage. Materials exhibiting plastic deformation prior to fracture (i.e. bending before breaking) provide an additional measure of safety for a constructed aerial system.

Additional mechanical properties of interest not investigated in this work include resistance to crazing, stability at temperature extremes, and resistance to cyclic fatigue.

3.1.3 Proof-of-Concept sUAS Structural Component Replacement

To narrow the range of mechanical properties required of PSD plastic scintillator materials in the specific application of structural sUAS components, a preliminary proof-of-concept replacement of a structurally-demanding component of an existing sUAS was conducted. The components chosen for replacement by PSD plastic scintillators were the landing gear of Lawrence Berkeley National Laboratory’s (LBNL) radiation mapping sUAS, consisting of the NG-LAMP detection system aboard a DJI Matrice 600 carrier vehicle (Fig. 3.1) [25], [26]. Computer-aided design models were constructed of a representative sUAS mass with the landing gear replaced by plastic scintillators, and dynamically simulated to analyze the

stresses and deformation predicted for a variety of flight scenarios to obtain required minimum strength estimates. These estimates were used as the evaluation metric for identifying scintillators with suitable mechanical properties. The results of the computational modeling were verified experimentally by the replacement of the landing gear of a LBNL-operated DJI Matrice 600 sUAS. SiPM biasing and readout boards were designed and manufactured, accompanied by 3D-printed protective housings and mounting hardware, for integration with the NG-LAMP detection system. The constructed system was subjected to field-testing involving a series of flights and takeoff-landing impact cycles.

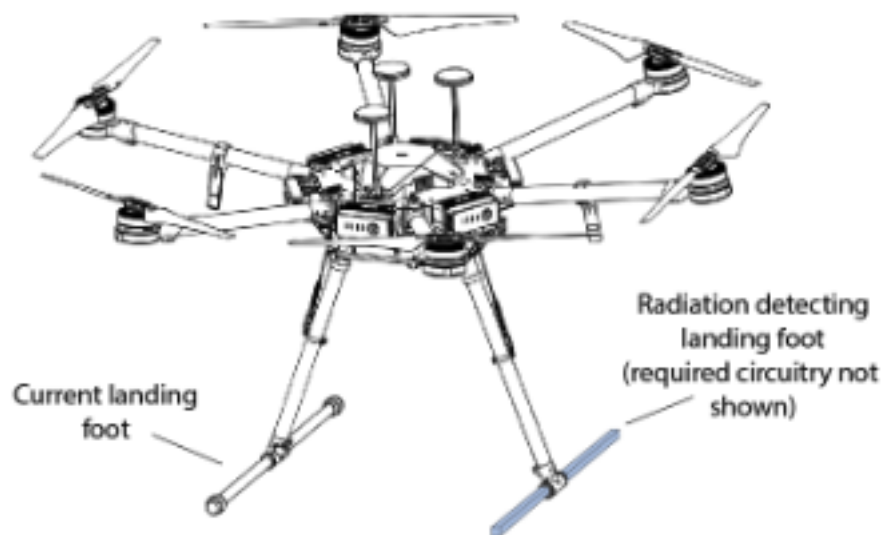


Figure 3.1: Schematic of DJI Matrice 600 flying platform with landing gear replaced by a structural scintillator rod in blue (associated detection equipment not depicted) [26]

3.1.4 Dynamic Stress Simulation

To predict the real-world stresses experienced by the system prior to construction, the planned configuration was modeled in SolidWorks as a 16-inch long, 1-inch wide square prism of polystyrene material supporting a vertically-angled carbon fiber leg at its center lengthwise, with the remaining sUAS mass approximated as a 12.7kg (9.1kg for the sUAS platform, 3.6kg for NG-LAMP) axial load applied to the vertical leg. Dynamic simulations of the modeled system were conducted to estimate the maximum stresses experienced by the landing gear in takeoff, level flight, and free-fall landing scenarios. Two free-fall landing scenarios were simulated: level landing with the sUAS weight evenly distributed across a pair of identical landing feet, and uneven landing with initial ground contact made by a

corner of one landing foot (Fig. 3.2). Landing impact resulting from a 1-meter free-fall was simulated as an upward force to the initial point(s) of contact.

The results of the simulation study indicate the configurations with highest endured mechanical stresses were the free-fall landing scenarios, as expected, with predicted magnitudes of 19.2 MPa for an even landing and 135 MPa in a worst-case uneven landing scenario. For the purposes of establishing relevant mechanical properties requirements for scintillator compositions used in the construction of payload-less sUASs, the scenario involving a payload-carrying sUAS free-fall and suboptimal (crash) landing was considered outside of application scope. Applying a factor of safety of 1.5, standard for components sustaining external loads in aerospace applications, the minimum required material strength threshold of 28.8 MPa was thus derived, rounded to 30 MPa.

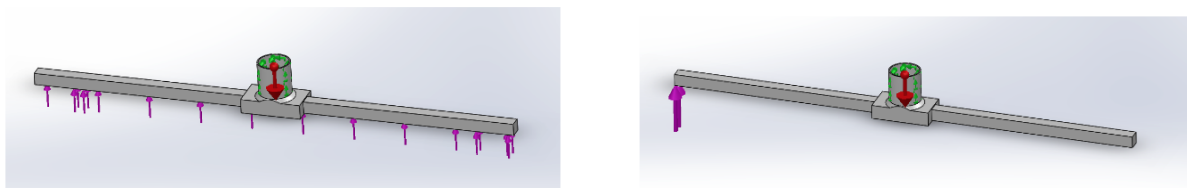


Figure 3.2: SolidWorks dynamic simulation depicting locations of sustained mechanical stress by structural PSD plastic scintillator landing gear induced in scenarios of level landing (left) and uneven landing with initial ground contact on landing foot corner (right) [27]

3.2 Materials

To evaluate the effect of composition and scintillator preparation conditions on measured optical (PSD) and mechanical properties, a comprehensive study of PSD plastic scintillator compositions was conducted in collaboration with the Natalia Zaitseva group of LLNL. 22 PSD plastic scintillator compositions were provided in 3 iterations with varying solvent matrix type and proportions, primary (scintillating) dye type, secondary (wavelength-shifting) dye type, and ^6Li -salt doping matrix type and concentration. The evaluated compositions are listed in Tables 3.2 and 3.3. A selection of the evaluated compositions is photographed in Fig. 3.3.

Solvent matrix effects were examined through evaluating compositions with varying proportions of polystyrene (PS), Poly(methyl methacrylate) (PMMA), and Poly(methacrylic acid) (PMAA). In addition to solvent matrix, two scintillating dyes were compared: 2,5-diphenyloxazole (PPO) and m-terphenyl (m-TP), at concentrations of 30% and 10% by weight. ^6Li was added to some compositions, as indicated, using a matrix-soluble salt, with ^6Li -isovalerate and ^6Li -IBA used for PS:PMAA-based compositions, and ^6Li -3-MeSA and ^6Li -BSA used for PS:PMMA-based compositions.

Among the compositions, wavelength-shifting dye varied as either 1 wt% E404 (Exalite 404, 1,4-bis(9,9-diethyl-7-(tert-pentyl)-9H-fluoren-2-yl)benzene) or 0.2 wt% bis-MSB (1,4-bis(2-methylstyryl) benzene) [28]. All compositions contained 5 wt% divinylbenzene (DVB), serving as a cross-linking agent.

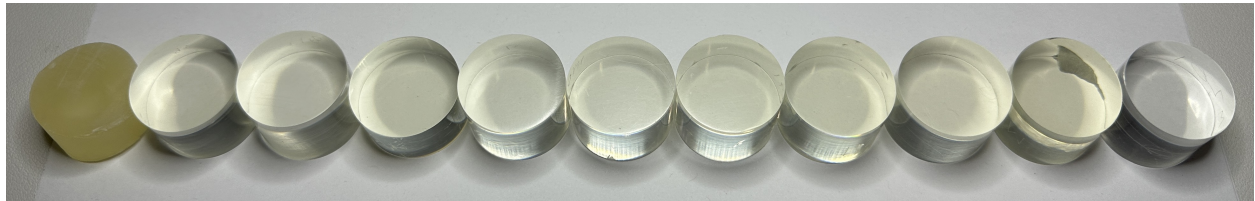


Figure 3.3: Photo of selected evaluated compositions, in order from left to right: J*, I, D, F, V, K*, L*, M*, N*, O*, C**

In addition to effects of composition, the effects of preparation method on the resulting PSD and mechanical properties was additionally studied. Six samples of identical composition, with labels denoted by an asterisk (*), were prepared and cured in an oven for varying durations and temperatures. All six samples were prepared and polymerized in an oven at 60°C. After 15 hours and 20 minutes total elapsed time, sample J* was removed. After 63 hours and 20 minutes total elapsed time, sample K* was removed. The oven temperature was then raised to 75°C over a period of 3 hours. After 69 hours and 50 minutes total elapsed time, sample L* was removed. After 135 hours and 5 minutes total elapsed time, sample M* was removed. After 182 hours and 5 minutes total elapsed time, sample N* was removed. The oven temperature was then raised to 85°C over a period of 30 minutes. After 231 hours and 5 minutes total elapsed time, sample O* was removed.

Although nitrogen was maintained for the curing environment, it was noted that the samples were exposed to oxygen each time the oven door was opened to remove a sample, disturbing the inert environment. Therefore it may be possible that temporary exposures to oxygen may have influenced the measured samples' properties.

In addition, sample J* (pictured on the far left in Fig. 3.3) was not measured for PSD FOM, as the presumed insufficient curing resulted in an optically opaque sample without a flat face conducive to SiPM readout coupling.

Table 3.2: Table of evaluated PSD plastic compositions containing PS:PMAA solvent matrix in various proportions as well as their respective primary dye, λ -shifting dye, and ^6Li doping matrix type and content

Label	PS:PMAA	Primary Dye	λ -shifting Dye	^6Li (wt%)	^6Li (at%)
A	100:0	m-TP	E404		
B*	90:10	m-TP	E404	1.5% ^6Li -IBA	0.1
C**	100:0	PPO	E404		
D	100:0	PPO	E404		
E	69:31	PPO	bis-MSB	1.8% ^6Li -Val	0.1
F	80:20	PPO	E404		
G	85:15	PPO	bis-MSB	1.8% ^6Li -Val	0.1
H	90:10	PPO	bis-MSB		
I	90:10	PPO	E404		
J*	90:10	PPO	E404	1.7% ^6Li -IsoVal	0.094
K*	90:10	PPO	E404	1.7% ^6Li -IsoVal	0.094
L*	90:10	PPO	E404	1.7% ^6Li -IsoVal	0.094
M*	90:10	PPO	E404	1.7% ^6Li -IsoVal	0.094
N*	90:10	PPO	E404	1.7% ^6Li -IsoVal	0.094
O*	90:10	PPO	E404	1.7% ^6Li -IsoVal	0.094
P	92:8	PPO	bis-MSB	1.8% ^6Li -Val	0.1

Table 3.3: Table of evaluated PSD plastic compositions containing PS:PMMA solvent matrix in various proportions, as well as their respective primary dye, λ -shifting dye, and ^6Li doping matrix type and content

Label	PS:PMMA	Primary Dye	γ -shifting Dye	^6Li (wt%)	^6Li (at%)
Q	50:50	PPO	bis-MSB		
R	50:50	PPO	bis-MSB	2.2% ^6Li -3-MeSA	0.08%
S	75:25	PPO	bis-MSB	2.6% ^6Li -3-MeSa	0.10%
T	85:15	PPO	bis-MSB	4.2% ^6Li -BSA	0.10%
U	90:10	PPO	bis-MSB		
V	90:10	PPO	E404		

3.3 PSD Characterization

The content of this section delineates the systematic procedure for PSD characterization of the compositions described in Section 3.2. The specific implementations of energy calibration and PSD FOM determination are described in detail, followed by a discussion of the obtained

PSD characterization results in regards to compositional differences and sample preparation conditions.

A controlled measurement environment was arranged to characterize the PSD properties of each composition sample in a consistent manner (Fig. 3.4). Readout was performed using a common Sensl J-Series 6mm 2x2 SiPM array. For each sample, the scintillator and SiPM surfaces were cleaned of dust and residue using ethanol, cotton swabs, lint-free wipes, and compressed air, and coupled using a pea-sized dollop Eljen EJ-550 optical coupling grease. The coupled scintillator-SiPM assemblies were wrapped in four layers of high-density PTFE tape to reflect scintillation light, followed by three layers of Eljen EJ-554 black vinyl tape to seal the detector from external light. A printed circuit board (PCB) was designed and manufactured for the SiPM array to provide reverse-bias voltage through the common cathode and sum the four signal anodes into a single output. Chapter 6 includes a detailed discussion of SiPM biasing and readout PCB design. A TENMA 72-6905 laboratory power supply was used to supply a bias voltage of +29.5V, connected using a 50 Ω MCX-BNC RG-174/U cable.

Digitization of SiPM signal readout waveforms was performed by a Struck Systeme SIS3316 250MHz digitizer powered by a VME rack and connected to the SiPM board's signal output via a 50 Ω MCX-BNC RG-174/U cable and a BNC-VME adapter. Digitized pulse waveforms were collected in 4ns sample increments for 600 sample length (2.4 μ s) pulse window intervals, with pre-trigger delay set to 100 samples. Dynamic range was set to 1.9V with 14-bit resolution. Trigger threshold was set to 120 (13.9mV). Wired data transmission to a local Linux machine via CAT 6 ethernet cabling was facilitated through a local area network (LAN) router.

Waveform packets transmitted from from the digitizer buffer were saved into HDF5 data files. The raw HDF5 data files were parsed into 2-dimensional NumPy arrays using the h5py Python package for analysis and postprocessing.

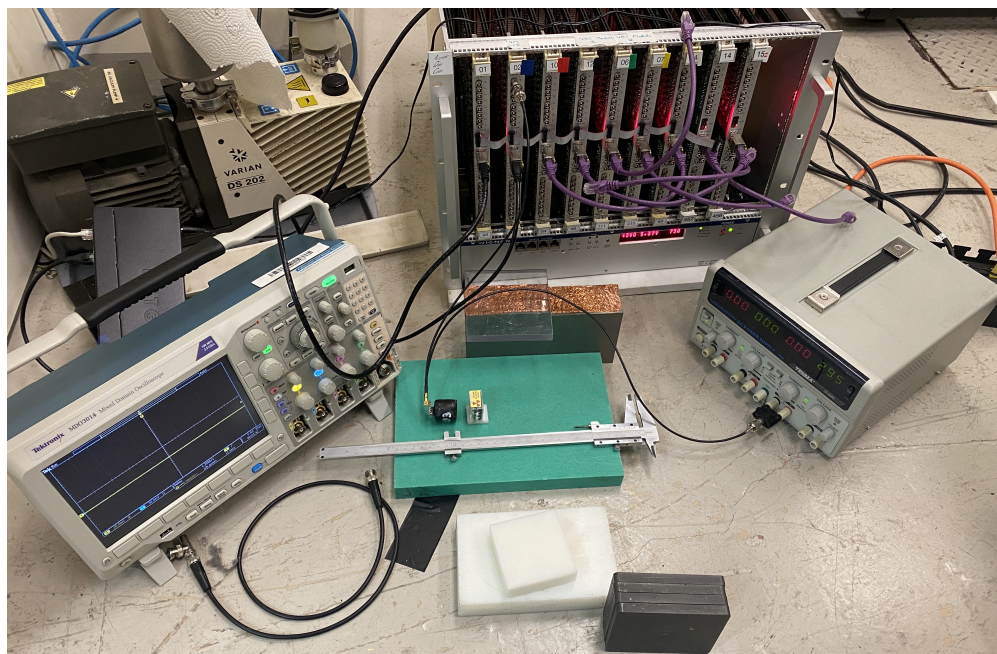


Figure 3.4: Photo of experimental setup for PSD evaluation of 1” cylindrical compositions

3.3.0.1 Calibration

Calibration waveform data were collected for 5-minute measurements of $1 \mu\text{Ci } ^{137}\text{Cs}$ and ^{22}Na point sources placed at a distance of 1 inch from the scintillator face opposing the SiPM readout face.

A Python pulse-processing script was written to perform data cleaning of the raw waveforms, generate an energy spectrum of calculated pulse integrals, and determine true Compton edge location using the calculated half-width-half-max energy resolution. Data cleaning was performed by first subtracting an averaged background of the first 50 samples acquired from the pre-trigger delay for each collected waveform. Signal pulses were then filtered by trigger time, and pulses with peak value times offset more than 25 samples from the set pre-trigger delay removed. Simple pile-up rejection was implemented following the criteria of excluding waveforms with values greater than 30% of the peak height in the final 200 time samples. Signal pulses were aligned by the first value greater than 20% of the pulse maximum.

To front-load computationally-heavy operations prior to parameter iteration loops, a cumulative trapezoidal integration (using the `scipy.integrate.cumtrapz` function) was applied to each cleaned pulse and stored in a 2-dimensional NumPy array. For given pulse start and end time parameter indices, the pulse integral was thus efficiently acquired by subtracting the pre-computed cumulative pulse integral at the specified pulse start index from the pre-

computed cumulative pulse integral at the specified pulse end index. A histogram of pulse integrals produced for a given measurement yielded the calibration spectrum.

To calculate the Compton edge of a generated calibration spectrum, the spectrum was first smoothed using a Savitzky–Golay filter (`scipy.signal.savgol_filter`) and then peak-fitting function `scipy.signal.find_peaks` applied to identify the highest-prominence peak, designating the Compton edge peak channel. The HWHM was calculated as the number of channels between the Compton edge peak channel and the first channel following the Compton edge peak channel with a value less than 50% of the peak channel counts (Fig. 3.5). HWHM energy resolution was then calculated as the peak channel divided by the HWHM.

From the obtained resolution, the true Compton edge location was identified as a percent of the Compton edge peak height channel as described in Chapter 2.5. The obtained true Compton edge location was identified as the first spectrum bin following the peak channel with a value less than the specified percentage of the peak channel height (Fig. 3.5).

The described calibration process was applied to perform three-point calibration using the ^{137}Cs γ decay Compton edge at 478 keVee, the ^{22}Na positron-annihilation Compton edge at 361 keVee, and the ^{22}Na γ decay Compton edge energy of 1061 keVee. A third-degree polynomial was fitted to the three channel-energy calibration points to obtain the calibration coefficients, for converting pulse integral in ADC units to energy deposited in keVee.

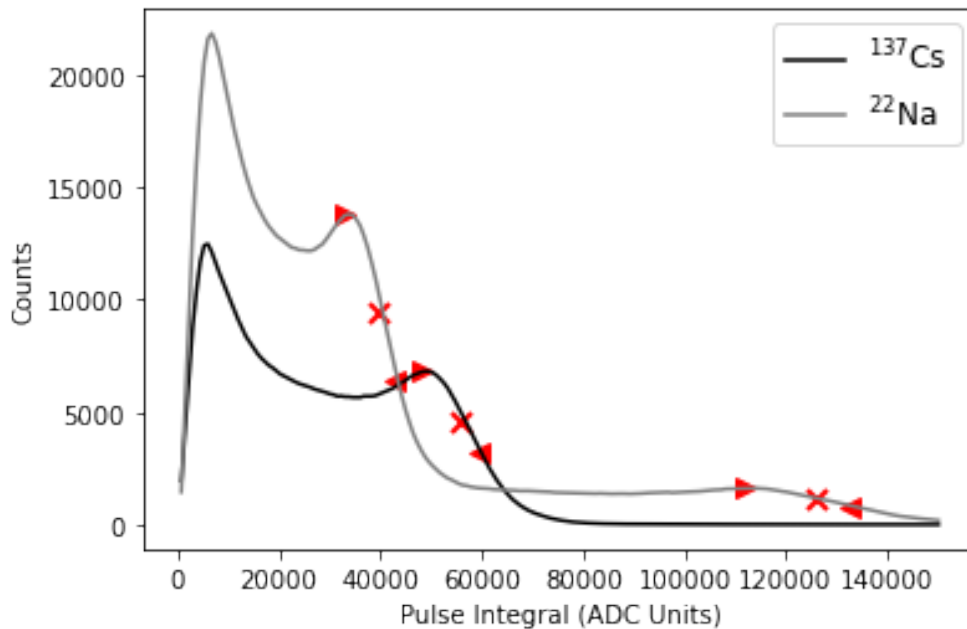


Figure 3.5: Energy calibration of SiPM-coupled PSD plastic scintillator (Table 3.3 composition V), with Compton edge peak channel marked by right-facing triangle, Compton edge half-maximum channel marked by left-facing triangle, and estimated true Compton edge channel marked by the letter 'X'.

3.3.0.2 Measurement

Following energy calibration, a 20-minute PSD measurement was performed of a 1 Ci PuBe source placed at a distance of 3" from the scintillator face opposite the SiPM readout face, with lead shielding of 2" thickness placed in between to equalize the proportion of detected γ -ray and neutron interactions.

Digitized pulse waveforms were collected in the same manner as the calibration measurements. Following pulse cleaning and processing, the pulse end, pulse start, and tail pulse region start indices were progressively iterated to determine the optimal parameters maximizing the γ -n discrimination figure of merit.

Within each iteration of pulse end index and pulse start index, the pre-computed cumulative integral value at the pulse start index (ϕ_i) was subtracted from the pre-computed cumulative integral value at the pulse end index (ϕ_f) for both the calibration and measurement datasets, yielding the total pulse integrated charge for each waveform. An energy calibration was performed for the iterated pulse start and pulse end parameters, and applied to the measurement dataset to filter measurement waveforms with calibrated pulse energies within the energy region surrounding the thermal neutron hump (405-555 keVee) for further PSD analysis. For these waveforms, the pulse tail start index was iterated and the tail-pulse to total-pulse fraction of the filtered measurement waveforms calculated for each iteration, according to equation 3.1.

$$\text{Tail to total Fraction} = \frac{\phi_t - \phi_i}{\phi_f - \phi_i} \quad (3.1)$$

The calculated tail pulse fraction values for the measurement waveforms were used to generate a histogram, yielding a bimodal distribution signifying detected γ -ray interactions at lower tail-total fraction values and neutron interactions at greater tail-total fraction values. FOM was quantified by fitting a Gaussian distribution to each region as described in Section 2.4.1. For ${}^6\text{Li}$ -doped compositions, a triple-Gaussian fit was applied for composition B only, as measurements by other ${}^6\text{Li}$ -containing compositions did not exhibit a prominent enough thermal neutron capture hump to be discernible by the fitting algorithm. For those compositions, the unaltered (left) half of the neutron region was mirrored and a Gaussian fit applied to the modified histogram, as described in Section 2.4.1.

The highest obtained FOM and the associated ϕ_i , ϕ_f , and ϕ_t indices were recorded as the optimal parameters, using which tail pulse fraction computation was extended for signal waveforms of all recorded energies and plotted as a function of interaction energy to produce composition-specific PSD plots.

3.3.1 PSD Characterization Results

The results of PSD FOM characterization for each composition are plotted in Figs. 3.6 and 3.7. Composition FOM values are plotted along a horizontal axis signifying solvent matrix polystyrene percentage. Different composition types are indicated by representative marker

shapes, with square markers representing PS:PMMA based compositions, circular markers representing PS:PMAA based compositions, and diamond markers representing compositions with PS only as the solvent base matrix. All compositions contain 30% PPO scintillating dye by weight excepting those denoted by triangular markers, which represent compositions containing 30% m-TP scintillating dye by weight and a PS:PMAA base. The exception is composition C**, which contains 10% PPO by weight. Filled composition markers denote ^6Li doping.

Measured PSD FOM among the compositions evaluated ranged between 0.891-2.377 with composition A, containing m-TP scintillating dye and no ^6Li , demonstrating the highest achieved FOM. Its generated PSD plot is displayed in Fig. 3.8, left. Significant PSD FOM degradation was generally observed for ^6Li -doped compositions as compared with their non- ^6Li -doped counterparts, for example in comparing compositions R and S. Of the ^6Li -doped compositions, composition B containing m-TP scintillating dye exhibited the highest PSD FOM value of 1.496, with its corresponding PSD plot displayed in Fig. 3.8, right.

PSD plots of characterized compositions with PSD FOMs above 1.27 for the 405-555 keVee energy region demonstrate clear visual separation and lack of overlap of the γ -ray interaction (lower) and neutron interaction (higher) prongs within the evaluated energy region. If ^6Li -doped, fast and thermal neutron detected interactions are easily distinguishable from γ -ray induced signal pulses (Fig. 3.9, left). Compositions with FOMs significantly higher than 1.27 present clear separation of the particle identification regions into energy regions well lower than 400 keVee, while compositions with FOMs below 1.27 may demonstrate sufficient separation at energy regions higher than 555 keVee (Fig. 3.9, right), or none at all.

Applying the established FOM threshold criteria, denoted by the horizontal dashed line in Figs. 3.6 and 3.7, reveals that no ^6Li -containing compositions of PS:PMMA base demonstrated sufficient PSD capability for further implementation as structural detector materials, with the exception of composition S. The compositions that met or exceeded the minimum FOM criteria include all compositions of PS:PMMA base not containing ^6Li , both compositions containing m-TP scintillating dye, composition S, and compositions K*, L*, and P, of PS:PMAA base.

^6Li -doped compositions of PS:PMAA base indicate a potential inverse dependence of FOM on PMAA fraction, evident when contrasting sample E, possessing the highest PMAA:PS ratio of 31:69 and the lowest FOM for the composition type of 0.898, with sample P, possessing the lowest PMAA:PS ratio of 8:92 and the highest FOM for the composition type of 1.408. A similar corresponding relationship was not significantly observed for PS:PMMA base compositions, which may potentially be better understood with more data.

Of the two compositions of PS-only base, the composition containing 30% PPO by weight (composition D) exceeded the FOM threshold with a FOM of 1.890, while the composition containing 10% PPO by weight (composition C**) did not meet the threshold with a FOM of 1.133, as expected due to its relatively low scintillating dye content.

The evaluated compositions do not serve as an exhaustive representation of possible scintillator composition types and proportions. Between batches of requested compositions fabricated by Zaitseva et al. at LLNL, preference was indicated to evaluating ^6Li -containing

compositions in order to identify PSD plastic scintillators potentially suitable as structural materials featuring trimodal particle sensitivity. Promising preliminary results from ^6Li -containing PS:PMAA-base compositions encouraged the investigation of a greater quantity of these samples. Likewise, compositions containing m-TP were requested for further evaluation following promising initial characterization results; however at the time of the study, a scarcity of high-purity m-TP reagent arising from global supply chain issues provoked by the COVID-19 pandemic led to the investigation focusing on the optimization of PPO-dyed compositions.

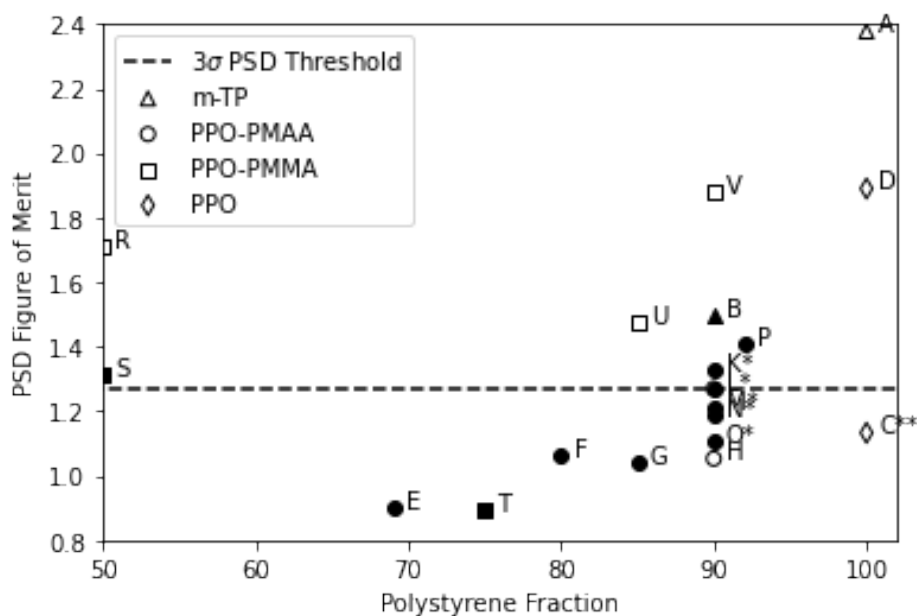


Figure 3.6: Plot of calculated PSD FOM values as a function of solvent matrix PS percentage for evaluated compositions. Filled markers indicate ^6Li doping.

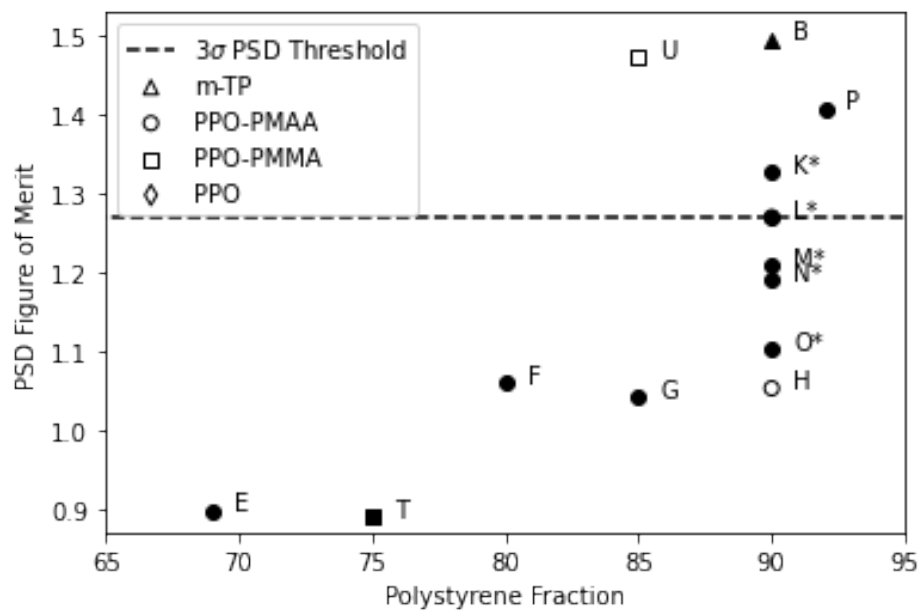


Figure 3.7: Fig. 3.6 with axes bounds focusing on cluster of compositions at 65-95% PS. Filled markers indicate ^6Li doping.

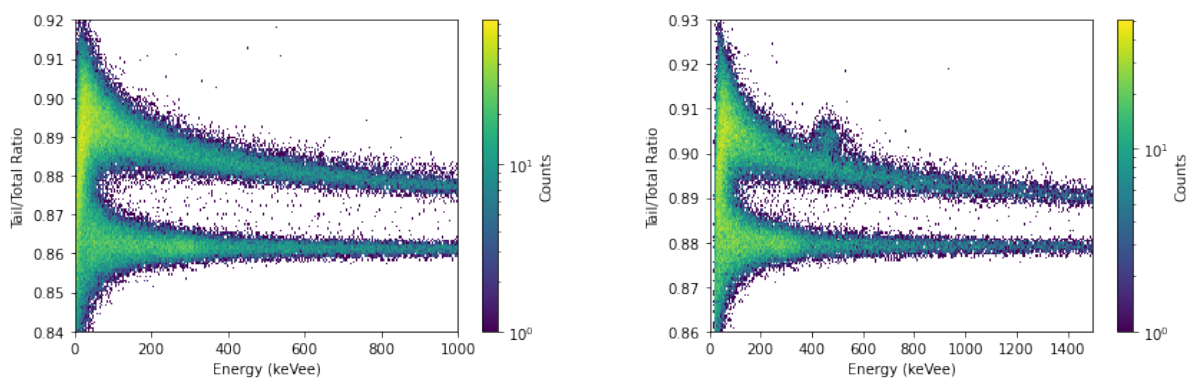


Figure 3.8: Generated PSD plots for compositions A (left) and B (right)

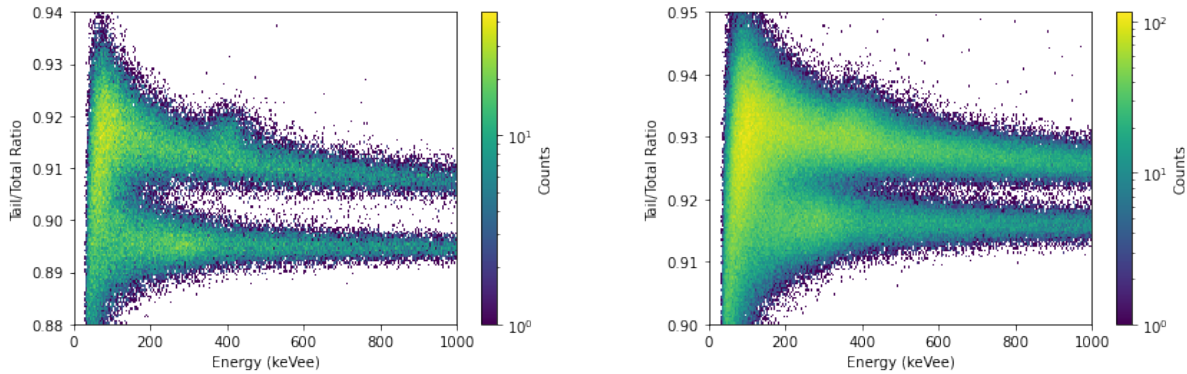


Figure 3.9: Generated PSD plots for compositions P (left) and F (right)

3.3.1.1 Curing Conditions

The results of PSD FOM evaluation as a function of curing conditions are plotted in Fig. 3.10. Composition FOM values are plotted along a horizontal axis signifying scintillator curing duration paralleled by a horizontal bar displaying the corresponding curing oven temperature. The marker convention is as previously described for Fig. 3.6. Measured PSD FOM ranged from 1.104 - 1.328, with an observed inverse relationship between FOM, and curing duration and temperature. Although all five samples were of the same composition, two met the FOM threshold criteria, namely samples K* and L*, while the remaining did not. As an important note, sample O* did have a chip on one of its readout faces, which may have influenced its measured FOM.

These results indicate the need for careful control of the scintillator curing method to ensure reliable fabrication of compositions with intended properties. For the fabrication of PSD plastics demonstrating high FOM, the results suggest greater success may be achieved by lower-temperature curing at 60°C, with a curing time of 63 hours and 20 minutes being sufficient for polymerization. Sample J*, cured for a period of only 15 hours and 20 minutes, did not result in an optically-viable sample and was noted to continue polymerizing at room temperature after removal from the oven. Thus, to identify the optimal curing duration for this composition, further study into the effects of sample curing durations between 15 and 63 hours is warranted.

The observed results indicate potential for enhancing PSD FOM through optimization of the curing method. However, as revealed in Section 3.4.3, favorable mechanical properties exhibit a different response to curing parameters. These measurements do not provide an indication as to whether the observed response can be applied generally to other compositions.

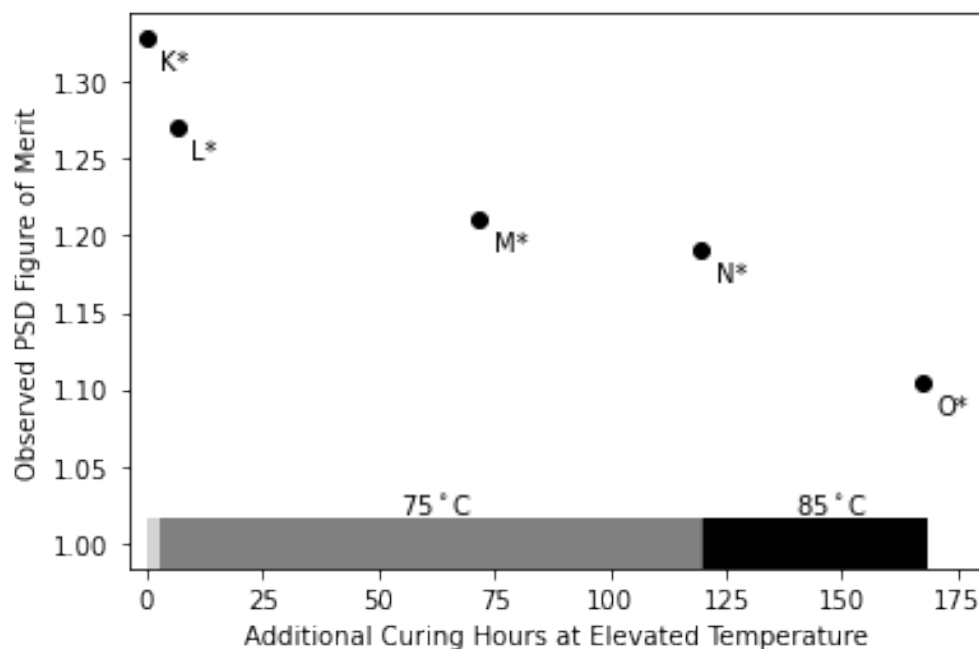


Figure 3.10: Plot of calculated PSD FOM values as a function of curing time, in hours, for curing effects evaluation samples K*-O*. Oven temperature over time is indicated by the horizontal bar above the horizontal axis, with the region between 0 and 3 hours representing the oven warming period from 60° to 75°C

3.4 Mechanical Properties Evaluation

Following PSD evaluation, the compositions were CNC-machined into SSJ “dogbone” geometry samples (Fig. 3.11) and subjected to a systematic controlled tensile testing procedure to record stress-strain relationships, from which composition-specific yield stress (mechanical strength) and Young’s modulus (mechanical stiffness) were derived. The following section describes the tensile testing procedure, analysis of measured data, and interpretation of results in the context of compositional differences and sample preparation conditions. As discussed in Section 2.5, while particular interest has been devoted to cross-linking compounds in the evaluation of compositional effects on favorable mechanical properties, the compositional scope of this work seeks to provide insight on less frequently studied compositional aspects, particularly choice of scintillator base and the effects of ^6Li -salt doping matrices.

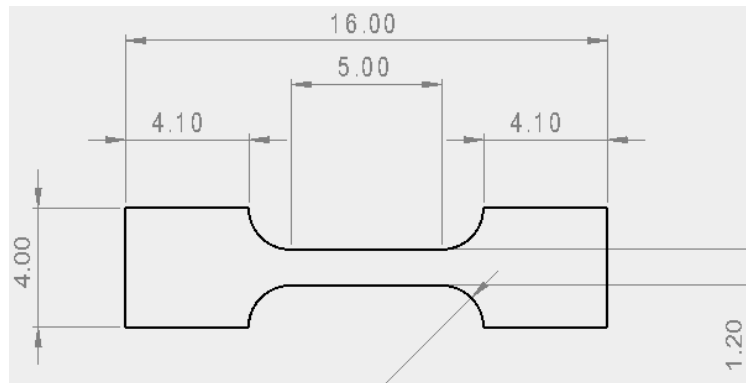


Figure 3.11: Schematic of SSJ tensile-testing sample geometry machining blueprint; dimensions in millimeters

3.4.1 Methods

Ten samples for each composition were tested using a Kammrath & Weiss Tensile/Compression Module with a 500N load cell (Fig. 3.12). Samples were pulled at a strain rate of $10\mu\text{m/s}$ until fracture, recording elongation and load converted to engineering stress (σ) and strain (ϵ) every 10 milliseconds. The obtained stress values were plotted as a function of strain for each sample, to produce stress-strain curves.

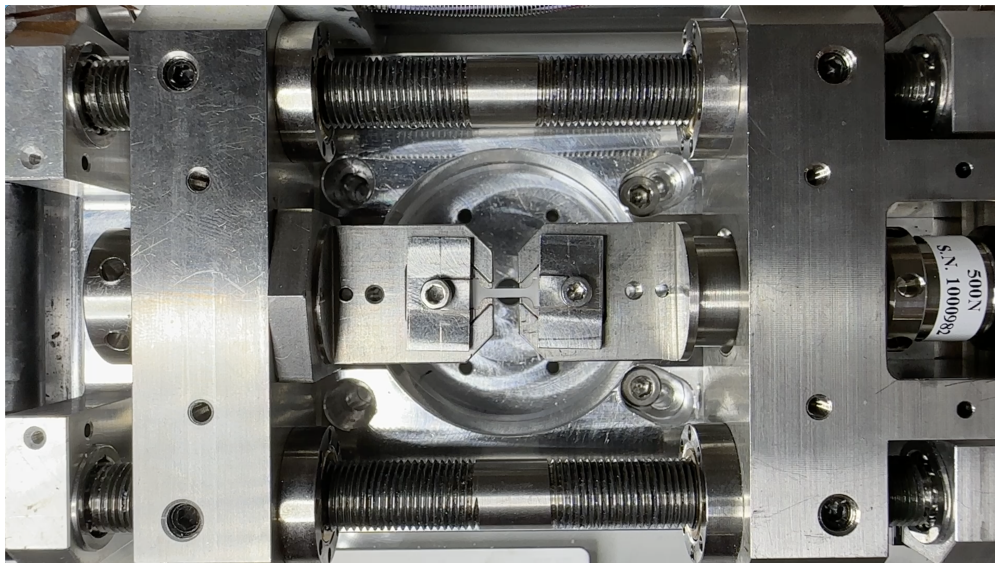


Figure 3.12: Birds-eye view of tensile/compression module containing SSJ sample of PSD plastic scintillator at its center prior to pulling

For each sample stress-strain curve, yield strength (σ_y) was determined using the 0.2% strain offset method, in which a linear extrapolation of the elastic deformation region (Fig. 3.13) was applied and offset by a 0.2% strain translation, with the intersection of the extrapolated line and the original $\sigma - \epsilon$ curve denoting the empirical sample yield strength. The slope of the elastic region, signifying the tensile (Young's) modulus of elasticity (E), was determined using a linear regression fit to the steepest 1% strain section of the curve's elastic deformation region.

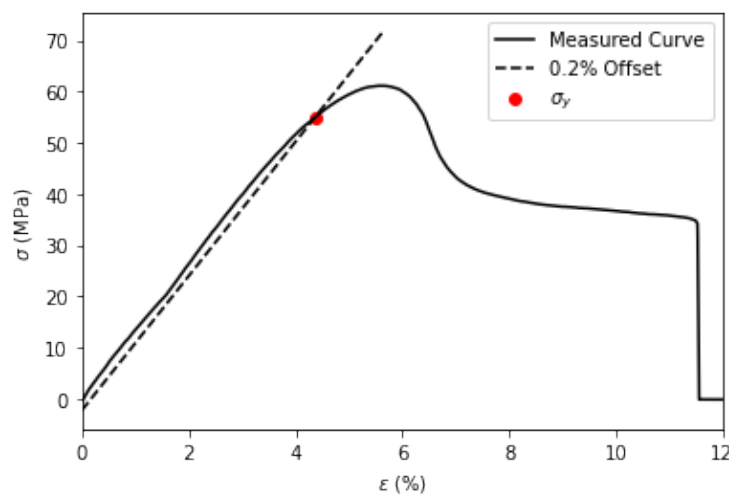


Figure 3.13: Plot of sample σ - ϵ curve of an evaluated PSD plastic SSJ sample (Composition H) demonstrating 0.02%-offset σ_y determination method

3.4.2 Mechanical Evaluation Results

The results of the mechanical evaluation: tensile strength as a function of composition and Young's modulus as a function of composition, are plotted in Figs. 3.14 and 3.15. Measured composition values are plotted along a horizontal axis signifying solvent matrix polystyrene percentage, as described for Fig. 3.6.

Acquired yield stress values ranged from 8.93 ± 1.36 MPa to 61.02 ± 6.57 MPa among the compositions, with composition E demonstrating the highest achieved yield strength value.

The compositions' calculated tensile yield strength values are plotted as a function of their calculated Young's moduli in Fig. 3.16, revealing a strong linear relationship between mechanical strength and stiffness, as expected. Calculated Young's modulus values ranged from 1.31 ± 0.23 GPa to 11.42 ± 0.84 GPa.

In general, the compositions with the highest yield strengths were PPO-dyed of PS:PMAA and PS-only base. The strengths of PS:PMAA base samples were observed to be significantly

lower for compositions containing ${}^6\text{Li}$; however all PS:PMAA compositions demonstrated mechanical strength values surpassing the 30 MPa threshold yield strength criteria for potential use as structural sUAS components. A potential relationship is identified between PMAA content and yield strength, evident when contrasting composition E, possessing the highest PMAA:PS ratio of 31:69 and the highest calculated yield strength of all tested compositions, with sample P, possessing the lowest PMAA:PS ratio of 8:92 for the composition type and a markedly lower calculated yield strength of 44.70 ± 1.86 MPa.

Samples with the lowest calculated yield strengths were the PPO-dyed with PS:PMMA base, with the lowest yield strength of the tested samples calculated for composition Q. Among compositions of this type, the ${}^6\text{Li}$ containing specimens were observed to have significantly lower yield strength values and did not meet the threshold yield strength criteria for viability as structural sUAS materials. A corresponding relationship between PMMA content and mechanical strength, similar to the one observed for PS:PMAA compositions, was not significantly observed for PS:PMMA base compositions, which may potentially be better understood with more data.

The calculated yield strengths of all other measured compositions, including non- ${}^6\text{Li}$ doped PS:PMMA compositions and both m-TP dyed compositions, met the yield strength threshold criteria. Notably, composition C** exhibited a significantly higher yield strength as compared to sample D, potentially due to its higher PS content by weight.

The results of this study indicate that for the fabrication of mechanically-capable ${}^6\text{Li}$ -loaded PSD plastic scintillators, PMAA may potentially serve as a tool to compensate for the mechanical softening resulting from ${}^6\text{Li}$ doping. However, this means of bolstering composition mechanical strength must be made in consideration of its potentially detrimental impact to PSD FOM.

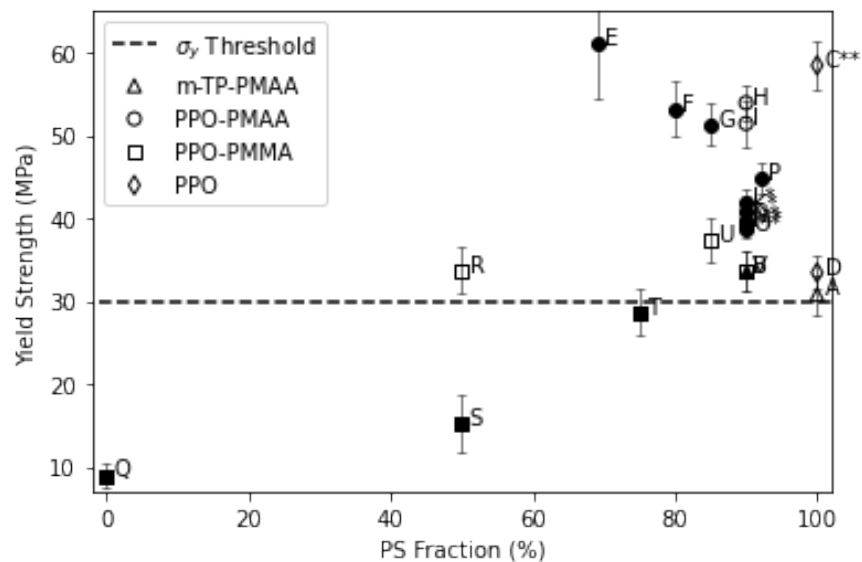


Figure 3.14: Plot of measured σ_y values in MPa as a function of PS solvent matrix percentage of evaluated compositions. Marker shape and fill are as described for Fig. 3.6

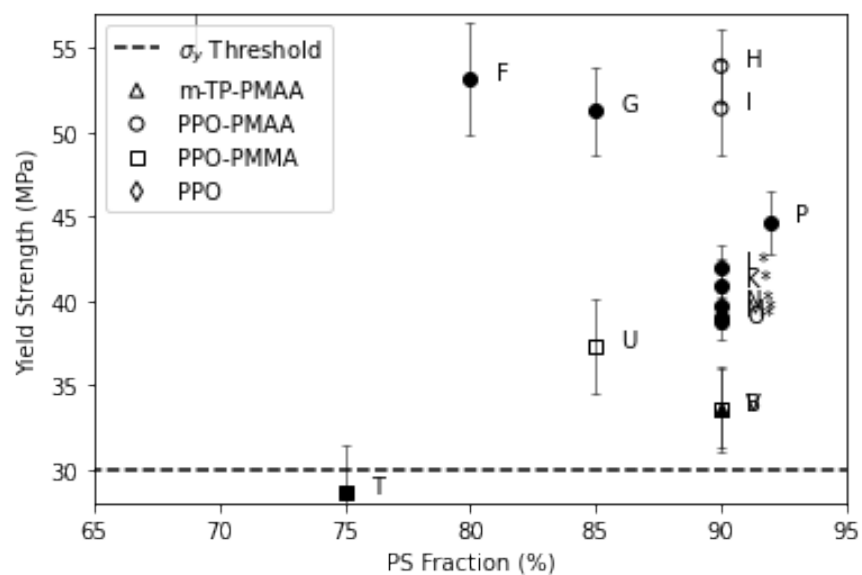


Figure 3.15: Fig. 3.14 with axes bounds focusing on cluster of compositions at 65-95% PS

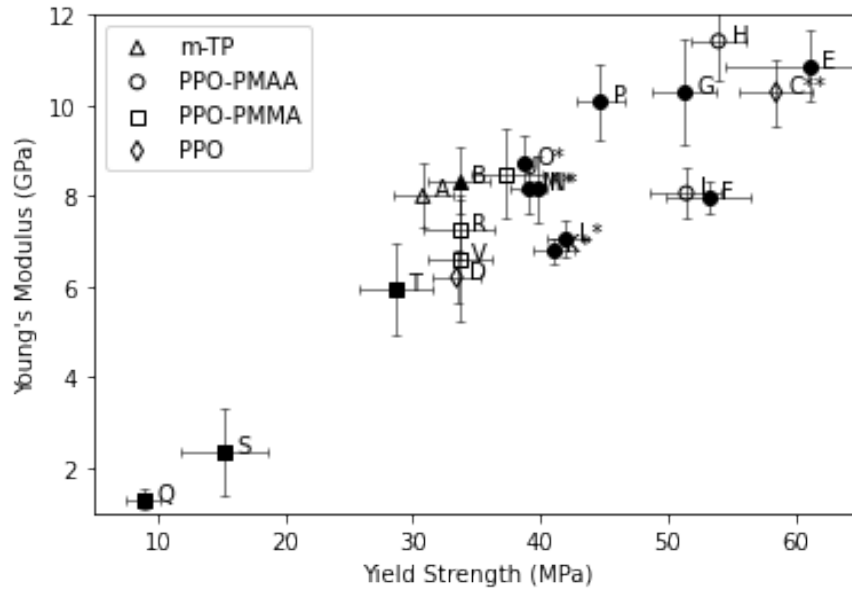


Figure 3.16: Plot of measured Young’s Modulus, in GPa, as a function of yield strength, in MPa, of evaluated compositions depicting a strong linear relationship. Marker shape and fill are as described for Fig. 3.6

3.4.3 Curing Conditions

The results of the calculated tensile strength as a function of curing conditions and calculated Young’s modulus as a function of curing conditions are visually depicted in Fig. 3.17. Measured compositions are plotted along a horizontal axis as described for Fig. 3.10. Calculated yield strength values range from 38.77 ± 0.46 MPa to 41.97 ± 1.39 MPa. While a curing-dependent decrease in strength is observed, the difference is not significant in the context of structural material selection, indicating curing temperature and duration do not significantly affect evaluated material strength. However, a significant increase in Young’s modulus is observed for samples exposed to increased curing temperatures and durations, with a difference of 28% between samples K* (6.79 ± 0.27 GPa) and O* (8.72 ± 0.59 GPa).

As discussed in Section 3.1.2, high frame stiffness is a desirable quality for sUAS construction, and thus from a mechanical perspective the results of this study indicate that scintillator curing at elevated temperatures and for prolonged durations yields materials with more capable structural properties. However, the optimization of curing conditions to enhance mechanical properties conflicts with the curing conditions observed to yield optimal PSD FOM. Therefore, the selection of optimal scintillator curing parameters is a compromise between favorable mechanical and optical traits. The characterized results do not provide an indication as to whether the observed response can be applied generally to other composition types.

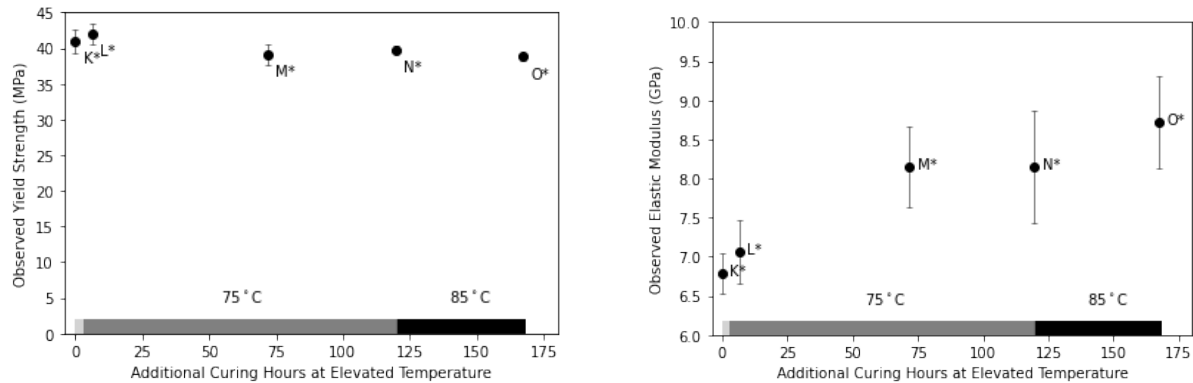


Figure 3.17: Plots of measured σ_y values in MPa (left) and measured E values in GPa (right) as a function of curing time in hours for curing effects evaluation samples K*-O*. Oven temperature over time is indicated by the horizontal bar above the horizontal axis, with the region between 0 and 3 hours representing the oven warming period from 60° to 75°C

3.5 Analysis of Results

The results from the PSD characterization and the mechanical evaluation studies can be conflated to compare the viability of the assessed compositions for use as structural detectors. The following section provides a discussion of the compositions evaluated in meeting the established PSD and mechanical criteria for further incorporation as an active-volume structural material of a sUAS frame. Attempts are made to identify potential trends relating composition-related effects to PSD and mechanical properties.

For the compositions evaluated, PSD FOM is plotted as a function of tensile yield strength in Fig. 3.18. Plot marker convention is as described for Fig. 3.6.

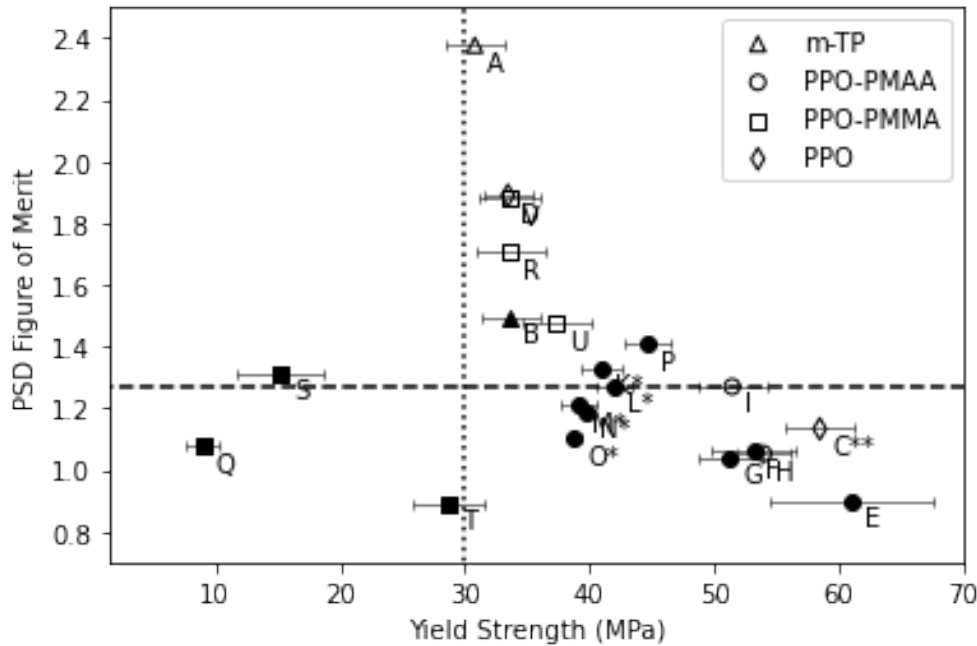


Figure 3.18: Plot of calculated PSD FOM values as a function of σ_y in MPa of evaluated compositions; separated into four quadrants by dashed lines horizontally at FOM = 1.27 and vertically at $\sigma_y = 30$ MPa. Marker shape and fill are as described for Fig. 3.6

Applying the established criteria for PSD and mechanical strength divides the plot into four quadrants, with the top left quadrant signifying compositions which demonstrate sufficient PSD FOM but insufficient mechanical strength, the bottom right quadrant signifying compositions possessing the required mechanical strength but insufficient PSD capability, the top right quadrant containing compositions meeting both mechanical and PSD criteria, and the bottom left quadrant containing compositions which demonstrate neither adequate PSD FOM nor sufficient mechanical strength for use as structural sUAS detector components.

The plotted composition properties distribution reveals three distinct regions populated by different composition types: low strength populated by ^6Li -doped PS:PMMA base compositions, high strength populated by PS:PMAA base compositions, and moderate strength with high PSD FOM populated by PS:PMMA base, as well as m-TP dyed compositions.

A notable outlier includes composition C**, demonstrating high strength but poor PSD FOM, presumably due to its lower scintillating dye content.

A general inverse relationship between PSD FOM and yield strength can be inferred from the distribution of compositions, not including those of the ^6Li -containing PS:PMAA base type. This finding indicates that even outlier results with respect to their composition type, such as composition H, abide by a consistent trade-off relationship between mechanical strength and PSD capability.

These obtained results suggest that current PSD plastic scintillator compositions can be fabricated to serve as capable active-volume structural detector materials in component applications with tensile strength requirements as high as approximately 50 MPa. The use of PSD plastic compositions for applications requiring tensile strengths higher than 50 MPa may still be fulfilled mechanically, providing detection characteristics of γ -ray and neutron particle sensitivity with the absence of low-energy particle discrimination capabilities.

Thus, for the implementation of a non- ^6Li -doped PSD plastic scintillator composition, a PS:PMMA composition containing PPO scintillating dye is favored, while for the implementation of a ^6Li -doped structural PSD plastic scintillator composition, a PS:PMAA composition containing PPO scintillating dye is favored in the construction of an active-volume structural sUAS frame, based on the obtained results.

In accordance with these findings, the chosen composition for further integration as a structural detector material for the construction of a payload-less sUAS was composition P.

Although preliminary PSD FOM and mechanical evaluation results for compositions containing m-TP scintillating dye suggest promising capabilities, a recommendation cannot be made due to the limited experimental data. This class of compositions and its range of properties, however, warrants further investigation.

3.6 Proof-of-Concept Experimental Component Replacement

With the successful identification of scintillator compositions possessing yield strength values exceeding the simulation-established minimum strength threshold of 30MPa (obtained in Section 3.1.4), an experimental verification of the simulated sUAS equipped with structural PSD plastic landing equipment was conducted. A square rod of the simulated dimensions (16" \times 1" \times 1") was provided by LLNL of a composition analogous to composition D (albeit containing 0.2 wt% bis-MSB λ -shifting dye rather than 1 wt% E404), to serve as the active-volume scintillator component landing gear. Associated hardware, including custom mounts and housings for dual-ended SiPM readout, were 3D printed of a nylon carbon fiber blend. SiPM biasing and readout printed circuit boards (PCBs) were manufactured for integration with the existing onboard NG-LAMP radiation detection payload, but ultimately not equipped for the proof-of-concept field testing. The SiPM biasing and readout board development process is described in detail in Chapter 6.

Fig. 3.19 depicts the constructed system consisting of one landing gear foot replaced by a structural PSD plastic detector assembly. For a balanced center of mass and improved flight stability, a second 16" square rod of 1" side length composed of inert PMMA was used to replace the remaining original carbon-fiber landing foot; depicted in Fig. 3.19, right.

The constructed sUAS was piloted for a series of flights, executing a variety of standard flight maneuvers at a flight speed of 1 meter per second, with controlled takeoffs and soft, level landings. The sUAS was then subjected to an impact-cycling endurance test consisting

of 20 consecutive takeoff and free-fall landings at incrementally increased altitudes, up to a maximum free-fall altitude of 1 meter.



Figure 3.19: Photos of LBNL operated DJI Matrice 600 sUAS platform depicting the replacement of a landing foot with a structural PSD plastic detector assembly (left, center), as well as the replacement of the second carbon-fiber foot with a PMMA 16” long 1” x 1” square rod (right)

During the field testing, the custom-printed mounting hardware of the detector assembly to the vertical sUAS leg experienced a shear fracture as a result of an unintended unbalanced landing, of a similar nature to the simulated uneven-landing model scenario. The mount was repaired by a bead of JB-Weld PlasticBonder and reinforced by a steel circular hose clamp (visible in Fig. 3.19, left). The impact-cycling endurance test was terminated following the completion of 20 takeoff-landing cycles, due to one of the sUAS’ motor frame arms breaking at its hinge.

No damage was observed to the PSD plastic rod as a result of its operation as the landing gear of the constructed system. In the case of the unintended uneven landing, the sacrificial failure of the 3D-printed component mount may have prevented damage to the landing gear assembly – an ultimately favorable design outcome. However, attempts during test flights to retract the landing gear into a horizontal flight configuration were unsuccessful, due to the added mass of the structural PSD plastic detection assembly.

The results obtained from field testing the constructed system indicate the predicted minimum required strength values established by the Solidworks simulated model meet or exceed the material strength requirements necessary for the construction of active-volume structural landing gear for the employed sUAS. The successful implementation of a structural PSD plastic scintillator in this application, consisting of a structurally-demanding role of a relatively heavy sUAS configuration, serves as a proof-of-concept feasibility demonstration of the capabilities of these materials for their use in constructing similar systems. However,

the demonstrated difficulty of operating the landing gear retraction mechanism reveals the challenges of 1:1 replacement of existing sUASs' structural elements, often composed of lightweight materials such as hollow carbon fiber tubes, with PSD plastic scintillators.

In the case of augmenting a high-resolution detection-payload transporting system by additional detector mass, it is likely more advantageous to utilize any available surplus carrying capacity by increasing the existing detector payload mass, rather than by the retrofitting of PSD plastics as structural components. The lessons learned in the construction and performance evaluation of this proof-of-concept system served as the catalyst for pivoting the system design focus of this work toward novel, compact payload-less sUASs composed of structural PSD plastic scintillators.

Chapter 4

Simulation-informed Geometric Evaluation

In order to determine an optimal scintillator configuration capable of serving as a structural sUAS component while maintaining particle discrimination capability, the Monte Carlo simulation toolkit GEANT4 was utilized to model radiation interactions, scintillation processes, optical photon transport, and detector readout within modeled SiPM-coupled scintillator geometries. Simulation accuracy was experimentally validated for complex tapered scintillator volumes. Following experimental validation, the constructed model was used to predict an optimal scintillator geometry for fabricating structural sUAS frame components.

4.1 Model Construction

The initial model framework was based on the GEANT4 extended optical example *LXe*, in which scintillation is simulated for a liquid xenon volume surrounded by photomultiplier tubes, with a wavelength-shifting sphere placed within the scintillator volume (Fig. 4.1). Other notable GEANT4 examples available for reference in modeling scintillation include *OpNovice 2* and *wls*.

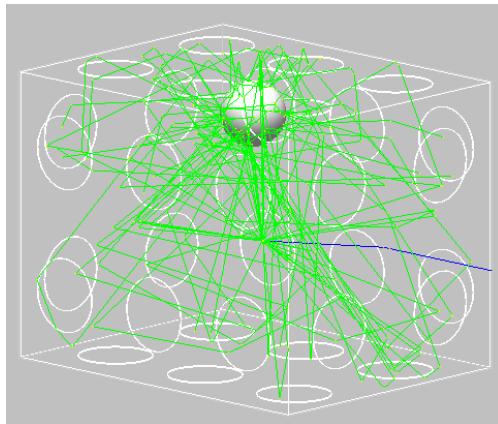


Figure 4.1: GEANT4 extended optical example *LXe*, depicting simulated scintillation photon tracks (green) generated by a primary particle (blue) interaction

To modify the model for the application of a simulated PSD plastic scintillator structural sUAS component, the wavelength shifting sphere was removed, the number of PMTs reduced from 32 to 1, and the PMT geometry altered to a square of 1.25 cm side length, reflecting the dimensions of a Sensl J-Series 6 mm 2x2 SiPM array. The scintillator geometry was modified to an elongated rectangular prism with adjustable cross-sectional and overall length dimensions.

To allow for variation of geometry in order to study volume tapering effects, two trapezoids with adjustable dimensions were adjoined to the prism at opposite ends to create a `G4UnionSolid` object (Fig. 4.2).

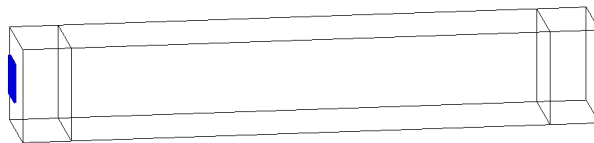


Figure 4.2: GEANT4 `G4UnionSolid` volume simulating a PSD plastic scintillator with three geometrically-adjustable sections

The radiation source was modeled as a monoenergetic γ -ray particle beam with energy of 661.7keV originating at a point. Particle emission direction was randomized within the bounds of an angular distribution enveloping the entire scintillator volume for the case of an uncollimated source configuration, or restricted to a slit for the case of a collimated source configuration.

4.1.0.1 Scintillator Properties

The scintillation emission spectrum was simulated as a distribution of three energies, with 10% emission intensity at 2.543 eV (487 nm), 100% at 2.917 eV (425 nm), and 10% at 3.024 eV (410 nm), according to the published emission spectrum of commercially-available Eljen EJ-276 PSD plastic scintillator (Fig. 4.3) [29]. The refractive index was likewise set at 1.59. Scintillation light self-attenuation length was set to 72.6 cm, and Birks constant set to 0.23 [30].

As scintillation photon generation mechanics in GEANT4 do not account for conservation of energy, scintillation light yield was set by prioritizing accurate energy spectrum generation of the theoretical 478 keV Compton edge for incident 661.7 keV photon interactions of a simulated ^{137}Cs γ -ray source. This was achieved using a value of 8,500 photons/MeV (Fig. 4.4), consistent with values in literature ranging between 8,000 – 10,000 photons/MeV [30].

To reflect the elemental composition of a PSD plastic scintillator, the detector material was specified as 47.2% hydrogen, 50.9% carbon, 0.93% oxygen, and 0.93% nitrogen by atomic fraction, with a density of 1.09 g/cm^3 [31].

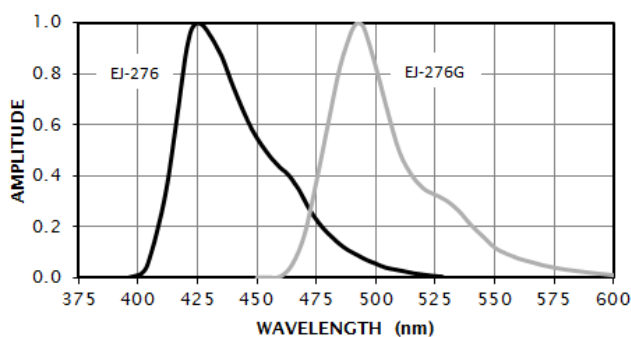


Figure 4.3: Eljen EJ-276 and EJ-276G (green-shifted) PSD plastic scintillation photon emission spectra

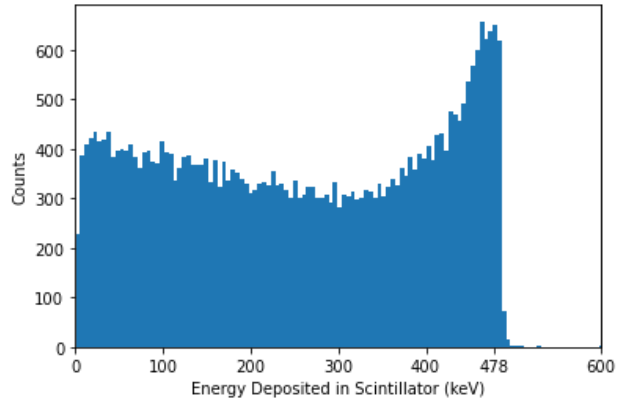


Figure 4.4: Spectrum of simulated energy depositions of Compton scattering interaction events in a PSD plastic scintillator volume, depicting 478 keV Compton edge

4.1.0.2 Surface Properties

A 0.5334 mm thick PTFE layer, of 1:2 carbon:fluorine elemental ratio composition and 1.9 g/cm^3 density, was specified surrounding the scintillator volume to model the six layers of 0.0035" thick high-density PTFE tape reflector wrapping used experimentally [32]. The material of the experimental hall volume surrounding the scintillator and wrapping was set to air.

To model the optical photon reflection characteristics of the PTFE wrapping, a G4OpticalSurface was created and set to the UNIFIED model with a ground surface finish and a dielectric_metal interface. Specular spike reflection probability was set to 0.85, and specular lobe reflection probability set to the remaining 0.15. Surface reflectivity was set to 1 and absorption efficiency to 0.

The SiPM surface was modeled as a G4OpticalSurface set to the UNIFIED model, with a ground surface finish and a dielectric_metal interface. Efficiency was set to 48.85% at 410 nm, 50% at 425 nm, and 41.1% at 487 nm [5].

4.1.0.3 SiPM Properties

The SiPM was modeled as a rectangular prism with a $12.5 \text{ mm} \times 12.5 \text{ mm}$ square readout face composed of two layers, consisting of protective glass material layer 0.37mm thick and a silicon material layer 0.09mm thick. The protective optical glass layer density was set to 2.39 g/cm^3 , and the SiPM layer material set as silicon with density 2.33 g/cm^3 [33]. Photon absorption efficiency was set as an energy-dependent distribution with respect to the three scintillation photon energies previously described, corresponding to values of 41.1% at 487nm, 50% at 425nm, and 48.85% at 410nm [5].

4.2 Experimental Validation

To assess the constructed model’s performance and tune the initial parameters used, experimental validation was performed by fabricating and characterizing three PSD plastic scintillator geometries representing different complexities of scintillator tapering configurations. All three geometries were fabricated from initial 35mm square \times 100mm rectangular prisms, cut with a bandsaw from a singular block of scintillator material. Scintillator composition was that of sample I of Chapter 3.2.

Among the three rectangular prisms, the first geometry was maintained unaltered as a high aspect-ratio rectangular prism. A four-sided 45° taper was applied to the second geometry, producing a 13 mm \times 13 mm readout face matching the surface area of a Sensl J-Series 6mm 2x2 SiPM array. The third geometry was tapered along the full scintillator length to a readout face similarly matching the surface area of an SiPM array, yielding an elongated frustum with a tapering angle of 84° (Fig. 4.5).

All shaping cuts were made using a manual miter saw under a wetted blade. The three pieces were hand-polished to surface roughness of 1 μ m using sequential 120, 320, and 600 wet sandpaper grits, followed by 9 μ m, 3 μ m, and 1 μ m diamond suspension stages on rotating polishing pads. The polished scintillator surfaces were cleaned with ethanol to remove dust and leached dye, and coupled to a Sensl J-Series 6mm 2x2 array SiPM using EJ550 optical grease. The scintillator-SiPM assemblies were wrapped in six layers of high-density PTFE tape followed by two layers of black vinyl tape, and measured for PSD.

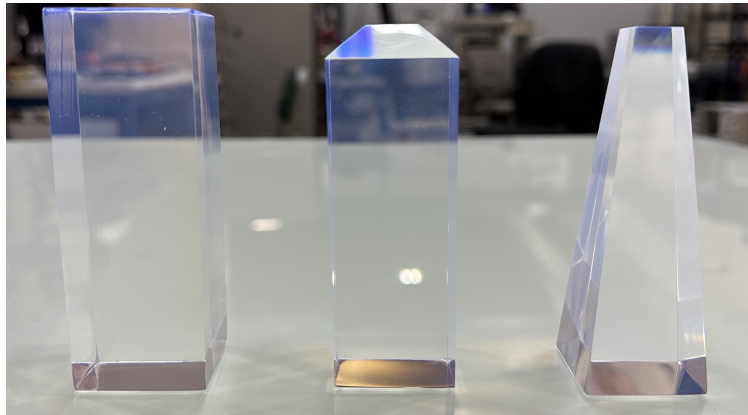


Figure 4.5: Photo of polished GEANT4 model validation experimental scintillator geometries

4.2.1 Measurements - Uncollimated

For each of the three geometries, ^{137}Cs , ^{22}Na , and PuBe sources were measured sequentially at a distance of 25.5 cm (10 inches) from the midpoint of the scintillator, to mimic the conditions of a horizontal structural scintillator sUAS component in-flight measuring a source positioned

on the ground. Twenty-minute experimental measurements were recorded for each source for each geometry, and used to characterize PSD.

The results of the experimental PSD characterization for each geometry are depicted in Fig. 4.6, containing the respective PSD plots for the unaltered rectangular prism (left) and 45° tapered rectangular prism (right), and Fig. 4.7, containing two PSD plots for the elongated frustum geometry. The left plot of Fig. 4.7 depicts measured PSD using a SiPM array coupled to the frustum’s tapered face, while the right plot demonstrates the measured PSD using a SiPM array coupled to the untapered frustum base.

The results demonstrate significant variability in the obtained PSD FOM for signal pulse energies within the 475 ± 75 keVee energy band across the three geometries. For the unaltered rectangular prism, the maximum FOM value achieved is 0.93. The 45° taper configuration demonstrated a significant improvement in FOM over the unaltered prism, to 1.13; a difference of 21.5%. The elongated frustum configuration, with the SiPM coupled to the tapered face, showed PSD FOM further improved to 1.45, while coupling of the SiPM to the frustum base demonstrated the highest achieved PSD FOM among the configurations, with a FOM of 1.52. The evaluated difference of the two scintillator-SiPM orientations demonstrates the impact of SiPM placement on PSD FOM for a tapered scintillator volume.

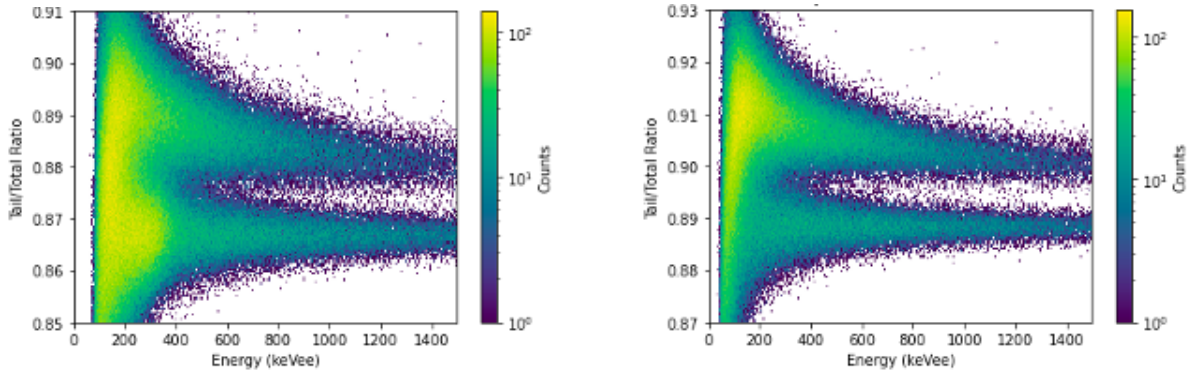


Figure 4.6: PSD Plots of $100 \text{ cm} \times 35 \text{ cm} \times 35 \text{ cm}$ PSD plastic scintillator unaltered rectangular prism (left) and 45° 4-sided readout face taper (right) configurations

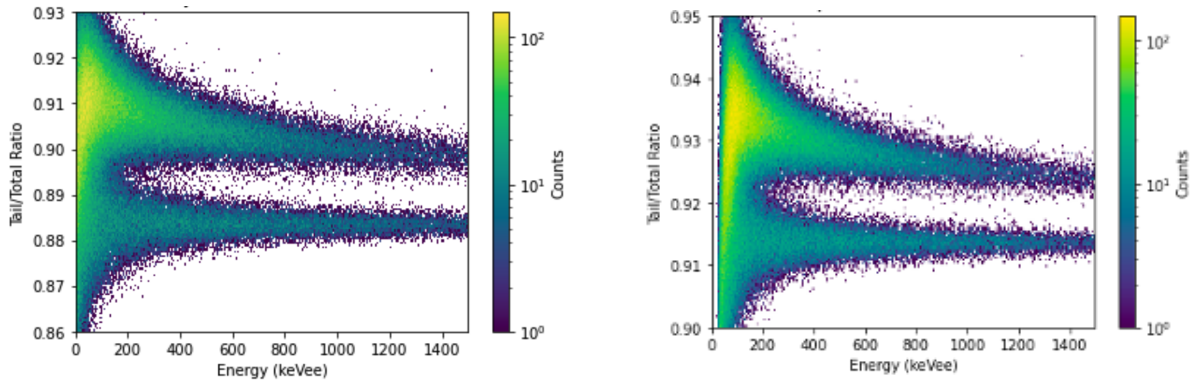


Figure 4.7: PSD Plots of 100 cm elongated frustum tapering configuration for SiPM coupled at tapered face (left) and frustum base (right)

The obtained experimental results suggest that scintillator tapering improves PSD FOM regardless of scintillator-SiPM coupling arrangement. However, the improvement in FOM was observed to be more effective for the configuration in which tapering was applied to the geometric region farthest from the readout face. This effect can be attributed both to the light-guiding geometry facilitating the redirection of surface-reflected scintillation photons toward the photodetector (Fig. 4.8), as well as the reduction of scintillator volume farthest from the readout face.

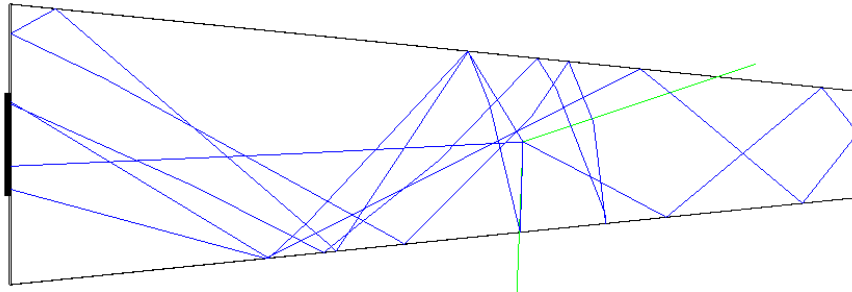


Figure 4.8: Simulated elongated frustum geometry in GEANT4 demonstrating reflection of scintillation photons toward the untapered base

The experimental measurement data were used to validate the constructed GEANT4 model by comparing simulated SiPM hits spectra to measured ^{137}Cs energy spectra. Source measurement conditions were modeled representing the three geometries, with energy deposition, number of scintillation photons generated, and number of scintillation photons detected by the SiPM, or “hits”, recorded for each simulated γ -ray scintillation event. For the elongated frustum, the SiPM was coupled to the frustum base, and incident γ -rays were

correspondingly rotated to account for the shape’s angled resting position on a horizontal surface.

In order to compare simulated energy spectra, represented as SiPM hit counts histograms, to experimental energy spectra of integrated signal pulse charge in ADC units, a scaling factor is applied to account for the conversion of collected scintillation photons to digitized electrical signal. This scaling factor, referred to as the ADC Conversion Factor, is proportional to the SiPM photon detection efficiency (PDE) in units of e^-/photon , the SiPM gain G , the number of digitizer channels $n_{channels}$, and the digitizer dynamic range (DR) in Volts (Eq. 4.1). The charge of an electron is denoted by q_e . In the constructed model, PDE is accounted for by the wavelength-dependent optical surface efficiency.

$$ADC \text{ Conversion Factor} \propto PDE \times G \times q_e \times n_{channels}/DR \quad (4.1)$$

Using this conversion factor, the GEANT4-simulated ^{137}Cs energy spectra for the three geometries are overlaid onto their respective experimental energy spectra in Fig. 4.9. By using a fixed ADC conversion factor for the three geometries, the accuracy of the model in replicating geometric effects on scintillation light collection efficiency (LCE) is assessed.

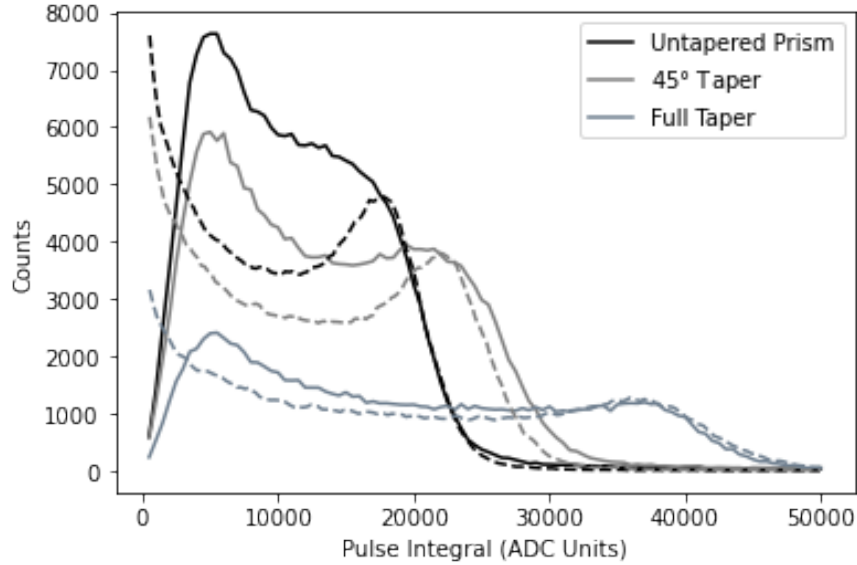


Figure 4.9: Comparison of simulated (dashed line) and experimental (solid line) ^{137}Cs energy spectra for the three model validation PSD plastic scintillator geometries, using a fixed ADC conversion factor

The model was found to be capable of reconstructing the correct shape (energy resolution) and location (relative centroid channel) of the Compton edge; the spectral feature of highest importance. However, discrepancies are evident in the lower energy regions containing the

Compton continuum, being populated by disproportionately fewer simulated counts. This is attributed to the complex surrounding experimental measurement space, resulting in room scattering effects, not being accounted for by the model, as well as the complexities of simulating nonlinear energy dependence of scintillation light yield of plastic scintillators in GEANT4. Attempts were made to reduce the effects of room scattering by orienting the experimental setup on an elevated platform distanced from walls and other objects, as in the model environment γ -rays that travel outside the experimental hall are killed to reduce computational burden.

A difference between the simulated and experimental Compton edge channel of the 45° tapered configuration, relative to the untapered and fully-tapered configurations, is apparent as well. This may be attributed to numerous factors, including inconsistencies between the hand-fabricated and simulated geometries, surface scuffs and inevitable rounding of edges as a product of hand-polishing, as well as inaccuracies in the model parameters. The specified surface model was found to significantly affect the relative centroids of the three simulated Compton edges, with increased specular spike reflection probability shifting the elongated frustum Compton edge to higher values while simultaneously diminishing separation between the untapered and 45° tapered Compton edges. Increasing specular lobe reflection probability was observed to produce the reverse effect.

To account for experimental noise, random noise was added to the simulated spectra by calculating the baseline noise variance of random experimental waveforms. Using the obtained variances, simulated noise sample values were generated using a normal distribution for a number samples corresponding to the experimental pulse sample length. The simulated noise samples were summed, and added to each ADC-converted simulated hit counts event.

4.2.2 Collimated Model Validation

In addition to comparing spectral differences between geometries, the performance of the model in predicting position-dependent effects on LCE within a scintillator volume was validated by collimating a ^{137}Cs beam at five positions along the 10cm scintillator length: 15% (1.5cm), 25% (2.5cm), 50% (5cm), 75% (7.5cm), and 85% (8.5cm), from the readout face. A collimated ^{137}Cs beam was achieved experimentally using two colinear 2-inch thick hevimet tungsten-alloy blocks arranged to form a 3.5mm gap, along which as $0.1\mu\text{Ci}$ source source was placed at a distance of 6cm from the scintillator side and centered along the scintillator's height. For each collimated source position, the scintillator was moved to position in reference to the collimated source and a twenty-minute measurement recorded. The process was repeated for all three geometries.

The experimental setup was accordingly modeled in GEANT4 by restricting the primary particle directional distribution in the Z direction. For the case of the elongated frustum, the modeled collimated photon beam's origin and direction were adjusted to reflect the scintillator's angled resting position as shown in Fig. 4.10.

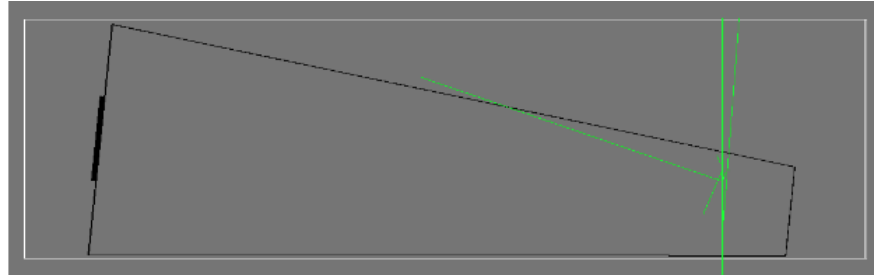


Figure 4.10: Simulated elongated frustum collimated beam rotation

The acquired simulated and experimental collimated source energy spectra for the 45° tapering configuration are compared in Figs. 4.11 and 4.12. Fig. 4.11 demonstrates the obtained raw simulated distributions of ADC-converted photocathode hit counts overlaid on the experimentally measured spectra. Fig. 4.12 repeats the comparison with representative experimental noise added to the simulated spectra.

The results demonstrate the model successfully replicates the shape of the experimentally measured Compton edge. However, similar discrepancies in the Compton continuum are observed as in the uncollimated simulated-experimental spectrum comparisons. The successful prediction of position-dependent effects on recorded energy spectra for these complex, high-aspect ratio geometries indicate more generally the model's fidelity in replicating the scintillation photon transport optical physics processes of structural PSD plastics, including attenuation, specular lobe surface reflections, and diffuse PTFE wrapping reflections.

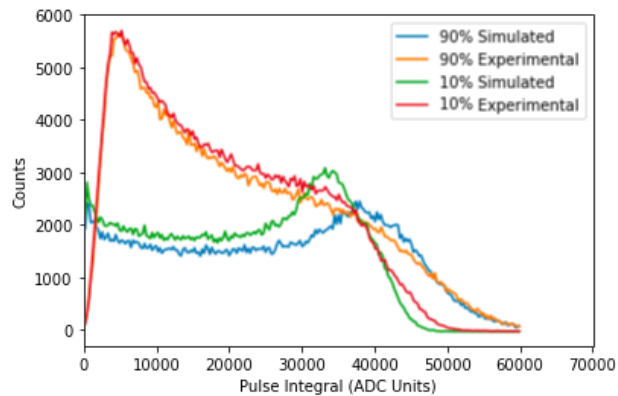


Figure 4.11: Comparison of simulated and experimental ^{137}Cs spectra at collimated positions of 10% and 90% of the scintillator length from the photocathode, for 45° taper configuration

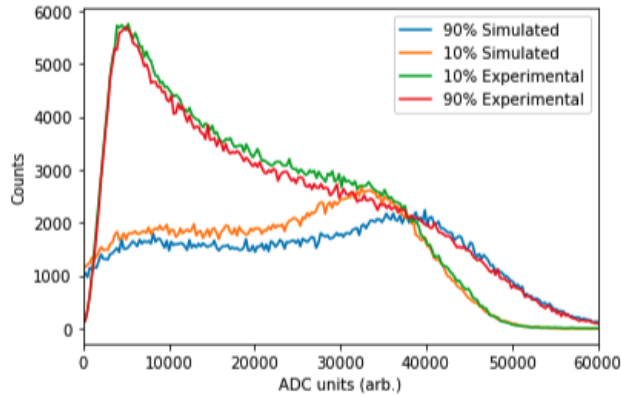


Figure 4.12: Comparison of simulated and experimental ^{137}Cs spectra at collimated positions of 10% and 90% of the scintillator length from the photocathode for 45° taper configuration, with noise added to the simulated spectra

4.3 Optimal Shape Determination

Following validation of the model’s performance in generating accurate energy spectra for the three complex experimental geometries, the model was applied to predict a scintillator geometry usable as a structural component with optimal detection properties. Of the potential common scintillator base geometries for optimization, e.g. cylinder, prism, cone, a rectangular prism was selected as flat, parallel dimensions provide practical versatility for sUAS component mounting.

The selected structural role for demonstrating the feasibility of these materials for use as structural components in a payload-less sUAS was the four frame arms of a familiar sUAS platform in DIY drone construction: the DJI F450. The platform features a modular frame composed of four structural arms secured by a pair of center plates, allowing for the progressive replacement of structural frame components by PSD plastic scintillators (Fig. 4.13).



Figure 4.13: CAD model of DJI F450 sUAS platform [34]

In order to ensure successful integration into its structural role, a structural scintillator component geometry must be optimized within the physical constraints set by the overall component assembly. Physical assembly constraints include the requirement for a minimum length to accommodate propellers of a diameter producing sufficient thrust, a minimum height for clearing detection electronics placed at the sUAS center, a region for securely mounting the four individual frame arms at the sUAS center, and a means for fastening the four motors onto the frame arms. The final physical requirement is sufficient component volume to achieve 50% active mass utilization.

The available degrees of freedom include the scintillator bulk dimensions (length, width, and height), tapering of the scintillator regions nearest and farthest from the photodetector, including the readout face, and positioning of fasteners.

Evaluation metrics for optimizing scintillator geometry include detection efficiency, average LCE, and LCE uniformity. Detection efficiency is defined as the fraction of incident radiation particles resulting in detected scintillation events. LCE is defined as the fraction of scintillation photons produced in a scintillation event that are detected by the photodetector. LCE uniformity is defined as the standard deviation of the distribution of calculated LCE values of recorded events.

Iteration of scintillator geometries with the objective of identifying an optimal shape was conducted for a set of fixed bulk dimensions, comparing simulated LCE in progressive application of the available tapering angles. For each variation, 100,000 661.7 keV γ -ray incident primary particles were simulated.

The effects of progressive tapering angles, applied to each scintillator end relative to the readout face both individually and in tandem, were assessed for an initial rectangular prism volume with bulk dimensions of 100 mm length, 33 mm width, and 33 mm height. Tapering angle was varied in 5° increments for the single-end tapered geometries. For the dual-ended tapering variations, tapering was applied to the entire scintillator length, with the junction

of the two tapers shifted in increments of 1 cm. Sample geometric variants for the three tapering types are depicted in Fig. 4.14.

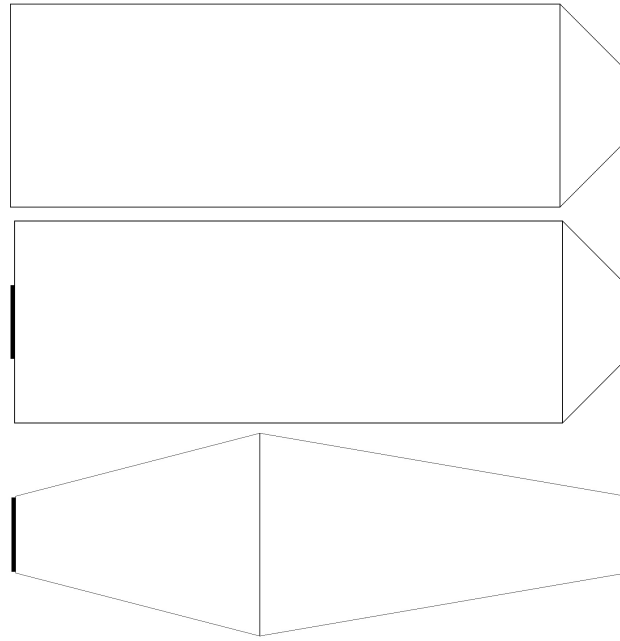


Figure 4.14: Example simulated configurations of 45° readout face taper (top), 45° taper of scintillator end opposite the readout face (middle), and dual taper with junction at 40% scintillator length from the photocathode (bottom)

The obtained LCEs for the simulated geometric variations are plotted in Figs. 4.15, 4.16, and 4.17. Significant differences in LCE and LCE uniformity were observed as a result of tapering. Tapering of the photocathode readout face resulted in improved mean LCE at moderate angles (Fig. 4.15), with maximum improvement of 2.15%, to 10.15%, when compared to the 0° taper (representing a rectangular prism) mean LCE value of 9.94%. Beyond 45°, LCE is observed to deteriorate significantly with more extreme tapering, to a minimum of 7.56% at 80°. This is likely due to beneficial light-guiding effects being outweighed by the elimination of active scintillator volume in close proximity to the photocathode.

LCE uniformity was observed to increase with applied tapering angle, from 2.15% for a rectangular prism to 5.15% for a fully-tapered volume, a difference of 140%. This indicates significant tapering of the scintillator region nearest the photocathode produces greater variability in LCE for detected radiation interactions.

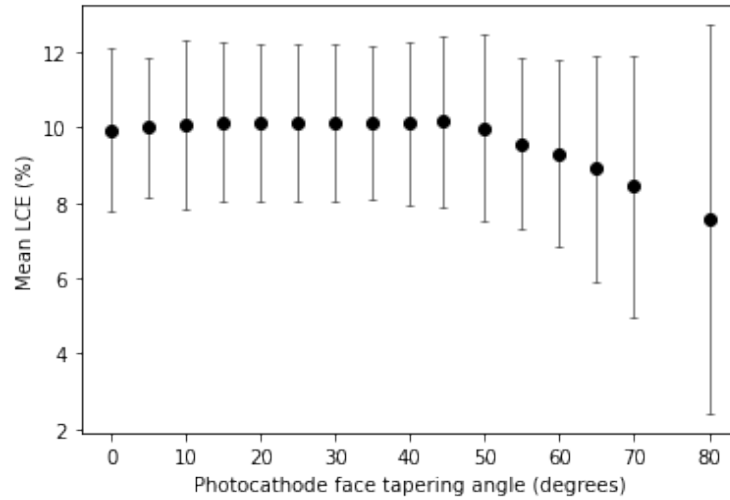


Figure 4.15: Plot of simulated LCE as a function of photocathode face tapering angle, with error bars representing LCE uniformity

The results of tapering the scintillator face opposing the photocathode readout face demonstrate significant improvement in LCE with increasing tapering angle (Fig. 4.16). A maximum LCE improvement of 60.4%, to 15.9%, is achieved using a taper of the full scintillator length. LCE uniformity increased 34.4% to 2.89% compared to the rectangular prism configuration.

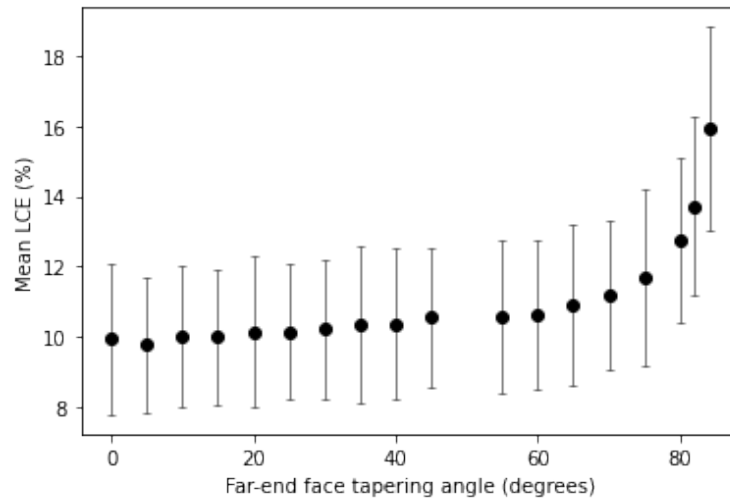


Figure 4.16: Plot of simulated LCE as a function of tapering angle of face opposing photocathode, with error bars representing LCE uniformity

The results of mean LCE obtained from applying maximum tapering to both scintillator ends for different photocathode and far-end tapering proportions, as set by the junction position, are shown in Fig. 4.17. The plotted data exhibit a complex mean LCE response to tapering proportions. The lowest mean LCE was achieved by heavily skewing the junction away from the scintillator readout face, while the highest mean LCE was achieved by a dual-tapered geometry with a junction heavily skewed toward the readout face. The optimal simulated dual-tapered geometry, in terms of mean LCE (16.1% - a 62.2% improvement compared to the rectangular prism) and LCE uniformity (2.62% - a 21.6% increase compared to the rectangular prism), was achieved at a junction position of 1cm. This result indicates that the combined use of tapers allows for the contribution of both to improving mean LCE.

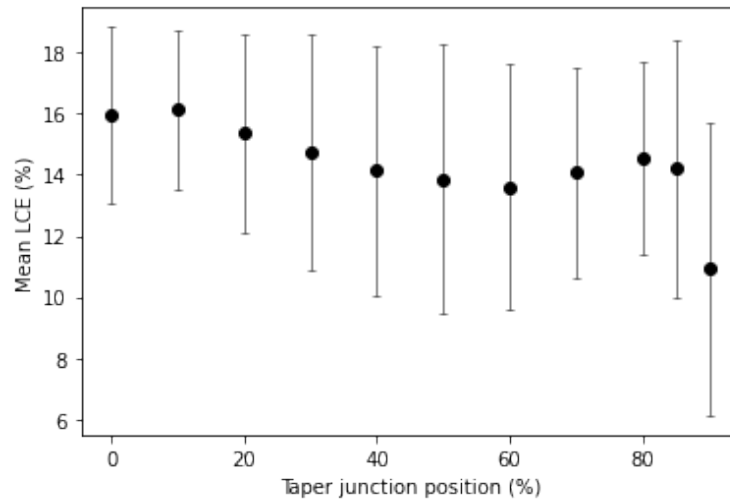


Figure 4.17: Plot of simulated LCE as a function of dual-ended tapering junction position, with error bars representing LCE uniformity

The results obtained of the three tapering configuration studies indicate tapering of both ends of the scintillator volume provides an improvement to mean LCE, with the majority of the improvement attributed to the effects of tapering the region farthest from the readout face. A 62.2% increase in mean LCE was achieved by optimal tapering of the initial representative rectangular prism dimensions, corresponding to an applied taper of 45° to the readout face and a pronounced taper of the opposite scintillator end. More significant improvements to mean LCE may be achieved by tapering the scintillator region farthest from the readout face to a point, as opposed to a $12.5 \text{ mm} \times 12.5 \text{ mm}$ square. The evaluated geometries, however, were intentionally selected to investigate tapering effects with respect to photocathode orientation.

While an optimal simulated scintillator geometry was derived for the established set of bulk dimensions, modifications must be made for practicality of implementation as a

structural sUAS frame component. Namely, the necessary modifications include mounting compatibility to other frame components at the sUAS center, and means for securing thrust-producing motors with propellers.

To enable secure mounting, a region of 2.5 cm (one inch) length containing parallel faces near the photocathode was incorporated to accommodate surface area for effective clamping of the component in place at the frame center. The presence of this section reduces the extent of the tapers, reducing overall LCE and LCE uniformity to $13.1\% \pm 2.14\%$.

Commercial sUAS motors are mounted to frame arms by a set of (usually four) machine screws. Mounting of the motors to the scintillator component thus requires the incorporation of a set of screw holes at the far scintillator end (opposite the photocathode), as well as a horizontal surface to which the motors will be secured. This requirement in effect further restricts available tapering of the far end of the scintillator.

The bolt pattern of the utilized sUAS motor was incorporated into the GEANT4 model as a set of cylinders of two diameters (corresponding to the thread and bolt head diameters) centered between the three scintillator side edges, applied as a G4SubtractionSolid to the unified shape.

Simulation results of the geometry incorporating sUAS motor mounting bolt holes yield a mean LCE value of $13.0\% \pm 2.21\%$; indicating a decrease in mean LCE of 0.85% and a 3.27% increase in LCE uniformity as a result of the addition of the four holes. The relatively minor reduction in mean LCE is likely due to the holes' positioning through the scintillator region farthest from the photocathode readout face. The increased variability in the LCE distribution may be attributed to both the beneficial effects of the holes in artificially reducing overall scintillator length by reflecting scintillation photons toward the photocathode, as well as the detrimental effects of creating an obstacle for scintillation photons "behind" the holes in reaching the photocathode.

The resulting generalized optimal geometry, incorporable as a structural sUAS frame component, is the tadpole shape displayed in Fig. 4.18. In comparison to the untapered rectangular prism, simulated mean LCE is improved by 30.8%, with LCE uniformity increasing by 2.79%.

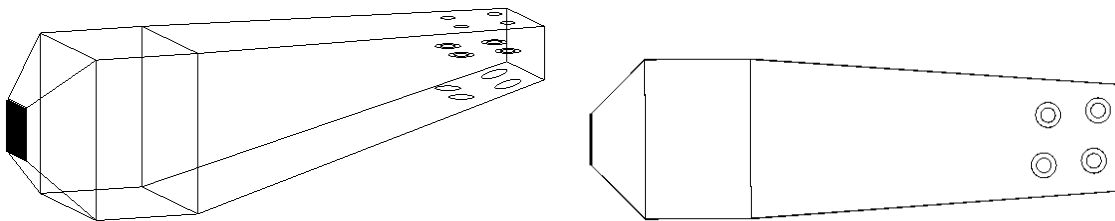


Figure 4.18: Optimized sUAS structural component scintillator geometry

It is important to note that in addition to optimization of geometry and scintillator-photocathode orientation, LCE can be improved by using additional photocathodes or by

increasing the photocathode surface area. However, the implementation of this approach must take into consideration that a constructed sUAS contains four scintillator arms, and thus the use of multiple photocathodes, or SiPMs, per arm can quickly render the system or multiple-unit construction cost-prohibitive.

Chapter 5

sUAS Construction

Construction of a sUAS composed of active-volume structural elements synthesizes the results of the optimal composition selection together with the optimal simulated scintillator geometry. Development of the final system can be categorized into three modules:

1. Active-volume structural frame fabrication
2. Detection electronics, associated circuitry and data communication
3. Power, propulsion and flight control

The following chapter discusses the component selection and physical integration of these modules into an operational assembled system. A detailed discussion of the detection electronics, associated circuitry, and data communication is contained in Chapter 6.

5.1 Active Frame Fabrication

Bulk material in the form of two 3-inch \times 3-inch \times 9.5-inch blocks was received from Dr. Natalia Zaitseva and Dr. Michael Ford of LLNL. The compositions of the two blocks are listed in Table 5.1. Both compositions contain 5 wt% DVB cross-linking agent.

Label	Solvent/Base	Primary Dye	γ -shifting Dye	^6Li Content
1	PVT	30% PPO	0.2 wt% bis-MSB	
2	90:10 PS:PMAA	30% PPO	0.2 wt% bis-MSB	1.5% 1.7 wt% ^6Li -isovalerate

Table 5.1: Compositions of received PSD plastic bulk material for structural sUAS component fabrication

The blocks of bulk material were cut longitudinally using a bandsaw into four 1.5" \times 1.5" \times 9.5" sections (Fig. 5.2).



Figure 5.1: Left: Photo of bulk scintillator material block, composition 1. Center: Photo of bulk scintillator material block, composition 2. Right: Photo of bulk scintillator material block, composition 1, illuminated by UV lamp.

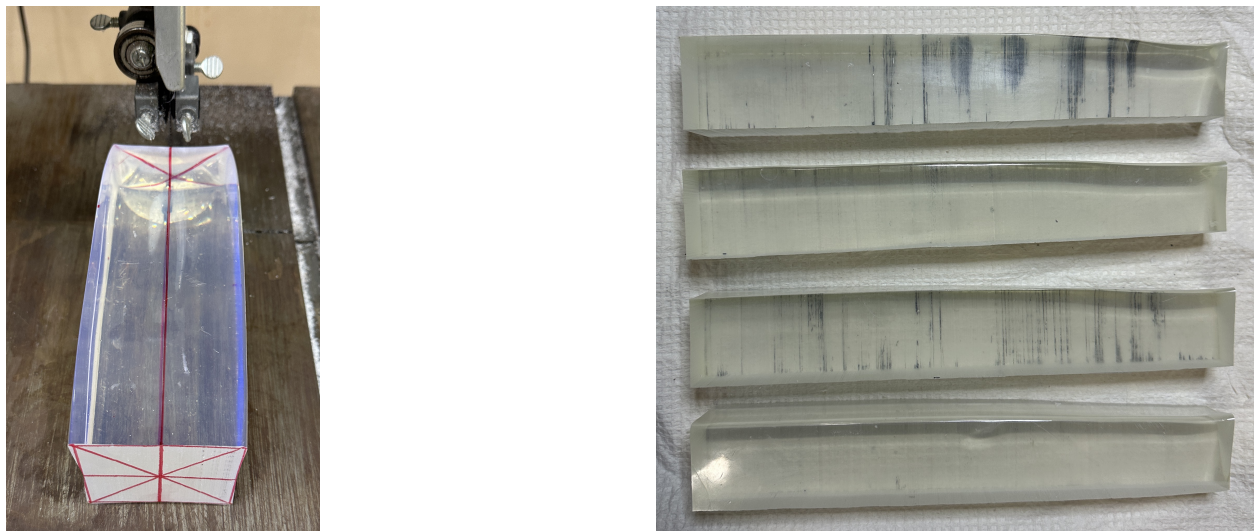


Figure 5.2: Left: Photo of bulk scintillator material block (composition 2) in preparation for bandsaw cuts. Right: $1.5'' \times 1.5'' \times 9.5''$ cut sections

Following optimization of potential volumes through GEANT4 simulation, the four sections were reduced to a length of 5" using a manual miter saw. A 45-degree cut was made on all four sides of one scintillator end face to create the tapered SiPM readout face. Three additional cuts were made to shape the bulk taper, while maintaining a region one inch in length for two parallel faces (top and bottom) in between the SiPM and bulk tapers necessary for securing the components to the sUAS center.

The top and bottom faces of each arm were sanded parallel using 60 grit sandpaper. Four holes were then drilled using a drill press to accommodate M3 hex bolts for motor mounting. Each hole was drilled using a 1/8" bit for the motor bolt thread diameter, followed by a 0.31" bit to create a recess for the bolt head (Fig. 5.3).

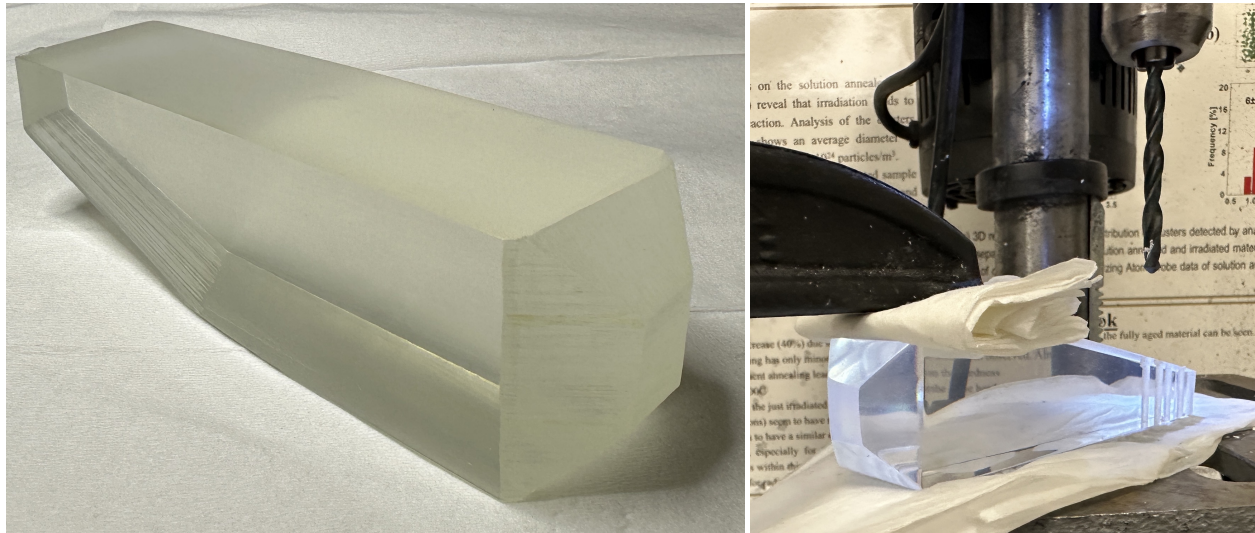


Figure 5.3: Left: Photo of PSD plastic cut to structural sUAS component geometry. Right: Photo of drill pressing motor bolt holes into PSD plastic scintillator component

The cut and drilled sUAS structural scintillator arm geometries were then mechanically hand-polished, as described in Chapter. 4.2, using a succession of 120, 320, and 600 sandpaper grits, followed by $9\mu\text{m}$, $3\mu\text{m}$, and $1\mu\text{m}$ diamond suspensions on a Buehler microfiber polishing pad using a 10" rotating polisher machine. The polished scintillator components are photographed in Figs. 5.4 and 5.5.

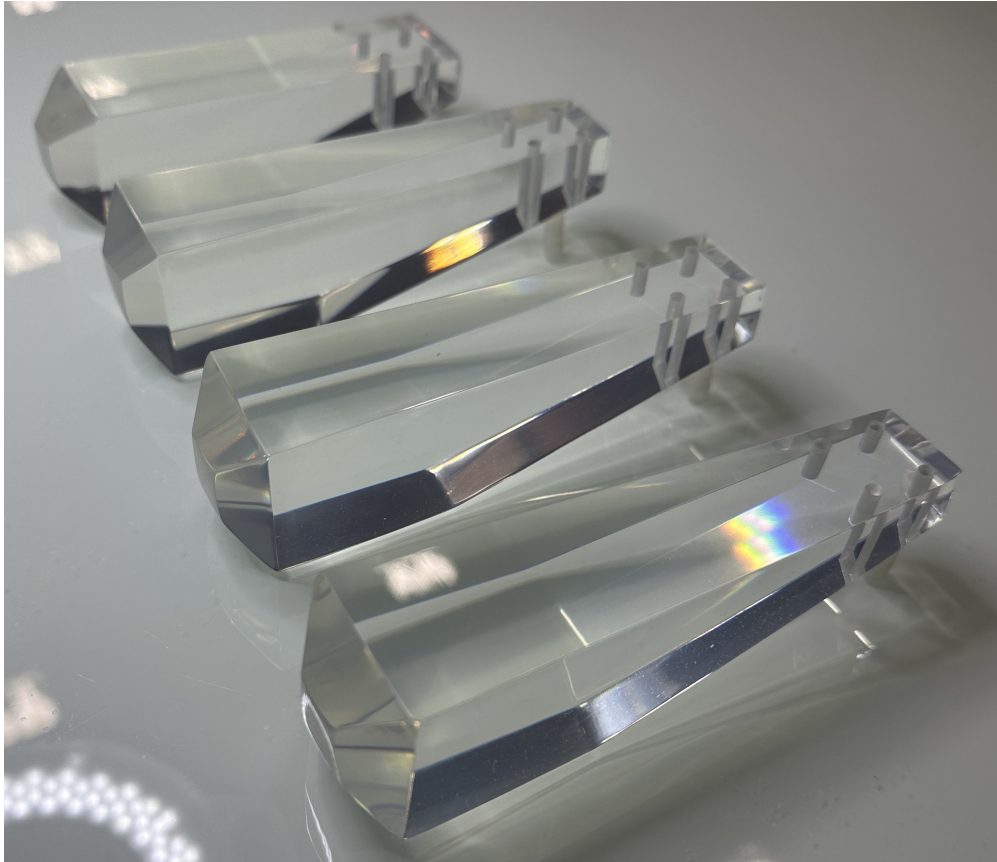


Figure 5.4: Polished PSD plastic structural sUAS components

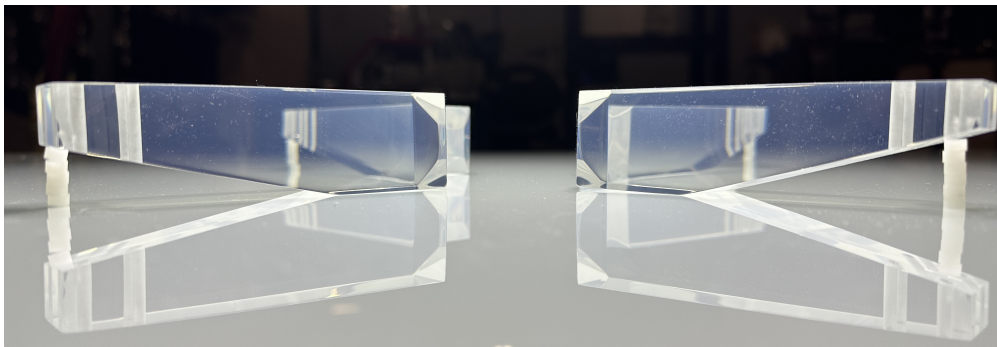


Figure 5.5: Polished PSD plastic structural sUAS components

Four M3 machine screws were wrapped in two layers of high-density PTFE tape, and inserted into the drilled holes. The polished scintillators were surface-cleaned with ethanol,

coupled to Sensl J-Series 6mm 2x2 SiPM arrays using Eljen EJ-550 optical grease, and wrapped in six layers of high-density PTFE tape. To seal the assembly from sunlight, the components were then wrapped in 3 layers of EJ-554 black vinyl tape.

The exposed SiPM pins were connected to individual biasing and readout printed circuit boards (PCBs). A detailed discussion of the PCB development is contained in Chapter 6. The connected readout boards were wrapped by an additional layer of black vinyl tape, followed by a layer of conductive adhesive-backed copper tape (later electrically-grounded to the sUAS), and a final layer of black vinyl tape (Fig. 5.6).

A bead of Permatex Ultra Black Silicone Gasket Maker was applied to the protruding motor mounting bolts, following which the sUAS motors were secured and allowed to cure for 24 hours. Two additional layers of black vinyl tape were applied to the motor hole access site.



Figure 5.6: Photo of optically-sealed PSD plastic structural sUAS component assembly

The four scintillator arms were arranged surrounding a nanoPSD spectrometer in a 90-degree X-frame. To maintain frame alignment, two 2mm thick carbon fiber sheets were cut into an X shape, arranged above and below the scintillator arms, and secured using reinforced adhesive tape.

5.2 Detection Electronics, Associated Circuitry, and Data Communication

The detection electronics, associated circuitry, and data communication module consists of: SiPM biasing and readout circuitry, a labZY nanoPSD real-time PSD spectrometer, and a Raspberry Pi Zero 2 W onboard computer.

The nanoPSD spectrometer is positioned at the center of the sUAS active frame, in between the top and bottom carbon fiber sheets, for maximum physical protection and

minimization of required signal cable length (Fig. 5.7). The Raspberry Pi companion computer as well as the SiPM bias and readout boards are mounted onto the center of the top carbon fiber sheet and below the flight controller, in between the flight controller's vibration-dampening foam mounts.

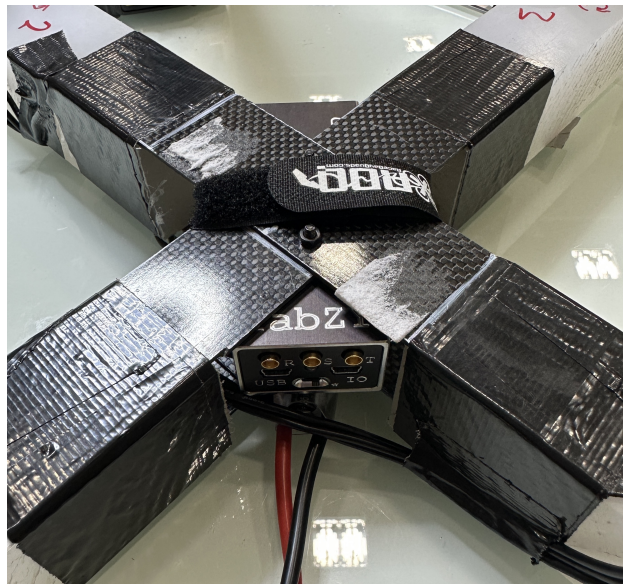


Figure 5.7: Photo of spectrometer location at sUAS center, with non-scintillator plastic frame arms for prototyping

Power and serial TX/RX data links are provided to the Raspberry Pi's GPIO pins via the Pixhawk Cube Orange Telem 2 port connection. The nanoPSD is connected to the Raspberry Pi's microUSB port for power and data communication. Power is separately provided to a central SiPM bias and readout board from the electronic speed controller's (ESC) battery elimination circuit (BEC) 5V output, and distributed to the four peripheral scintillator component assembly PCBs.

5.3 Power, Propulsion, and Flight Control

5.3.1 Components

The Power, Propulsion, and Flight Control module consists of a CubePilot Pixhawk Cube Orange flight controller and carrier board, a Pixhawk Power Module, a CubePilot Here3 GNSS, a HOBBYWING XRotor Micro 60A 4in1 BLHeli-32 DShot1200 electronic speed controller (ESC), four BrotherHobby Avenger 2812 V3 1115kV motors, and a RFDesign RFD900x-US Telemetry Bundle.

Autonomous mission flight is made possible through the utilization of an on-board flight controller housing a computer processor alongside accelerometers, gyroscopes, compasses, and barometric pressure sensors, supported by a wireless link to a ground control station. Commercially-available HEX Pixhawk Cube Orange was selected for its sensor redundancy and control using open-source Ardupilot firmware.

In addition to the flight controller, a wireless link is needed for commanding the sUAS to perform complex flight maneuvers, such as the execution of self-guided flight along a programmed course. Telemetry commands are transmitted to the flight controller from a ground control station operating either Mission Planner or QGroundControl ardupilot-compatible software. The wireless link is established using a pair of RFD900X 915MHz radio telemetry.

Telemetry communication was initially accomplished using 100mW Holybro Telemetry V3 modules; however concerns regarding signal strength at range and around obstacles prompted migration to the higher-power (1W) dual-antenna RFDesign RFD900X transmitter-receiver modules with noise filtering.

A CubePilot Here+ RTK Base station is used in conjunction with the onboard Here3 GNSS to provide centimeter-scale positional resolution. Battery choice is mission-dependent, with experimental most flights powered by a HRB 6S 22.2V 3300mAh 60C XT60 RC Lipo battery.

The sUAS' onboard electronics are arranged in a vertical stack configuration at the center of the system, depicted in Fig. 5.8. The Pixhawk Cube Orange flight controller and carrier board are mounted at the center of the sUAS frame to the top carbon fiber sheet using vibration dampening foam, with the Here3 GNSS mounted atop the flight controller using vibration-dampening foam. The GNSS is connected to the flight controller via the CAN 1 port. For improved signal integrity, the GNSS' compass is utilized for flight, replacing the default flight controller compass.

Note: GNSS dial-in time and positional resolution were significantly improved by a firmware update to M8P, not present on the factory-provided modules.

The ESC is bolted to the bottom carbon fiber support sheet, below the nanoPSD, using nylon spacers to provide ample space for heat dissipation. The battery is mounted below the center of the sUAS using two Velcro straps, and fitted with an adhesive-backed shock-absorbing resilient polyurethane foam strip, 3/32" thick and 2" wide, to protect against impact during landings and takeoffs.

To reduce signal interference by transmitting antennas, the telemetry radio is mounted below the motor on frame arm 1 using 3M VHB double-sided adhesive tape.

The flight controller is flashed with Ardupilot ArduCopter 4.3.6 firmware. Remote communication with the sUAS is conducted from a 2021 Apple M1 Macbook Pro ground station computer (GCS) operating QGroundControl software, powering a local RFD900x telemetry module via a FTDI-USB cable as well as a Here+ RTK base station via a CAN-USB cable.

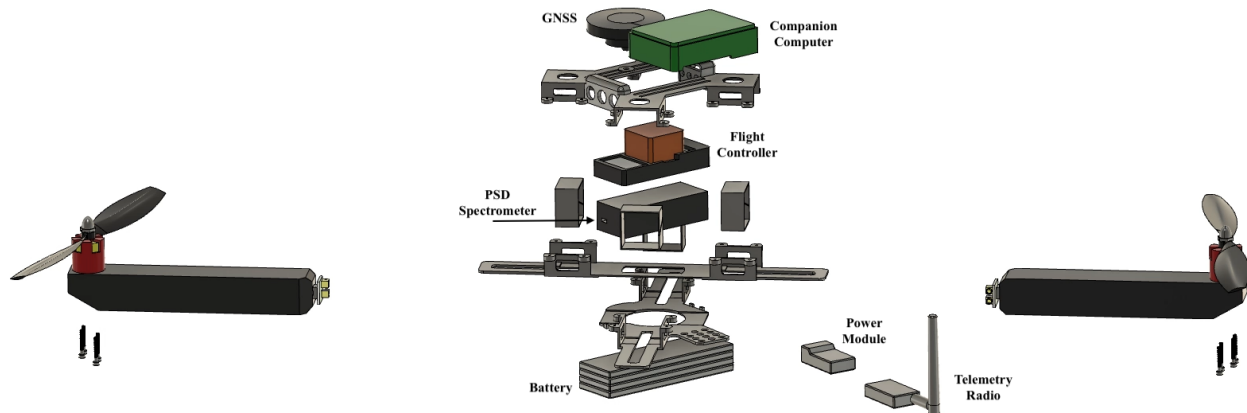


Figure 5.8: Exploded component diagram of sUAS vertical center stack arrangement

5.3.2 Equipment Considerations

5.3.2.1 Thrust

For multi-rotored sUASs, the key metric used to assess power requirements is the system's thrust-to-mass ratio. The recommended thrust-to-mass ratio value is generally stated as a minimum of 2 for cinematic and payload-carrying systems, with ratios of 3 and above often achieved by acrobatic and racing-oriented systems. A thrust-to-mass ratio of 2 can alternatively be interpreted as the ability of a system to hover mid-air at 50% applied throttle.

The total thrust of a quadcopter can be calculated as the sum of the individual thrusts generated by the four motors and propellers. For a 2:1 thrust:mass ratio at 100% throttle, the required thrust per motor is one half of the system's takeoff mass. The total weight of the constructed structural-scintillator sUAS is given in Table 5.2. For an assembled system weight of 1968.2 grams, motors and propellers are required with a minimum individual thrust rating of 984.1 grams. This requirement is met by the employed BrotherHobby Avenger V3 1115kV motors, providing 1090g of thrust when mated to 9" diameter, 4.7" pitch carbon fiber two-bladed propellers [35].

Table 5.2: Table containing measured component masses of the constructed sUAS

Component	Mass (grams)
Active Mass Frame	800
Flight Controller	73.7
GNSS	48.3
4-in-1 ESC	15.0
Motors	306
Telemetry Radio	14.5
PSD Spectrometer	127.7
Raspberry Pi	11
SiPM bias/readout boards	20
Power module	15
Propellers	40
Wiring	20
Mounting Hardware	10
6S 22.2V 3300mAh Battery	467
Total (no battery)	1501.2
Total (inc. battery)	1968.2

5.3.2.2 Battery Capacity

The necessary battery capacity for a specified flight duration can be calculated by multiplying the average power draw of the motors by the flight duration. In the absence of experimental power consumption data, an estimate can be performed for the system's hover duration from the quoted power draw of the motors at a thrust value equal to the sUAS mass. For the assembled system mass, this value is calculated as $1968.2g/4 = 492.05g$ thrust per motor. For brushless DC electric motors, generated power is a linear function of current (throttle), allowing the required hover thrust to be interpolated to 33.7% throttle and 3.68A current at 24V from the manufacturer specification sheet. Power consumption at hover is thus calculated to be 88.4W per motor, or 353.6W total. Hover flight duration can then be estimated as a function of battery capacity divided by the hover power draw. For a 3300mAh 22.2V nominal battery equipped by the constructed system, estimated hover time is 9 minutes and 20 seconds.

5.3.3 Thermal Considerations

Accounting for heat the generation of onboard components is of utmost importance for ensuring reliability of operation, as well as stability of temperature-dependent SiPM gain and signal integrity. Heat is generated by onboard components primarily as a byproduct of electrical resistance arising from current flow. The components responsible for the most

significant heat production are therefore the ESCs, motors, and the battery. Insufficient heat dissipation from these components can result in degradation of flight control and performance, reduction of component lifespans, loss of motor power, and potential catastrophic system malfunction leading to property damage and a fire risk. Concerning SiPM performance, increased system temperature negatively affects signal gain, resulting in degradation of low-energy PSD capability [5].

Heat dissipation in the sUAS is primarily fulfilled by the downward airflow generated by the propellers during flight. As such, the motors typically experience optimal ventilation and are not prone to overheating when operated within their rated current and voltage limits. Positioning of the battery below the sUAS frame provides protection from direct sunlight exposure and facilitates cooling via the downward airflow from the propellers. Therefore, ESC heat dissipation is the most challenging factor, due to its positioning at the frame center.

A central 4-in-1 ESC configuration is utilized in the sUAS. Initial prototypes included four individual QWinOut 40A ESC 2-4S ESCs mounted on the four frame arms; a more advantageous configuration from a heat dissipation standpoint. However, the 4-in-1 ESC is ultimately favored due to its lower mass (reducing total ESC mass from 92.8g to 15.0g), fewer and shorter battery-ESC current carrying wires, no requirement for a power distribution board, and a smaller and more protected footprint. Such a consolidated footprint and central placement on the sUAS, rather than directly under the propellers, however results in concentrated heat production and limited available airflow.

To account for this dynamic, the 4-in-1 ESC is mounted at the frame center with 0.25" nylon vibration-dampening bushings above and below the ESC board, providing adequate spacing for airflow. The employed 4-in-1 ESC is intentionally "oversized" to maintain current well below capacity with its 65A continuous, 80A peak rated current limits. As a reference, a total system motor current of 35.6A is interpolated to produce sufficient power for a 2:1 thrust:mass ratio from the motor specification sheet, with 14.7A total current at hover.

5.4 RF/EMI Mitigation

Electromagnetic interference (EMI) arising from both onboard-generated and externally-generated (e.g. power lines, radio towers) electromagnetic fields can significantly affect the sUAS' performance and jeopardize reliable operation by distorting communication signals and vital onboard sensors. Symptoms of a sUAS inadequately protected from EMI include reduced telemetry range, erratic flight behavior, onboard component "brownouts", and loss of GPS-guided flight ability. Different components have varying sensitivities and consequences to electromagnetic interference. To ensure proper component functioning in a compact sUAS system, extensive measures must be taken to limit electromagnetic fields and reduce component sensitivity to EMI. Available tools in this effort include avoidance of external EMI sources, conscientious onboard arrangement of EMI-producing and EMI-vulnerable components, use of EMI shielding, and optimal antenna placement and orientation.

5.4.1 Affected Components and Significance

The constructed sUAS contains EMI-producing components and EMI-sensitive electronics in a compact platform in which the simplest solution for reducing EMI - increasing distance between components - is not feasible. Consequently, careful consideration must be made to identify the most vulnerable EMI-sensitive onboard components in order to develop a robust approach for mitigation. EMI-susceptible components vary in their sensitivities to electric (E) and magnetic (H) fields, broadband EM frequency noise, and narrow-band EM frequency noise. Some components may be resistant to certain fields, such as SiPM H-field insensitivity, while others are susceptible to all forms of EMI, such as unprotected signal wires. Different approaches are available for mitigating electric and magnetic interference.

5.4.1.1 Flight Controller

The component of primary concern in EMI mitigation is the flight controller. The sUAS flight controller contains delicate sensors including inertial measurement units (IMUs) composed of accelerometers and gyroscopes, barometers, and a magnetometer (compass) which provide precise real-time measurements of the aircraft's position and orientation. The flight controller continuously assesses the aircraft's status and makes adjustments to maintain the intended flight course. The presence of electric fields can induce stray currents distorting accelerometer, gyroscope, and magnetometer readings, while magnetic fields can produce erroneous forces on accelerometer and gyroscope sensing elements resulting in incorrect readings, in addition to disrupting the magnetometer's reading of Earth's magnetic field. EMI can introduce noise leading to voltage fluctuations, as well as impacting effective functioning of the flight controller's computer.

5.4.1.2 GNSS

The sUAS GNSS allows provides the system with its real-time global position to enable autonomous mission execution capability. Maintenance of satellite signal integrity is of critical importance for autonomous flight, with loss of GPS lock often arising from tall structures and external EMI sources such as power transmission lines. The presence of EMI can reduce the signal-to-noise ratio (SNR) of received satellite signals.

5.4.1.3 Telemetry

The sUAS telemetry radio allows for wireless communication between the sUAS and the ground station. EMI can affect signal strength resulting in reduced maximum range, loss of data packets, "lag" in execution of commands and course adjustments, and potential loss of wireless contact with the sUAS.

5.4.1.4 ESCs

Uninterrupted communication between the flight controller, ESCs, and motors is vital for stable flight. EMI can induce noise and degrade signals resulting in missing or incomplete motor control commands sent to from the flight controller to the ESCs. This can cause erratic motor behavior and speed variations, misfires, inefficient regulation of motor power leading to components overheating, and potential loss of motor control.

5.4.1.5 Computer Processors

A significant array of computer processing equipment is present onboard the sUAS. These components, which commonly run on 5V or 3.3V, are susceptible to voltage fluctuations induced by EMI. If severe enough, these voltage fluctuations can cause brownouts or unexpected shutdown of electronics.

5.4.1.6 Radiation Detection Components

A major advantage of SiPMs for use in sUASs is their insensitivity to magnetic fields. EMI however can still significantly impact the effective functioning of these devices, introducing noise and potentially amplifying dark counts, exacerbating cross-talk and afterpulsing, inducing bias voltage fluctuations affecting gain, and distorting output analog signal pulses.

In addition to the SiPMs themselves, the associated biasing and readout circuitry is susceptible to EMI. EMI can induce noise in PCB components, tracks, and ground planes, as well as induce current fluctuations in wires. As SiPM output signals are weak analog currents, they can become significantly compromised by EMI.

5.4.2 Sources of EMI

Constrasting the highly EMI-sensitive electronics components on the sUAS are significant EMI-producing components. Generally, EMI is produced by devices employing rapidly changing currents and switching circuits - namely the motors, ESCs, and RF transmitters (telemetry radio).

5.4.3 Mitigation

The constructed sUAS contains multiple RF emitters, both of broadband and narrow-band type. In the construction of a highly compact sUAS platform, mitigation of RF interference becomes increasingly important in order to reduce detector signal pulse noise, maintain robust wireless communication, and ensure proper operation of autopilot sensors and signal wire transmission accuracy. Common baseline guidance recommends a minimum 5cm distance between RF-sensitive electronics and RF emitters. In the constructed sUAS platform, this spacing is often not possible to achieve. Therefore, to meet the desired RF noise levels, a combination of strategic component placement and shielding is utilized.

A metric of onboard RF noise is available via the telemetry link’s “relative signal strength intensity (RSSI)” values, given in dBm, from which telemetry signal-to-noise ratio is derived. Additional discussion of PCB-level EMI mitigation is contained in Chapter 6.

5.4.3.1 Component Arrangement

As possibility of distancing of components to reduce interference is limited, the next approach, in order of effectiveness, relies on strategic arrangement of sUAS components to minimize interference. Elements of this approach include the central vertical stack layout, effectively distancing the onboard electronics as far from the motors as achievable. The GNSS’ compass is used in place of the flight controller’s built-in compass to improve signal. In addition, the high-power RFD900x radio is mounted below a frame arm to distance it from more sensitive electronics and analog signal wires, with its vertical antennas pointing downwards to improve signal strength (as in most flight scenarios the sUAS is positioned above the ground station radio modem).

5.4.3.2 Shielding

Following the exhaustion of preventative measures for EMI mitigation, shielding is utilized to protect sensitive components. Available EMI shielding tools applicable to sUASs include conductive copper tape, wire meshes, shielded cables, and braided EMI cable sleeving. In order to function as intended, shielding elements must be electrically grounded.

Aboard the constructed sUAS, grounded copper tape is applied to shield the central and peripheral SiPM biasing and readout boards. Grounded copper tape is additionally placed on the nanoPSD spectrometer face directly above the ESC. Coaxial RG-174u MCA cables are employed for all SiPM voltage and signal connections. A high-quality shielded micro USB - mini USB cable is used to protect the data link between the Raspberry Pi Zero 2 W onboard computer and the labZY nanoPSD spectrometer. Grounded EMI sheathes envelope all current-carrying wires between the battery, ESC, and motors. Where possible, wires connecting components are shortened and twisted together to reduce interference.

5.4.3.3 Antenna Placement and Orientation

As mentioned previously, initial telemetry communication was performed using 433 MHz Holybro Sik Telemetry Radio V3, but abandoned in favor of the 915 MHz RFDesign RFD900x modules due to SNR concerns. Significant differences between the two tested Holybro and RFDesign telemetry modules are maximum power outputs of 100mW and 1W, respectively, two antennas per RFD900x module, and the choice of a half-wave dipole antenna in the RFD900X versus the loading coil antenna employed by the Holybro V3. While coil antennas are employed by the onboard RFD900x module, the ground station module makes full use of two half-wave dipole antennas.

In addition to transmitter/receiver module and antenna selection, the placement and orientation of the antennas is integral for signal strength and effective range, as well as

minimization of interference with the flight controller and SiPM signals. In the case of a single receiver antenna, mounting orientation is generally upright in order to position the antennas' axial signal blind cones vertically. In the case of two receiver antennas, one is generally placed in an upright vertical position, and the second offset 90 degrees (horizontally) to eliminate blind cones. For optimal component arrangement within the available footprint, the RFD900x module is mounted under a rear sUAS motor (motor 3) with one antenna pointing downwards and the second pointing away from the sUAS center, and shielded with electrical tape to prevent potential shorts on exposed pins (Fig. 5.9). This placement maximizes the distance from the flight control and detection electronics located at the center of the sUAS. Mounting below motor 3, the rear-left motor, positions the module to maintain a clear line of sight between the onboard radio antennas and the ground station as the sUAS faces away from its launch location.



Figure 5.9: Photo of assembled sUAS with RFD900x telemetry module in the foreground

Chapter 6

Detection Circuitry and Data Communication

The following chapter describes the design, integration and programming of all components necessary to enable radiation mapping by the sUAS. Included is a detailed discussion of circuitry for biasing and readout of the four onboard structural scintillator arms, processing of SiPM signal pulses into PSD spectra by the onboard spectrometer, the digital integration of radiation and positional data obtained from multiple onboard components, and the live communication of detector data from the sUAS to the ground station

Biasing and readout of SiPMs onboard the sUAS poses several challenges. The four individual structural scintillator frame arms' SiPMs are biased at a fixed voltage of 29.5V. Signals from the four arms are read out into a central single-channel labZY/Yantel nanoPSD PSD spectrometer. SiPM biasing must be provided by a steady, uniform, low-noise power supply of unconventional and relatively high voltage for compact electronics but low current. Readout must effectively collect analog signals susceptible to both internal noise from electronics and non-firing SiPMs, as well as EMI. Finally, signal processing must effectively perform PSD and transmit results in a communicable format to the ground station.

6.1 Biasing

Biasing of the SiPMs involves the supply of a stable, low-noise voltage of 29.5V to apply a reverse bias with desired overvoltage maximizing SiPM gain within its safe operating voltage range. As 29.5V is an uncommon value, it can be supplied either by reducing a higher-voltage source to the desired value (step-down), or by converting a lower voltage to the desired value (step-up). Both methods are discussed in the following section.

6.1.1 Step-Down Approach

The step-down SiPM biasing approach utilizes an ultralow dropout (ULLDO) DC-DC voltage converter circuit to achieve the target 29.5V. The advantages of this approach include the avoidance of switching regulator noise as well as the use of a dedicated SiPM biasing battery isolated from the current and voltage fluctuations present in the primary sUAS battery. Power is provided by either three 12-Volt Duracell MN21 batteries in series, with a combined weight of 50 grams, or 8 LiPo 3.7V nominal 100mAH rechargeable batteries connected in series. A dedicated battery for SiPM biasing is required, as the primary sUAS battery nominal voltage is insufficient at 22.2V nominal.

The core circuit component regulating the $>30V$ input voltage is the ONsemi/Texas Instruments LM2931 ULLDO. The biasing circuit was designed using KiCad, in accordance with the component's datasheet. To ensure steady output voltage for SiPM reverse biasing, the circuit includes a large battery decoupling capacitor and a low-pass filter (Fig. 6.1). Output voltage is adjustable using feedback resistors R1 and R2, carefully selected to provide the correct output voltage. PCB track lengths were minimized wherever possible, with components arranged in a star grounding pattern.

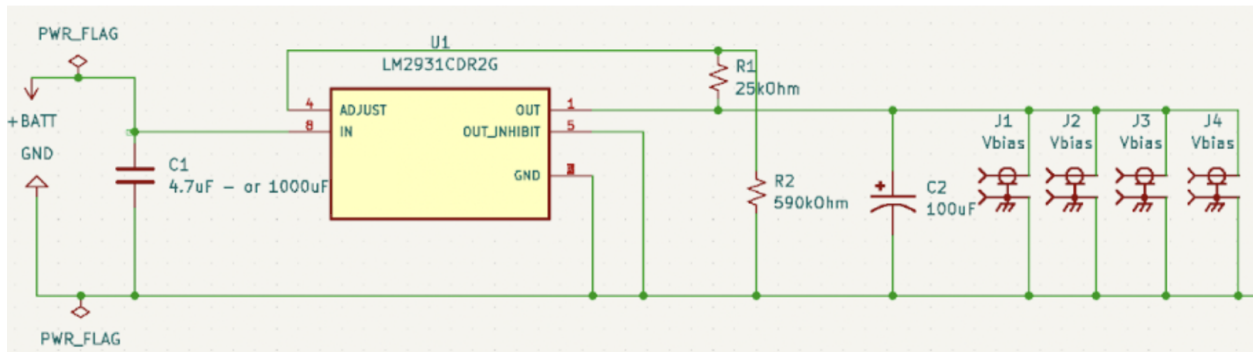


Figure 6.1: ULLDO SiPM biasing circuit diagram, providing four Vbias outputs

PCB manufacturing services of the designed layout were provided by Bay Area Circuits. Board components were hand-soldered. A fabricated bias supply used for laboratory bench testing is depicted in Fig. 6.2, containing three 12V batteries providing input voltage and a switch for toggling Vbias output.

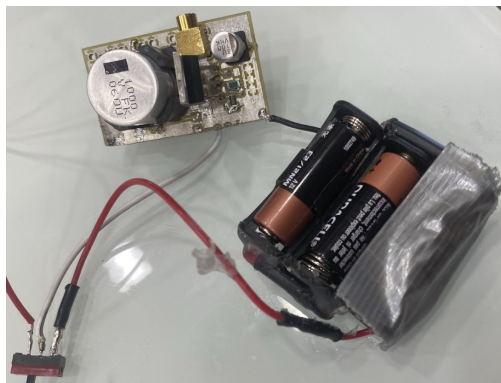


Figure 6.2: Fabricated ULLDO 29.5V output SiPM bias supply used in laboratory bench-testing

In laboratory testing, a ^{137}Cs spectrum obtained using a 1" cylindrical PSD plastic scintillator coupled to a Sensl J-Series 6mm 2x2 SiPM array, reverse-biased using the fabricated ULLDO circuit, exhibited no measurable difference from a spectrum obtained using the same detector configuration and measurement parameters powered by a Tenma 72-6905 benchtop power supply (Fig. 6.3).

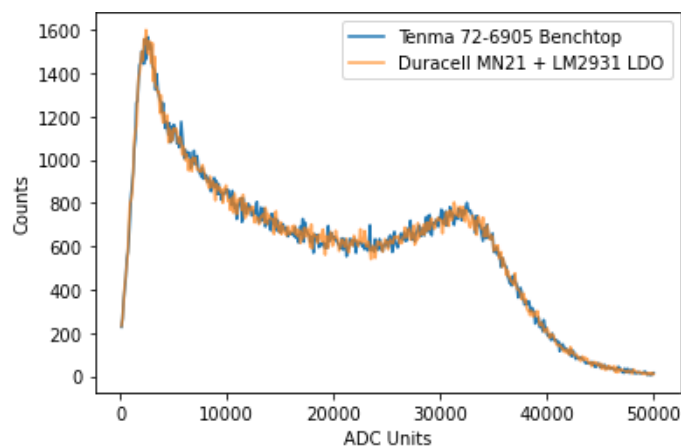


Figure 6.3: Plot comparison of collected ^{137}Cs energy spectra by a SiPM-coupled PSD plastic scintillator, biased using the fabricated ULLDO and a benchtop power supply

Despite the board's biasing effectiveness, difficulties were experienced with the step-down approach. The primary difficulty was due to the relatively high start-up current demanded by the ULLDO (26mA), which could not be adequately supplied by the lightweight, low-capacity batteries. The simplest method to alleviate this issue involves providing initial

start-up power using a benchtop power supply, and using a switch to transfer the power source to the battery once the circuit output voltage stabilizes, on the order of less than one second. The start-up behavior is captured by an oscilloscope in Fig. 6.4.

In addition to the high start-up current, the input voltage supply batteries were required to be partially drained prior to operation in order to meet the high-voltage ULLDO cutoff of 32V, from a maximum of 37.8V for the three MN21 batteries in series (12.6V per cell) or 33.6V for the LiPo β pack.

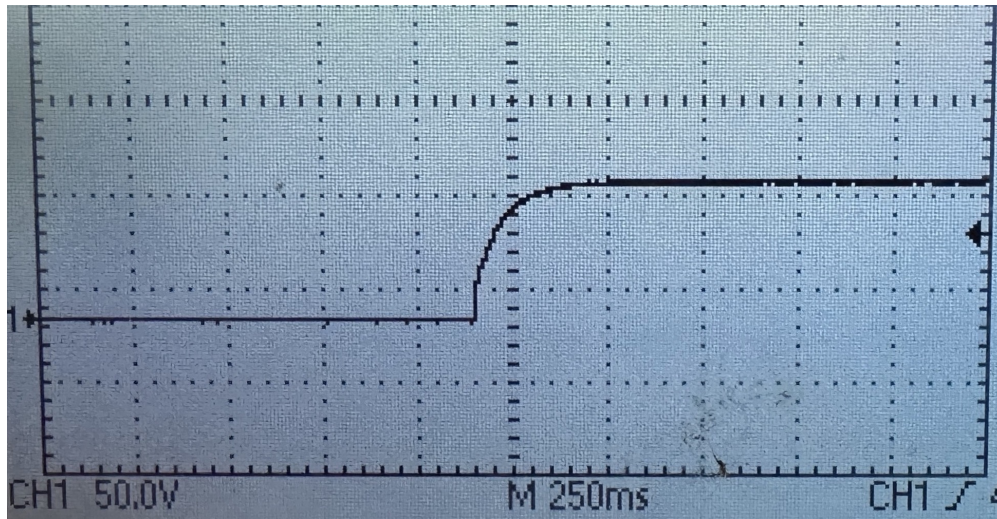


Figure 6.4: Start-up output voltage curve for ULLDO powered by Tenma 72-6905 benchtop power supply (voltage not to scale).

6.1.2 Step-Up Approach

A step-up approach was pursued following the conditional success achieved using the step-down circuit. The advantages of this approach include a low input voltage requirement allowing common electronics voltage sources to be used, such as 5V USB, thereby eliminating the need for a separate SiPM biasing battery and reducing the sUAS components' weight and footprint. A biasing circuit was designed in Autodesk Fusion 360, featuring a Maxim MAX5026 500kHz buck-boost DC-DC voltage converter, a decoupling capacitor, and two low-pass filters, providing an output voltage of 29.4V through careful selection of feedback resistors R1 and R2 (Fig. 6.5).

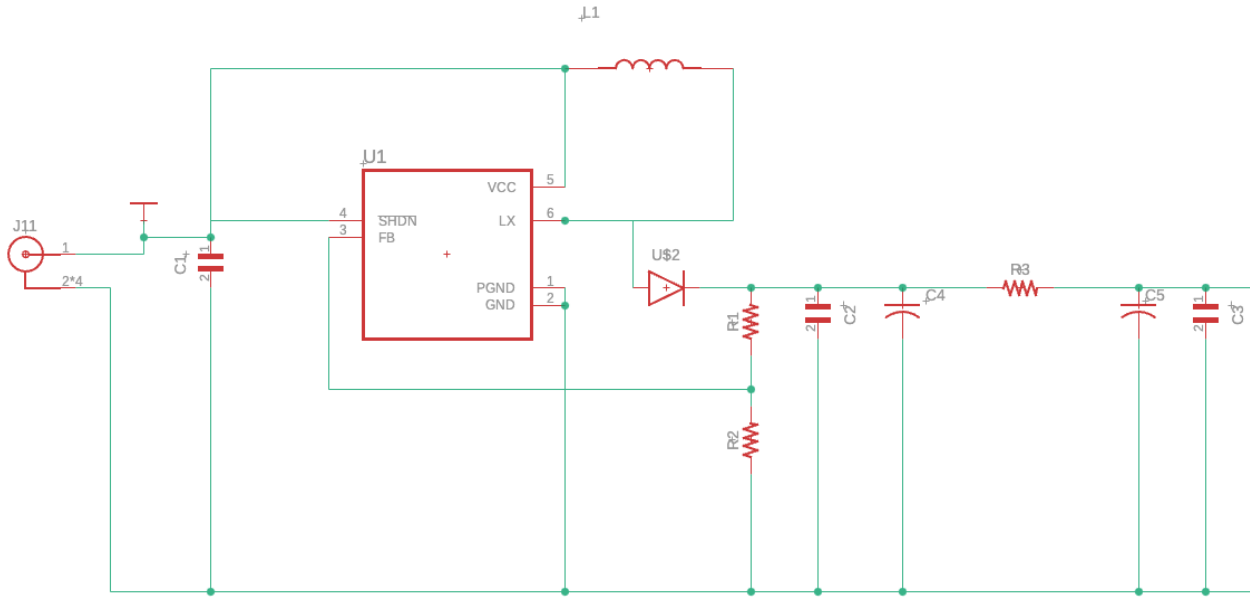


Figure 6.5: Circuit diagram of 5V-29.5V step-up SiPM bias voltage source, utilizing a MAX5026 buck/boost DC-DC converter

During laboratory testing, no substantial difference existed between ^{137}Cs energy spectra measured by a SiPM-coupled PSD plastic scintillator biased using the step-up switching regulator circuit and a benchtop power supply, as with the previous ULLDO circuit. 500kHz switching noise was observed with an amplitude of 1-2mV, and was effectively mitigated by the digitizer minimum voltage threshold.

6.2 Readout

The second function of the onboard central SiPM biasing and readout board is the collection and routing of analog current pulses generated by SiPMs to the single-channel spectrometer for pulse processing and PSD analysis. Techniques for multiple SiPM array readout are an active field of study with numerous established methods, providing different characteristics in regards to timing performance, energy resolution, pixelization, and SNR. For the application of four SiPM arrays multiplexed into a single channel readout, as is the case in the constructed sUAS, the pulse characteristics of highest importance are pulse shape integrity and minimization of noise. Pulse shape is impacted by SiPM multiplexing due to a change in circuit capacitance, while signal-to-noise ratio (SNR) is impacted in multiplexing applications due to the potential noise contribution from multiple SiPMs to collected signal pulses from individual SiPMs.

6.2.1 Peripheral SiPM Boards

Accompanying the central biasing and readout board are secondary PCBs, referred to as the peripheral SiPM boards, that are coupled directly to each SiPM to supply bias voltage to the four SiPM cathodes and collect output signals from the four SiPM anodes of each scintillator's coupled SiPM array. Input voltage is supplied from the central bias and readout board's common 29.5V cathode to an MCX socket on each peripheral board. Each board contains a passive low-pass filter composed of a 100Ω resistor in series followed by a $4.7\mu\text{F}$ capacitor in parallel to mitigate input voltage distortions caused by interference in the RG-174U coaxial cable connecting the central bias board to the peripheral board. The SiPM arrays are connected to the peripheral boards using 8-pin dual row DIN sockets soldered onto the PCBs. This prevents the direct soldering of SiPM pins to a PCB, which cannot be performed by hand and must be done in the absence of humidity, in order to prevent damage to the SiPM from the expansion/vaporization of water molecules within [36].

Common bias voltage is routed to the four cathode pins of the DIN socket of each of the four quad-SiPM arrays. The four anodes of each quad-SiPM array are connected in series at the DIN socket, yielding a single signal MCX socket output for each peripheral board.

6.2.2 Signal Series Summation

The simplest multiplexing method available to implement is summation of SiPM signals in series, and as such is the initial readout method applied for the four sUAS arms. In this method, the individual signal lines are connected in series to a single output.

The four peripheral board signal outputs are connected using male-male MCX RG-174U cables to the central bias-readout board's input signal MCX sockets. The board's four signal inputs are connected in series to yield a single MCX socket signal output. A 50Ω resistor is placed in parallel to the signal output, in order match the spectrometer and RG-174U coaxial cable impedances. The absence of this resistor results in characteristic pulse distortions due to signal reflections within the cable.

6.2.3 Signal-Driven Multiplexing

A second established method for readout of multiple SiPMs to a common output is signal-driven multiplexing. This readout technique provides an improved SNR when compared to simple signal series summation by rejecting the noise contributions of non-firing SiPMs [37]. The basic operation involves a common readout to which each multiplexed SiPM is connected by a pair of Schottky diodes. When a signal is generated by an SiPM, the positive signal pulse voltage forward-biases the Schottky diode "downstream" to allow the signal to continue along the common readout, while simultaneously reverse-biasing the downstream Schottky diodes of the remaining non-firing SiPMs. The second Schottky diode serves to create a symmetry to provide a constant sum of current at the common output [38].

For SDM to be effective when implemented as a readout method for weak analog signals (such as from SiPMs coupled to high aspect-ratio scintillators aboard the sUAS), the forward voltage drop of the employed Schottky diodes must be either as low as possible, or compensated for by biasing the diode. The voltage drop of a typical Schottky diode is between 150 mV – 450 mV, while voltages of collected SiPM signals may be as low as 10 mV. With this consideration, a passive approach may be employed utilizing zero-bias Schottky diodes, commercially available with forward voltage drops as low as 8mV [39]. Alternatively, the traditional approach of biasing conventional Schottky diodes using a positive voltage slightly below the voltage drop threshold may also be employed.

Fig 6.6 depicts a schematic of a SDM readout design for the constructed sUAS. Similarly to the series summation readout configuration, each sUAS arm SiPM is mounted on a peripheral board containing a low-pass filter, a DIN socket, 50 Ω terminator, and MCX socket connections for biasing and readout. The peripheral PCBs are identical to those used in series summation, with the primary differences between readout methods being the collected peripheral boards' signal arrangement and routing in the central biasing and readout board.

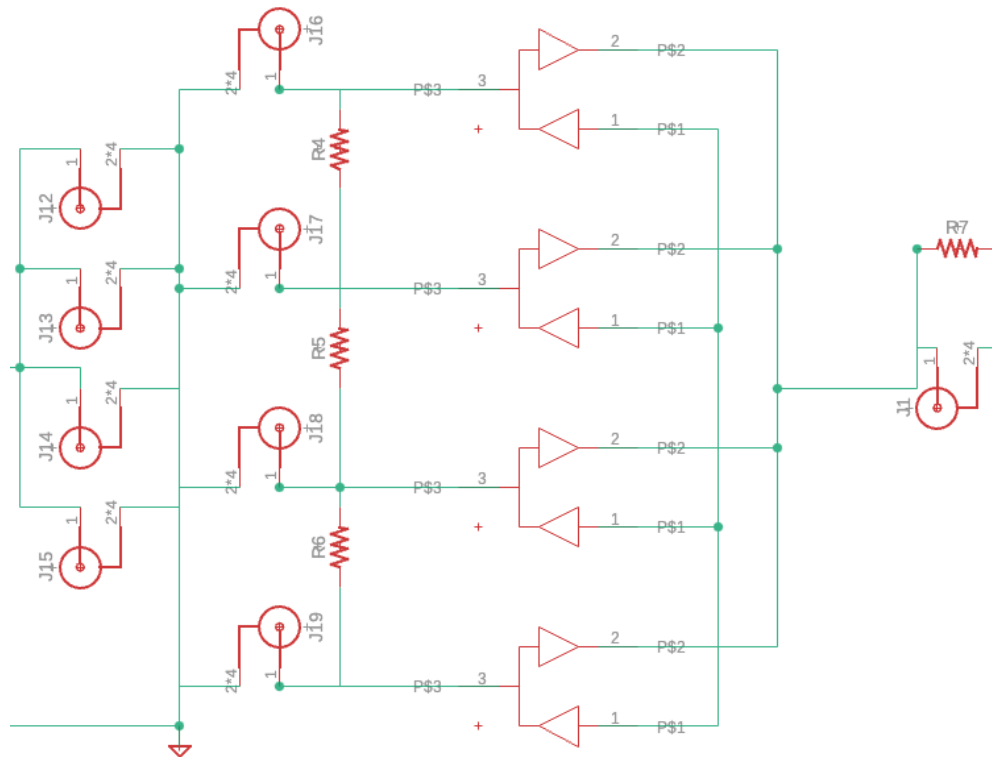


Figure 6.6: Circuit diagram of signal-driven multiplexing implemented for readout of the four structural-scintillator sUAS frame arm SiPMs

6.3 Signal Processing

Processing of the analog SiPM signals aggregated by the readout board into a single output channel is performed by the onboard labZY nanoPSD spectrometer. The nanoPSD accomplishes PSD using the time-invariant pulse shaping (TIPS) technique [40], and produces four histograms of the processed signals corresponding to: TIPS score, combined γ -ray and neutron energy spectrum, γ -ray energy spectrum, and neutron energy spectrum. The output spectra are viewable using the complementary labZY-PSD software (Fig. 6.7). Regions of interest (ROIs) can be marked on the TIPS score spectrum to establish TIPS regions corresponding to γ -rays and neutrons to classify pulses to their appropriate energy spectra. ROIs can be marked on the combined γ -ray and neutron energy spectrum to establish energy bounds for pulses included in the TIPS spectrum, such as a minimum energy threshold for performing PSD. The nanoPSD applies a noise-dependent variable energy threshold performed by a proprietary algorithm by default, which can be manually set to desired ADC values. In addition, numerous parameters settings for pulse shaping and processing are available for modification in order to optimize generated spectra dependent on detector characteristics and measurement conditions.

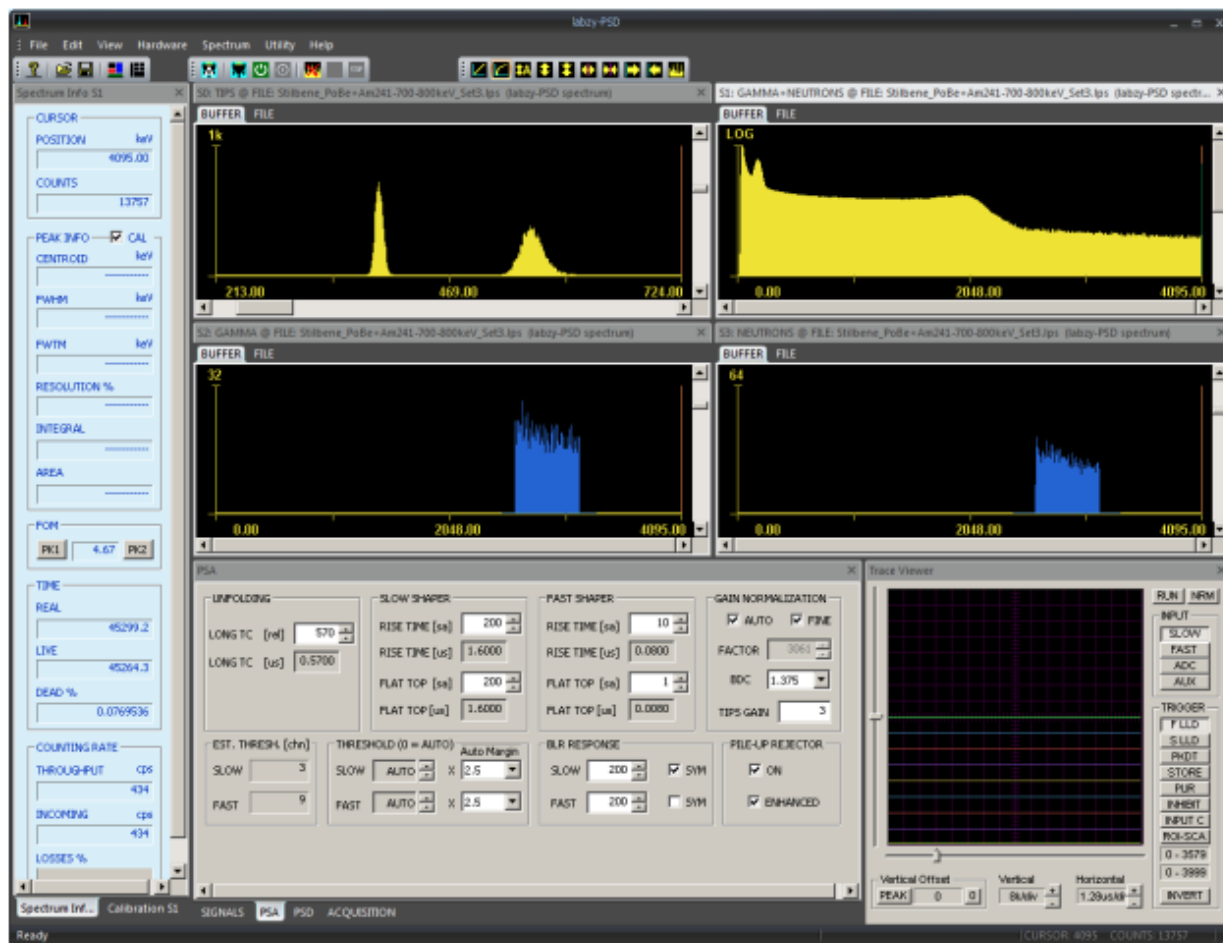


Figure 6.7: Example screenshot of labZY analysis software

The nanoPSD modules used for the constructed sUAS were provided by Dr. Valentin Jordanov, set for a positive input signal compatible with the employed SiPMs.

6.3.1 nanoPSD Parameters

The acquisition and pulse shaping parameters of the nanoPSD significantly affect TIPS spectra generation and obtained PSD FOM values. Save for the preamplifier gain, which must be set physically via a rotating knob to a value 0-7, all other parameters are set through software, with the provided Windows application writing the desired settings to the spectrometer's FPGA registers. Although specific parameter values vary depending on the response of the measuring scintillator, the labZY-PSD Software User Manual Versions 2.50-2.99 Revision 1a provides general guidelines for setting parameters [41].

For the constructed sUAS, pulse shape analysis (PSA) parameters were set according to Table 6.1. Physical preamplifier gain was set to its maximum setting (7). Parameters were optimized for PSD FOM at relatively low count rates of up to several thousand counts per second. The parameters of the signals tab and acquisition tab menus were left as the default values. To note, the AUTO UPDATE setting of the acquisition tab must be enabled in order for live streaming of measured spectra to function.

Table 6.1: labZY nanoPSD spectrometer PSA Tab Parameters calibrated for constructed SUAS

Category	Parameter	Value
Preamplifier (Physical)	Gain	7
Unfolding	Long TC	600
Slow Shaper	Rise Time	25
	Flat Top	225
Fast Shaper	Rise Time	12
	Flat Top	1
Gain Normalization	Auto	Yes
	Fine	Yes
	BDC	1.375
	TIPS Gain	10
Threshold	Auto Margin (Slow)	1
	Auto Margin (Fast)	1
BLR Response	Slow	200
	Fast	200
	SYM (Slow)	Yes
	SYM (Fast)	Yes
Pileup Rejector	On	Yes
	Enhanced	Yes

6.4 Electronics Wiring

The organizational flow of radiation detection information between the components of the sUAS is depicted by the flow chart shown in Fig. 6.8. Power is provided by the battery to the flight controller's carrier board using the Pixhawk power module connected in parallel to the 4-in-1 ESC's power connection. The associated detection and communication electronics including the GNSS, telemetry radio, companion computer, and PSD spectrometer are powered the carrier board through by various connections.

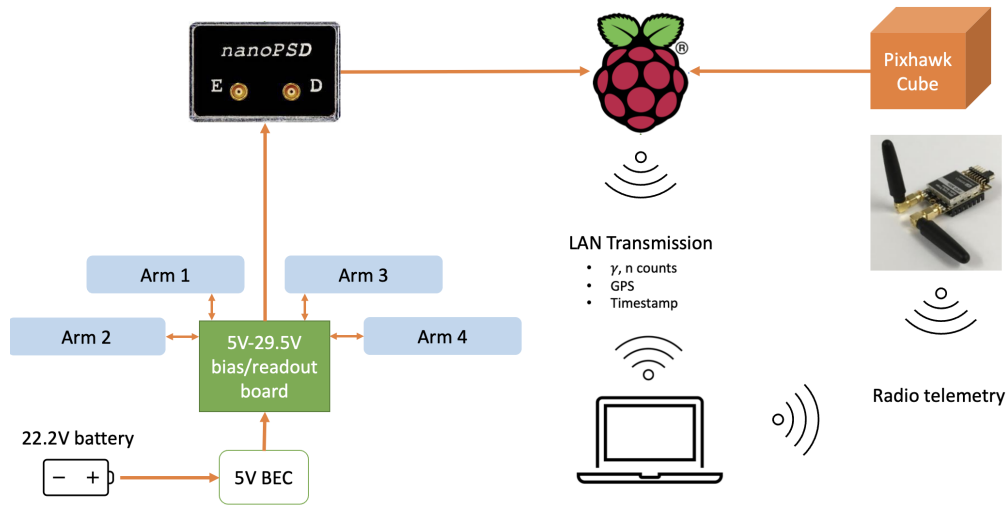


Figure 6.8: Organizational diagram of inter-component communication for the constructed sUAS

Physical connection of the GNSS and telemetry radio to the carrier board is straightforward, using the manufacturer-provided cabling. Custom wiring was prepared for the connection between the companion computer and the carrier board, by soldering a modified Telem2 cable to the Power, GND, TX, and RX GPIO pins of the Raspberry Pi Zero 2 W companion computer (Fig. 6.9). The Telem2 cable wires were twisted to reduce EMI susceptibility. Although not directly connected to a port on the carrier board, power is supplied to the spectrometer via the micro USB data port of the companion computer, which shares a power connection with the Telem2 power supply. A shielded mini USB - micro USB cable is utilized for the physical connection.

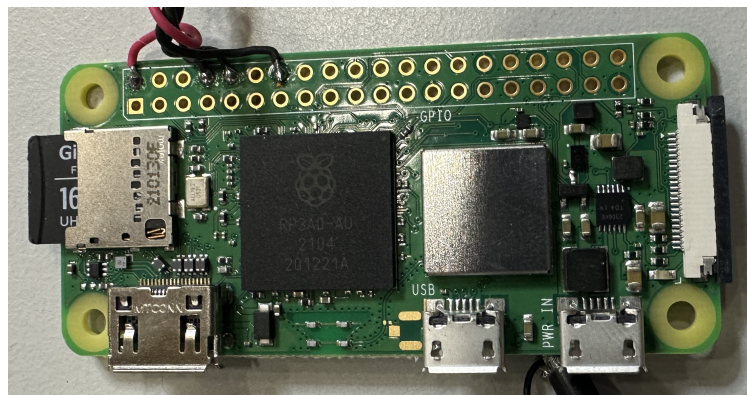


Figure 6.9: Photo of Raspberry Pi Zero 2 W soldered TELEM cable GPIO connections

Careful consideration was made to ensure the power draw by the onboard electronics does not exceed the Pixhawk carrier board's rated maximum current output of 2.5 A; 1.5 A of which is accessible at the Telem1 port, and 1 A accessible by the remaining peripherals' ports. Table 6.2 lists the rated average and maximum power draw of the onboard electronics powered by the carrier board. Although the typical steady-state power draw of the components is well below the 2.5A limit, the simultaneous current draw of all the components upon start-up can potentially exceed the available power. This was observed experimentally in the constructed sUAS as continuous rebooting of the companion computer and shutoff of the spectrometer shortly after powering on. These symptoms can be easily alleviated by powering on the spectrometer shortly after the other components - a 60 second delay is sufficient.

Table 6.2: Table of rated power draws of constructed sUAS peripherals powered by Pixhawk Cube carrier board

Component	Port	Avg. Power Draw (mA)
Here3 GNSS	CAN1	150
RFDesign RFD900x	Telem1	1000
Raspberry Pi Zero 2 W	Telem2	120 (580 peak)
labZY nanoPSD	Telem2	180

Power to the SiPM biasing and readout board is provided by the 5V battery elimination circuit (BEC) output of the 4-in-1 ESC, connected via a semi-flexible coaxial cable. All bias voltage and signal readout connections between the central board, peripheral boards, and spectrometer utilize coaxial RG-174U MCX cables. Coaxial cables were cut to size and hand-crimped to minimize cable lengths and reduce EMI susceptibility.

6.5 Data Communication

The established physical infrastructure allows for multi-way communication between the electronics onboard. Key data links include the spectrometer - companion computer interface, the flight controller - companion computer interface, and the companion computer - ground control station (GCS) interface.

6.5.1 Raspberry Pi - nanoPSD Communication

Two-way communication between the spectrometer and the onboard companion computer permits the control of measurement data acquisition, setting of parameters, and transmission of generated output spectra from the spectrometer to the companion computer. In a conventional (e.g. laboratory) measurement scenario with the spectrometer connected via USB to a computer, Windows software is provided by labZY to perform all necessary functions in

a graphical user interface (GUI) allowing the operator to view and analyze output spectra in real-time (Fig. 6.7).

However, in order to process spectra compiled by the nanoPSD onboard the sUAS, two-way communication and data transfer between the nanoPSD and the onboard Linux-based Raspberry Pi Zero 2 W computer must be accomplished. Despite the operating system incompatibility, this computer was chosen due to its low form factor and weight, minimal power consumption, cost, and communication compatibility with the Pixhawk Arducopter platform.

6.5.1.1 Establishing Linux Communication

An initial attempt was made to run the included labZY software on the Raspberry Pi using Wine, unsuccessfully. Therefore a custom software package needed to be written. USB driver compatibility was assessed between the labZY nanoPSD and the Raspberry Pi OS (Raspbian) Linux-based operating system on the Raspberry Pi.

Executing the `lsusb` command in Terminal with the nanoPSD connected to the Raspberry Pi via the micro USB port revealed the nanoPSD communicates using an FTDI chip (Fig. 6.10). As Linux devices by default contain the virtual COM port (VCP) drivers required for communication with FTDI chips, writing a custom device driver was not necessary.

```
pi@raspberrypi:~ $ lsusb
Bus 001 Device 002: ID 0403:6015 Future Technology Devices International, Ltd Bridge(I2C/SPI/UART/FIFO)
Bus 001 Device 001: ID 1d6b:0002 Linux Foundation 2.0 root hub
pi@raspberrypi:~ $ █
```

Figure 6.10: Terminal output of `lsusb` command for nanoPSD connected to micro USB

The next task is the decoding of the communication structure of the transmitted packets. To accomplish this, Wireshark and USBPcap were installed on a Windows laptop. Wireshark is an open-source packet analyzer, and USBPcap enables “USB sniffing”, or monitoring, of USB port communication packets. With the nanoPSD connected to the Windows laptop running the labZY software, Wireshark in conjunction with USBPcap were used to intercept and record packets transmitted across the live USB port. Measurement acquisition of a sample 1” cylindrical SiPM-coupled PSD plastic detector biased at 27V was started and ended approximately 30 seconds later using the Windows software, with USB packets recorded over the acquisition period.

The recorded packets were labeled as TX (transmitted from laptop) or RX (received from spectrometer). For the captured TX packets, message payload sizes were either 11 bytes, or 241 bytes. RX message payload sizes were more varied, being either 9 bytes, 225 bytes, 279 bytes, 289 bytes, or 3968 bytes.

Closer inspection of the frequency of transmission of the different message sizes revealed the TX 241-byte and RX 9 byte messages were sent only twice, grouped together at the approximate start and stop acquisition times. These were deduced to contain the start

acquisition and stop acquisition TX messages, accompanied by an 9-byte RX confirmation from the spectrometer.

In between these transmitted packet pairs, TX messages of size 11 were sent, followed shortly by either one message of size 279 bytes, or three RX messages of sizes 3968 bytes, 3968 bytes, and either 225 or 289 bytes, in the specified chronological order. The three RX packet messages had a total cumulative size of 8161 or 8225 bytes. Comparing the maximum number of spectrum channels available, 4096, the captured 8225-byte RX payloads are 33 bytes larger than twice the number of available spectrum channels (8192). With this finding, the 11-byte TX message were suspected to represent a request from the Windows computer to stream a spectrum, and the 8225-byte RX message providing a 4096-channel spectrum with each channel represented by 2 bytes, together with 33 bytes of metadata (potentially 32 bytes of metadata and a 1-byte message checksum).

Initial analysis of the received messages was performed for the RX 9-byte message payload. The payload of a sample recorded message was:

Table 6.3: Structure of intercepted 9-byte RX message payload

Binary	Decimal	Hex
01101110	110	6E
00000000	0	0
00001001	9	9
00000000	0	0
00001100	12	C
10000000	128	80
11000000	192	C0
00000000	0	0
01000000	64	40

The acquired message payload was cross-referenced with the labZY nanoMCA documentation, revealing the intercepted message structure is consistent with the labZY Device Response to Host Write Command described in the labZY Open Communication Manual, labZY Firmware, Versions 30.19, 20, despite the nanoPSD not being included in the Applicable Devices list (Fig. 6.11) [42].

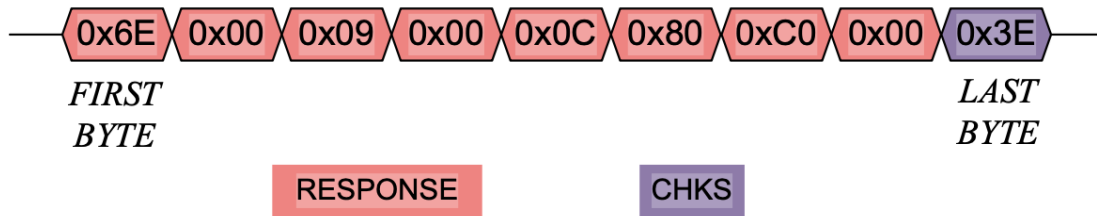


Figure 6.11: labZY Device Response to Host Write Command structure [42]

6.5.1.2 Command Structure

Using the intercepted USB packets and the labZY documentation, the command structure of functions necessary for operation onboard the sUAS was reverse-engineered and interpreted as information transmitted to and from the labZY device in 16-bit (2-byte) words or 2-word long words, in little-endian order.

The captured 241-byte TX message payloads sent to initialize and end acquisition were analyzed in a similar manner to the 9-byte RX packet previously, and observed to follow the structure described in the FPGA Registers, Standard labZY FPGA Designs, Revision 7.1 labManual (despite the nanoPSD not being listed as an Applicable Device in the document) [43]. Device acquisition status is set by a WRITE command, containing 8 header bytes followed by data of 116 2-byte (16-bit) registers in little-endian format to write to the device FPGA, starting from register 12, followed by one check-sum bit.

For starting and stopping acquisition, the applicable register is Register 16: Control and Status (CTRS). Spectrum acquisition is enabled by writing the value of bit 0 to 1, and disabled by setting it to 0. To clear an existing spectrum in the device buffer, the value of bits 5-4 should be set to 2. In this way, acquisition is controlled by writing 116 of the 127 registers to the nanoPSD, with a modified register 16. Successful writing is confirmed digitally by the receipt of the 9-byte RX labZY Device Response to Host Write Command, or physically by observing the behavior of the blue LED on the device: blinking during acquisition, and solid when stopped.

In between the acquisition start and stop commands, a READ command is sent containing an 11-byte message payload every second. The Host Read Command contains 10 header bytes followed by a checksum byte. The bytes structure is described in the Open Communication labManual, and contains the command code (100) in the first byte, the message payload byte length (11) in the second byte, the “FPGA address of the first data word to be read”, and “the number of FPGA bytes to be read”.

FPGA addresses 0x8000 to 0x807F are reserved for registers 0-127, and FPGA addresses 0x0000 to 0x7FFF (32768 bytes) reserved for spectral data. Each spectrum channel is represented by a long word, indicating 16,384 possible channels may be read. Through analysis of intercepted packets, the 16,384 channels were inferred to comprise four separate spectra of 4096 channels each. For the nanoPSD, the four spectra correspond to the TIPS, combined

γ -ray and neutron energy, γ -ray energy, and neutron energy. Verification of successful Read command transmission is performed by the receipt of the requested FPGA address data: either 279 bytes representing 127*2 registers, 24 header bytes, and 1 checksum byte, or 8225 bytes representing 4096 * 2 spectrum channels, 32 header bytes, and 1 checksum byte.

For each message, calculation of the checksum is performed as described by the labZY Open Communication labMANUAL.

To verify the correct packet structure, the captured packets were re-transmitted from the Windows machine to the nanoPSD by opening a serial socket on the Raspberry Pi. The received spectrum packets were observed to cycle between the four available spectra (TIPS, gamma+neutron, gamma, and neutron spectra), as well as the registers.

6.5.1.3 Acquisition Control

Communication with the nanoPSD from the Raspberry Pi Zero 2 W in the absence of the provided Windows control software can be performed by opening a serial port and sending one of two basic command types: read and write. Read commands are short packets transmitted to request a data stream, such as a specific spectrum or the Field Programmable Gate Array (FPGA) registers. Write commands are packets transmitted to set FPGA parameters, such as the trapezoidal shaper parameters and acquisition commands. For the purposes of simplifying the in-flight data acquisition software, the pulse processing parameters are set prior to flight using the Windows software, with measurement acquisition control commands utilized during flight.

To perform a measurement, the Raspberry Pi communicates with the nanoPSD using a Python script which opens a serial port for sending commands and requesting data. The applicable serial port can be revealed using the *dmesg* command (Fig. 6.12). Port location was set to */dev/ttyUSB0*, and baud rate to 921600. First, a read command is sent to request the current device registers using `port.write()`, followed by `port.read(279)` to record the following 279-byte packet received from the nanoPSD. The received registers are saved to a .txt file as a record of the spectrometer's measurement parameters. Next, a write command is sent using `port.write()` to start the measurement by splicing the previously obtained registers and altering register 16 to start data acquisition. A read command for 9 bytes is then sent to confirm successful transmission.

```

pi@raspberrypi:~$ sudo dmesg | grep tty*
[ 0.000000] Kernel command line: coherent_pool=1M 8250.nr_uarts=1 snd_bcm2835.enable_compat_alsa=0
snd_bcm2835.enable_hdmi=1 video=Composite-1:720x480@60i smsc95xx.macaddr=B8:27:EB:94:85:13 vc_mem.me
m_base=0x1ec00000 vc_mem.mem_size=0x20000000 console=tty1 root=PARTUUID=89428214-02 rootfstype=ext4
fsck.repair=yes rootwait modules-load=dwc2,g_ether quiet splash plymouth.ignore-serial-consoles
[ 0.000474] printk: console [tty1] enabled
[ 0.004658] Setting up static identity map for 0x100000 - 0x10003c
[ 0.090125] raspberrypi-firmware soc:firmware: Attached to firmware from 2022-08-26T14:04:36, vari
ant start
[ 0.158659] pps_core: Software ver. 5.3.6 - Copyright 2005-2007 Rodolfo Giometti <giometti@linux.i
t>
[ 2.707684] Setting default values for core params
[ 2.707716] Finished setting default values for core params
[ 2.938381] 3f201000.serial: ttyAMA0 at MMIO 0x3f201000 (irq = 114, base_baud = 0) is a PL011 rev2
[ 6.957229] systemd[1]: Created slice system-getty.slice.
[ 242.556072] usb 1-1: FTDI USB Serial Device converter now attached to ttyUSB0
pi@raspberrypi:~$

```

Figure 6.12: Terminal output of `sudo dmesg — grep tty*` command

To request the current loaded registers, a 22-byte message is transmitted as:

```
b"\x64\x00\x0b\x00\x01\x80\x00\xfe\x00\xd5"
```

The received message of length 279 bytes contains (in order): the READ command response byte, 2 microdata bytes, 127 2-byte (16-bit) registers in little-endian format from the device FPGA, and one check-sum bit.

6.5.1.4 Spectrum Transmission

Once acquisition has begun, a read command is sent using `port.write()` to the nanoPSD once per second requesting streaming of the TIPS spectrum, followed by `port.read(8225)` to record the following 8225 bytes received. The first 32 bytes include an 8 byte header line and 24 bytes of microdata, followed by an 8192 channel spectrum and a final checksum byte.

Each received spectrum is saved to a .txt file together with GPS coordinates acquired from the flight controller, and transmitted to the ground station computer.

6.5.1.5 Linux Implementation

To emulate the functionalities of the labZY Windows software on the onboard Linux companion computer, a python program was written to streamline communication with the nanoPSD through the serial port. The program is composed of a main file (`main.py`), a function for reading the device registers (`read_registers.py`), a set of functions to start acquisition (`start_measurement.py`), a function to read the TIPS spectrum (`read_spectrum_tips.py`), and a function to stop acquisition (`stop_measurement.py`). The program is run by executing the `main.py` function in Terminal, providing the desired measurement duration in seconds, and specifying whether to clear the existing spectrum at the start of acquisition using a boolean flag. For example, `main.py 60 1` executes a 60 second measurement with a clear spectrum.

When `main.py` is executed, serial port 0 is opened at `/dev/ttyUSB0`. The program then reads the registers onboard and writes a command to the open port consisting of the previously received registers 12-127 with register 16 modified accordingly with a newly-calculated checksum, and confirms successful transmission by listening for a 9-byte RX message. Upon receiving confirmation of acquisition start from the nanoPSD, the program then records the system time and repeats a 1-second loop for the user-provided measurement duration in which a read command is sent of structure:

```
\x64\x00\x0b\x00\x08\x20\x40\x00\x08\x20\x04
```

Bytes 8-9 of the command indicate an instruction to read 8200 bytes, and bytes 4-7 indicate data reading to start at FPGA hex address 2008 (decimal 8200) with automatic incrementing as words are read.

The program then listens for three RX messages of lengths 3968, 3968, and 289 bytes and concatenates them into one bytearray. A plain-text file with an incremented name is created in a directory named as the system date. The first 32 bytes of the array are converted to strings and written as four header and microdata rows in the text file, followed by the 8192 bytes containing 4096 spectrum channels as words converted to strings.

At the end of the measurement duration, acquisition is stopped by writing registers 12-127 with register 16 modified accordingly and a newly-calculated checksum. The program listens for a 9-byte RX message from the port, with its receipt confirming the end of the measurement.

6.5.2 Raspberry Pi - Pixhawk Cube Communication

Through the Raspberry Pi Zero 2 W's connection to the Telem2 port on the Pixhawk Cube carrier board, communication between the onboard companion computer and the flight controller is established.

6.5.2.1 Establishing USB Interface

The custom Telem2 cable is soldered to the Raspberry Pi Zero 2 W's GPIO pin 2 providing 5V power, pin 6 for grounding, and pins 14 (TX) and 15 (RX) for data communication. To configure the Raspberry Pi to operate GPIO pins 14 and 15 as a serial (USB) port, the command `sudo raspi-config` was written in Terminal to bring up the configuration menu. Within Interfacing Options, Serial was selected, and when prompted "Would you like a login shell to be accessible over serial?" No was selected, and Yes to "Would you like the serial port hardware to be enabled?". The Raspberry Pi was rebooted, and the serial port connection tested by running the command in terminal `ls /dev/ | grep ser` (Fig. 6.13).

```

pi@raspberrypi:~/nanoPSD_programming $ ls /dev | grep ser
serial0
serial1
pi@raspberrypi:~/nanoPSD_programming $ ls -l /dev/serial0
lrwxrwxrwx 1 root root 5 Sep 14 15:17 /dev/serial0 -> ttyS0
pi@raspberrypi:~/nanoPSD_programming $ ls -l /dev/serial1
lrwxrwxrwx 1 root root 7 Sep 14 15:17 /dev/serial1 -> ttyAMA0

```

Figure 6.13: Raspberry Pi Zero 2 W Terminal output displaying enabled GPIO serial port 1

Of the ports displayed in Fig. 6.13, Serial0 corresponds to the microUSB port, and serial1 to the GPIO port. As depicted in Fig. 6.13, serial1 is mapped to ttyAMA0, by default mapped to the computer's Bluetooth interface. To enable the operation of ttyAMA0 as the serial port, Bluetooth was turned off using the command `sudo vi /boot/config.txt` to access the computer's boot config file, to which `dtoverlay=disable-bt` was added. The computer was then rebooted.

6.5.2.2 MavLink 2 Protocol

The default and most up-to-date communication protocol used by serial connections to the Pixhawk Cube flight controller running Ardupilot firmware is MAVLink 2. Open-source MAVLink 2 communication libraries are available for Linux, and were installed by the following commands:

```

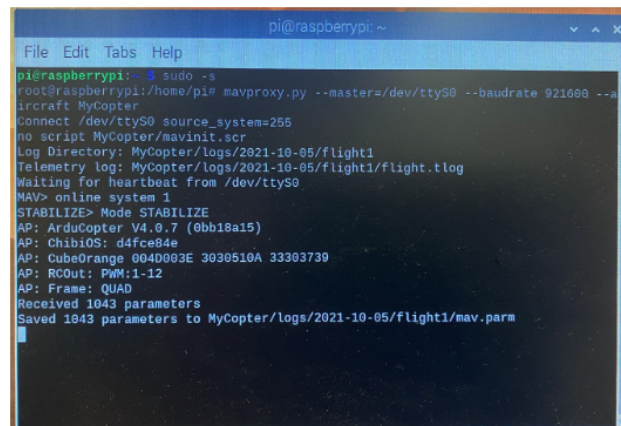
Sudo -s
pip3 install PyYAML mavproxy --user
echo "export PATH=$PATH:$HOME/.local/bin" >> ~/.bashrc

```

A MAVLink 2 connection can be established using MAVPROXY, by running:

```
Mavproxy.py --master=/dev/ttyS0 --baudrate 921600 --aircraft MyCopter
```

yielding the terminal output recorded in Fig. 6.14. The resulting terminal output confirms successful two-way communication between the onboard companion computer and the flight controller. Baud rate of the flight controller's applicable serial port can be set via the SERIAL2 baud rate parameter accessible by Mission Planner or QGroundcontrol.



```

pi@raspberrypi: ~
File Edit Tabs Help
pi@raspberrypi:~$ sudo -s
root@raspberrypi:~/home/pi# mavproxy.py --master=/dev/ttyS0 --baudrate 921600 --aircraft MyCopter
Connect /dev/ttyS0 source_system=255
no script MyCopter/mavinit.scr
Log Directory: MyCopter/logs/2021-10-05/flight1
Telemetry log: MyCopter/logs/2021-10-05/flight1/flight.tlog
Waiting for heartbeat from /dev/ttyS0
MAV> online system 1
STABILIZE> Mode STABILIZE
AP: ArduCopter V4.0.7 (0bb18a15)
AP: ChibiOS: d4fce84e
AP: CubeOrange 004D003E 3030510A 33303739
AP: RCOut: PWM:1-12
AP: Frame: QUAD
Received 1043 parameters
Saved 1043 parameters to MyCopter/logs/2021-10-05/flight1/mav.parm

```

Figure 6.14: Terminal output following successful MAVLink 2 connection to the flight controller using mavproxy

6.5.2.3 GPS Coordinates Acquisition

After establishing connection with the flight controller, MAVLink 2 enables the companion computer to request information using the MAVLINK Common Message Set. The messages of particular interest potentially containing location coordinates and time information are the GLOBAL_POSITION_INT, GPS_RAW_INT, and GPS_RAW_DATA. To request the content of these messages, a set of Python functions were written using the library pymavlink to connect to the flight controller, request a data stream of MAV_DATA_STREAM_POSITION yielding in the transmission of GLOBAL_POSITION_INT and LOCAL_POSITION messages from the flight controller, parse received messages, and return an array of 4 values comprised of the time since boot, latitude, longitude, and altitude. The main.py python program described in Section 6.5.1.5 calls these functions within the 1-second measurement streaming loop to associate the received TIPS spectra with GPS coordinates.

6.5.3 Raspberry Pi - Ground Station Communication

With data collection established from both the spectrometer and the flight controller, location-tagged measurement data can be synthesized and transmitted to the ground station computer (GCS) in real time.

6.5.3.1 Mosquitto Protocol

Live streaming of information from the onboard computer to the GCS requires a wireless connection and a data transmission protocol. This can be achieved either by transmission of data packets across the existing flight controller-GCS telemetry link using MAVLink routing, or using a separate network. For the purposes of maintaining telemetry signal strength and

simplified transmission of large (>1kB) data packets, data transmission over a separate network is favored. As Bluetooth is disabled on the companion computer in order to enable the use of two USB ports, a WiFi local area network (LAN) was identified as a readily accessible medium for communication.

A simple protocol for accomplishing machine-to-machine communication across a LAN is MQTT. The protocol is structured as a central MQTT broker with local and/or wireless clients. The broker serves to facilitate message routing from clients to their destinations. Communication is organized by message topics to which clients can publish and subscribe. Publishing a message to a topic transmits the message to all clients subscribed to the topic. In the sUAS-GCS configuration, the GCS serves as the MQTT broker as well as a subscriber to the measurement data stream topic. The sUAS' companion computer serves as a client publishing live messages in one-second intervals.

6.5.3.2 Transmitted Packet Structure

Packets generated by the data synthesis Python program are stored in plain-text files, each containing time information, location coordinates, and a TIPS spectrum of cumulative channel counts since acquisition start. The first 8 lines of each file contain the onboard computer clock time, the flight controller time since boot, latitude, longitude, altitude, and four lines of spectrometer metadata collected in conjunction with the received spectrum. Following the 8 header lines, the TIPS spectrum is contained in the ensuing 4096 rows (Fig. 6.15).

```
Raspberry Pi Time:1682550461.227
Pixhawk Time: 350589
Latitude: 379160343
Longitude: -1223381887
Altitude: 1830
100 0 33 32 0 0 64 0
156 19 116 39 0 0 0 0
83 3 0 0 30 0 0 0
0
0
0
...
```

Figure 6.15: Structure of assembled data packet depicting the header lines and initial three channels of a recorded TIPS spectrum

The data packets are saved locally on the onboard companion computer prior to being published by the Python program to an MQTT topic. At the end of each 1-second loop of the data streaming portion of the code, the command

```
publish.single("streamPSD", messageData, hostname = "192.168.0.114")
```

is run, publishing the packet data contained in “messageData” to the topic “streamPSD”.

6.5.3.3 Ground Station Data Processing

As the sUAS streams live measurement data packets to the “streamPSD” MQTT topic, the GCS simultaneously receives the streamed messages as a subscriber to “streamPSD”

Recording of the received MQTT messages is performed by execution of the bash script “save_mqtt_message.sh” using the command: `sudo bash save_mqtt_message.sh`

```
i=0
while true; do
  mosquitto_sub -C 1 -t streamPSD > msg"${i}".txt
  let i++;
done
```

In addition to saving each received MQTT message to an incremented file name during the measurement, a Python script was written to visualize the spectral data in tandem with data packet acquisition in real-time, named `live_plot_spectrum.py`:

```
import numpy as np
import matplotlib.pyplot as plt
import matplotlib.animation as animation
import pandas as pd

fig = plt.figure()
ax = fig.add_subplot(1,1,1)

def animate(i):
    data = pd.read_csv("spectrum.txt", skiprows=8)
    yar = data["0"]
    xar = range(len(yar))
    ax.clear()
    ax.plot(xar[:-1],yar[:-1])
    ax.set_xlabel("ADC Units")
    ax.set_ylabel("Counts")
    #ax.set_yscale('log')

ani = animation.FuncAnimation(fig, animate, interval=10)
plt.show()
```

Chapter 7

Measurements

In this Chapter, the detection and structural properties of two constructed sUAS prototype variants are demonstrated in laboratory and open-area source search experiments. Detection performance is evaluated in terms of PSD FOM in laboratory scenarios and source localization accuracy in field mapping scenarios. Initial field measurements were conducted using an extended-length structural PSD plastic scintillator component configuration, utilizing a 19 cm (7.5 inch) long structural component geometry to accommodate oversized 30 cm (12 inch) diameter propellers. The initial prototype geometry served to ensure sufficient thrust generation for demonstrating the proof-of-concept construction and operation of a payload-less sUAS.

Following a proof-of-concept demonstration using the extended-length detector component configuration sUAS, system dimensions were consolidated to construct a second prototype sUAS with an improved-upon configuration in terms of PSD. PSD capability was demonstrated in laboratory detector characterization, and structural component integration demonstrated in field testing of the improved design prototype system. Mitigation of signal interference, arising from the required consolidation of electronics to a minimal footprint, poses challenges in replicating laboratory-demonstrated PSD capability in field measurements. This can be overcome with refinement of the onboard electronics in regards to appropriate component selection, arrangement, and shielding.

7.1 Initial Prototype Field Measurements

The field measurements portion of this work was conducted to assess the feasibility of operating a payload-less radiation-detecting sUAS constructed of structural PSD plastic materials in a real-world deployment scenario. An initial prototype was constructed to demonstrate the proof-of-concept using scintillator frame arm components of increased length as compared to the optimal modeled detector geometry in Chapter 4.3, depicted in Fig. 7.1. The use of an extended frame configuration allows the sUAS to be outfitted with increased-diameter propellers to more easily generate thrust, provides greater in-flight stability, allows

for more generous spacing of onboard electronics. Due to the detector geometry of the initial constructed prototype, sufficient LCE to enable particle discrimination capability is not expected. In application of the GEANT4 model of Chapter 4 to the initial prototype detector geometry (Fig. 7.2), obtained mean LCE was 6.20%; 37.6% lower than the simulated mean LCE of the 100 cm long rectangular prism geometry (Chapter 4.2), which exhibited poor PSD capability experimentally. The larger detector volume, however, is predicted to provide advantages in the form of increased total detected counts.



Figure 7.1: Initial sUAS prototype consisting of 7.5-inch long structural PSD plastic scintillator frame component arms



Figure 7.2: GEANT4 model of initial sUAS prototype extended-length detector geometry

7.1.1 Setup and Configuration

Field measurements of the assembled initial prototype sUAS were performed at the University of California Richmond Field Station (RFS) in Richmond, CA.

Calibration of all onboard sensors was performed, including accelerometers, compasses, gyroscopes, level horizon, pressure, ESCs, motors, in advance of sUAS operation in guided-flight radiation mapping exercises. In addition, energy calibration was performed for the nanoPSD spectrometer and a 300keVee minimum signal pulse energy threshold set.

Each field measurement was conducted as a raster scan in an open field containing a mixed γ -n sources at a known location. A mission flight path over the area of interest was created in QGroundControl using Basic pattern feature of the survey pattern planning tool. Using this mode, waypoints are automatically generated across the designated measurement region in accordance with specified altitude, scan line spacing, and turnaround distance parameters (Fig. 7.3). Takeoff and waypoint altitudes are specified relative to launch altitude.

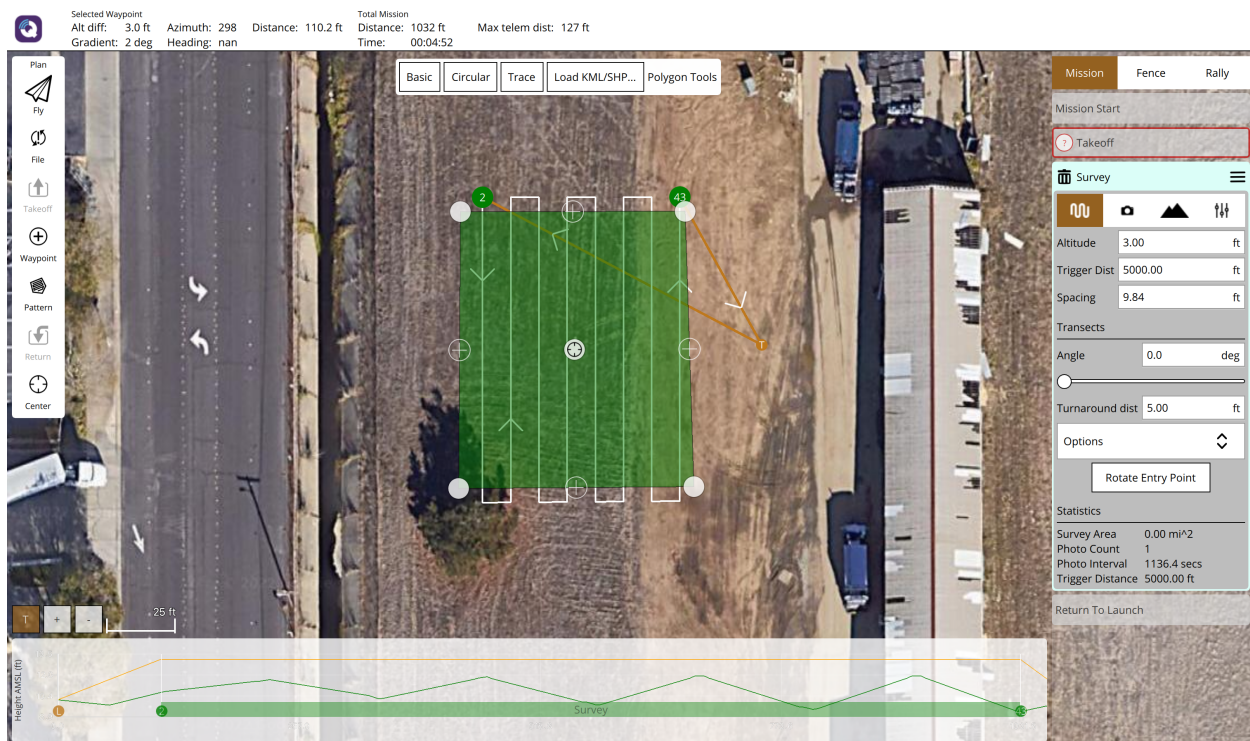


Figure 7.3: Screen capture of QGroundControl raster scan automatic course planning tool

7.1.2 Safety

In addition to sUAS electronics calibration, electronic safety features were specified to mitigate the consequences of system malfunctions in the event telemetry signal, power, course

adjustment, and/or critical sensor readings are compromised. The primary available safety feature for configuration is Return To Launch (RTL) behavior. The sUAS behavior in response to the RTL command consists of adjusting altitude to a specified value relative to the launch position, pursuing a straight-line course toward the launch position, and descent at a controlled rate. Specified in the Safety Setup tab prior to mission course planning, RTL altitude was set to an altitude of three meters, modified from the default setting of 15 meters.

In addition to RTL settings, a GeoFence was set to establish measurement area bounds to ensure the sUAS enters RTL mode in the scenario the sUAS travels outside the designated measurement area. The setting of this safety feature is vital for ensuring telemetry link is maintained between the sUAS and the GCS, in order to prevent loss of system control and the scenario of a “runaway” sUAS. For the field measurements, the GeoFence was established as a 30-meter radius from the GCS.

In the event of low battery charge, two battery failsafes were enabled: a low voltage threshold of 22.2V (3.7V per cell) triggering RTL mode, and a critical voltage threshold of 21V (3.5V per cell) triggering immediate controlled landing. Low-battery failsafes direct the sUAS to abort a mission when limited flight time remains, as well as protect its battery from irreversible damage due to excessive discharging.

For all other system malfunction scenarios, such as loss of telemetry connection, GPS positioning, and anomaly behavior, immediate controlled landing failsafe is specified.

7.2 Initial Prototype Field Measurement

The radiation mapping capability of the initial constructed prototype was evaluated by assessing the system’s performance in localizing a Pu-surrogate mixed source in the center of an open field at RFS. The source was positioned inside a white 5-gallon bucket 12.2 meters (40 feet) west of the sUAS launch position atop a 15” 5-gallon bucket (Fig. 7.4). A flight course was planned in QGroundControl to cover an approximate measurement area of 23 meters by 23 meters (75 feet by 75 feet) in a Raster pattern with 5 scan lines (passes). Flight altitude was set at 1.5 meters (5 feet) relative to ground height at the launch position and hover speed set to 3 miles per hour. The course plan was uploaded wirelessly to the sUAS flight controller.

An RTK base station was secured atop high-visibility traffic cone positioned nearby the GCS with an unobstructed view of the sky, connected to the GCS, and allowed to dial in its absolute position for 20 minutes. The obtained GPS accuracy following the 20-minute dial-in period was 3.9 feet (1.2 meters). Higher positioning accuracy is obtainable with longer dial-in periods, with potential for centimeter-level accuracy for 24+ hour dial-in times.

In addition to the RTK base station, a WiFi router was placed within the measurement space to provide a local area network (LAN) for data communication between the onboard computer and the GCS. Power was provided to the router from a car cigarette-plug adapter and a 15-meter (50 foot) extension cord. The range limits of the router were not investigated,

and the router was placed within the scan area to ensure signal strength. In more realistic hypothetical scenarios for which source location is not known a-priori, the router would be placed alongside the ground station computer, ideally with an unobstructed view of the sUAS.

Upon connection of the sUAS to its battery, all onboard electronics, including the detector circuits, are powered. To prevent brownouts from excessive start-up electrical load, the PSD spectrometer is switched off prior to system power-up, and switched on after onboard components have initialized. Upon power up, the onboard computer establishes a MQTT connection to the common data stream, and begins transmitting detected radiation spectrum packets to the GCS once per second. Following the receipt of received data packets by the GCS confirming the system is live, the autonomous flight plan was executed by arming the sUAS in Guided flight mode from the ground station computer.



Figure 7.4: Photo of initial prototype field measurement demonstrating the sUAS in flight, with locations depicted of the mixed γ -n source, launch position, LAN router, and RTK base station, from the visual perspective of the GCS.

7.2.1 Field Measurement Results

Following measurement, the packets transmitted to the ground station computer were plotted as a function of position to form a counts rate map (Fig. 7.5). Count rate data points were calculated by subtracting the TIPS spectrum counts of each one-second interval packet from the spectra obtained in the previous packet, yielding the newly detected counts. The newly-

detected counts per one-second interval were plotted as a function of GPS latitude and longitude, represented by color scale intensity.

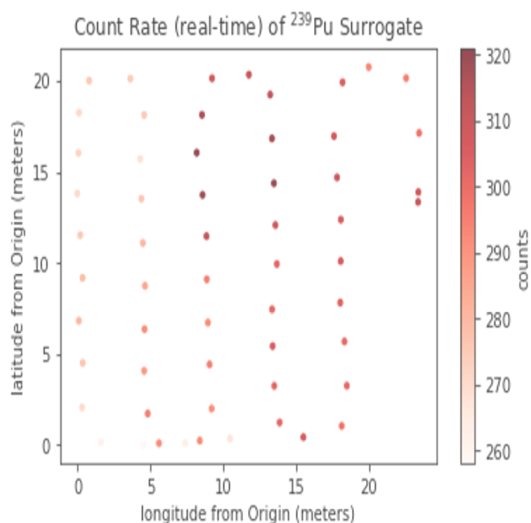


Figure 7.5: Plot of detected count rate with respect to relative coordinates position for one-second interval data packets collected during field measurement by constructed initial sUAS prototype

Superimposing the above count rates map over the original measurement path (Fig. 7.6) provides a preliminary visual indication of the system's proximity mapping capability (Fig. 7.7). Calculated newly-detected count rates are highest in the immediate region surrounding the true source location, with a reduction in count rate with increasing distance from the source. Noise in the distribution is apparent by occasional deviations from a continuous decrease in count rate as a function of source measurement distance. A discrepancy in detected counts rates is evident in between points to the east and west of the true source location, which may be attributed to the 1.2-meter altitude uncertainty of the recorded sUAS position.

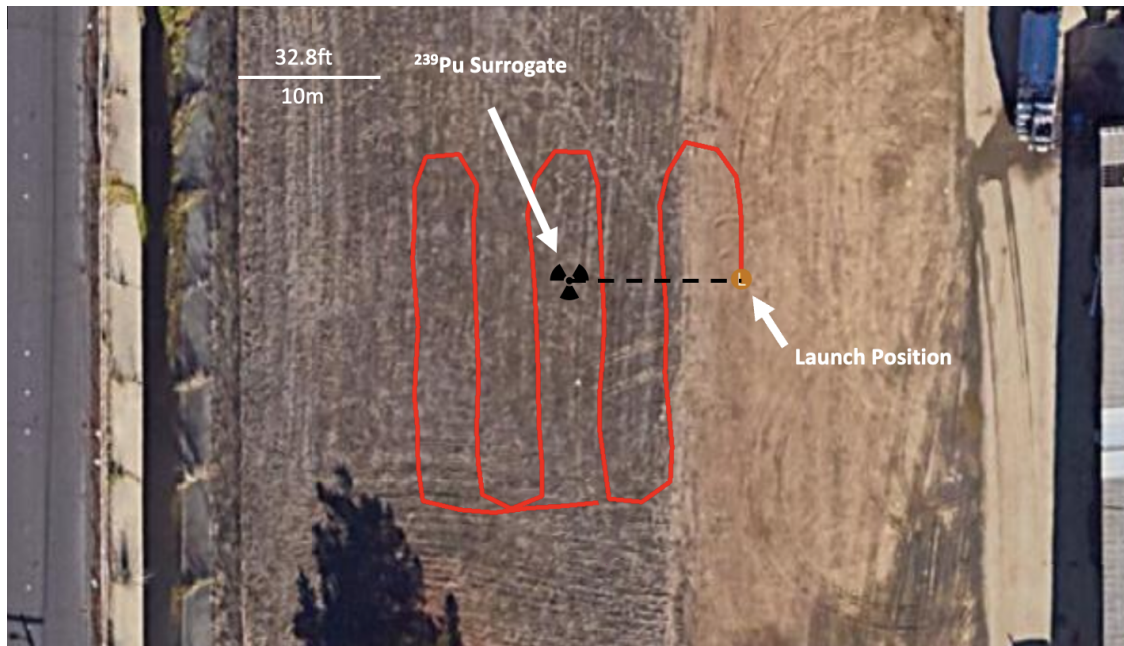


Figure 7.6: Screen capture of measurement path recorded by the sUAS flight controller

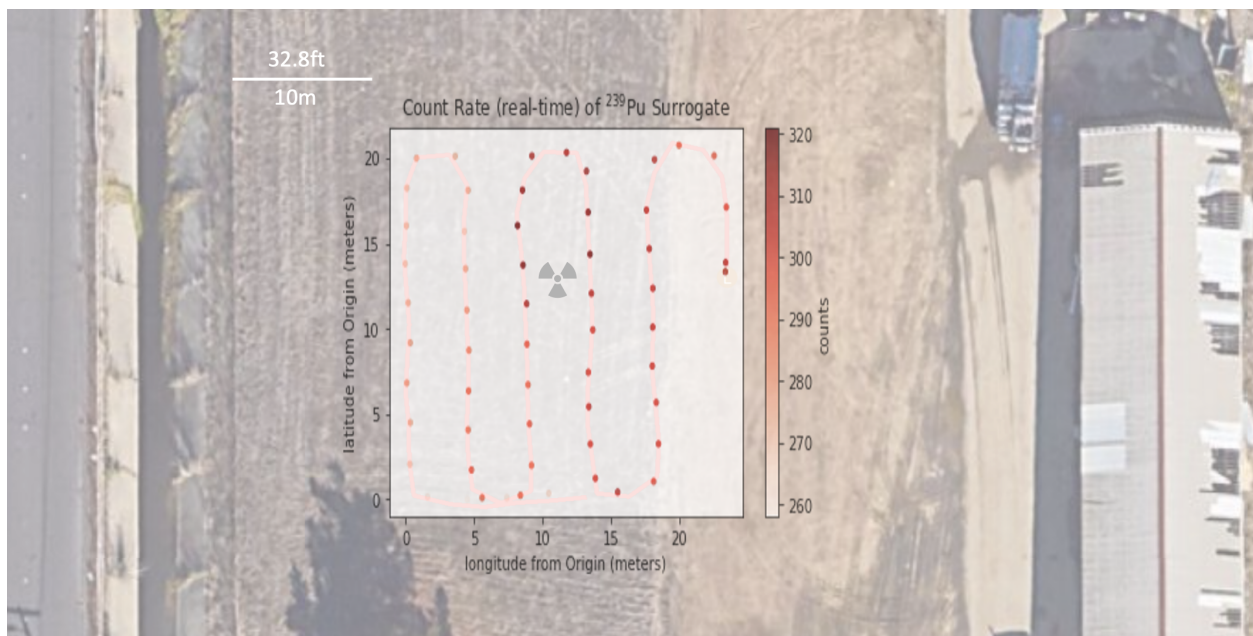


Figure 7.7: Fig. 7.5 overlaid onto 7.6, revealing a count rates distribution concentrated around the true source location

7.3 Analysis Techniques

Further analysis of the position-dependent count rates distribution was performed to investigate the viability of reconstructing source location using the collected data set. An initial attempt at source location reconstruction was made by applying a maximum likelihood expectation maximization (MLEM) algorithm to the distribution. Following 200 iterations, the algorithm was found to overfit reconstructed source locations to pixels following the measurement path, rather than the true source location (Fig. 7.8). A measurement dataset such as this, characterized by sparse sampling distributed over a large image field, presents an underdetermined system to which standard MLEM cannot be adequately applied. The result is a reconstructed image in which non-sampled regions, such as in between raster scan lines, are not considered to be probable source locations.

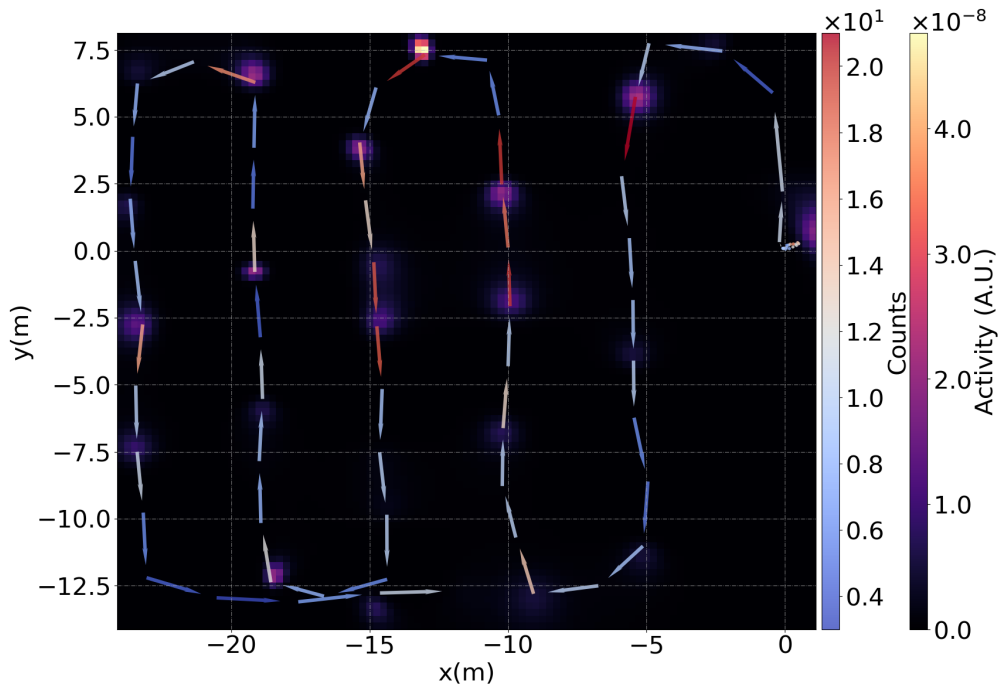


Figure 7.8: Standard MLEM reconstruction of measured position-dependent detected radiation counts by the sUAS. Multiple source hotspots along the measurement path are indicated by the colored pixel clusters. Measurement points are indicated by the directional vectors, colored by detected counts

To overcome this limitation, Kullback-Leibler (KL) divergence is implemented into the MLEM algorithm to modify individual pixel weights according to their probable contributions to the detected counts spatial distribution [44] [45]. The obtained reconstruction following 200 iterations is displayed in Fig. 7.9, depicting the most probable source location

as a singular source represented by the center highlighted pixels, as well as the detector's position vectors with associated signal intensity represented by the Counts colorbar. An attempt was made to reconstruct the source activity as denoted by the color of the reconstructed source pixels and the Activity colorbar. However, in the absence of detector response function characterizations, accurate absolute activity calculation could not be made.

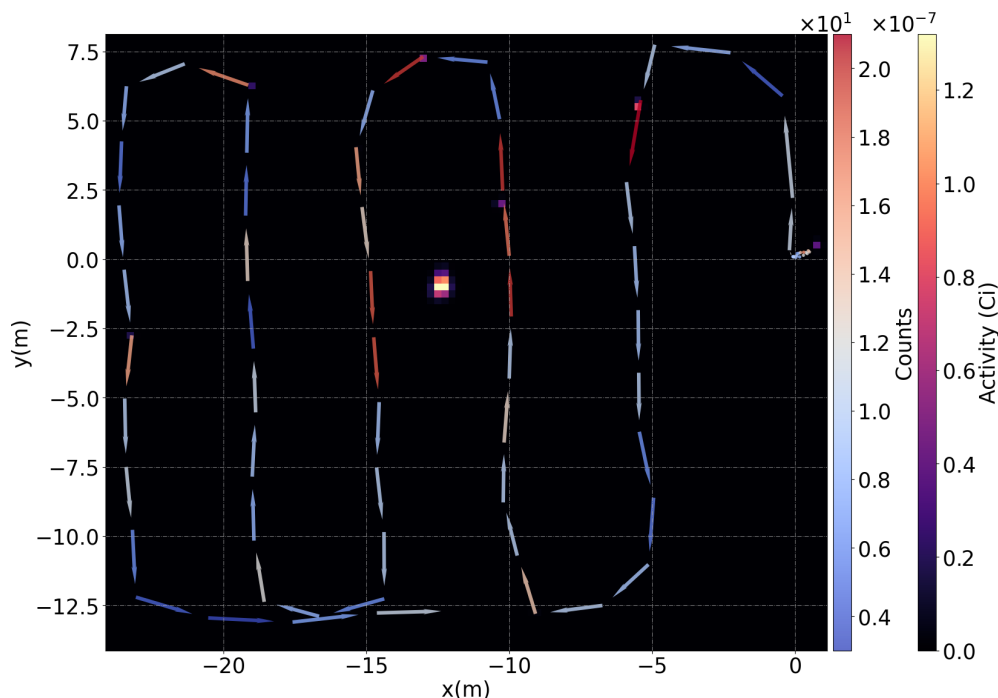


Figure 7.9: KL-divergence MLEM reconstruction of measured position-dependent detected radiation counts by the sUAS. A prominent source hotspot is indicated by the figure's center pixels. Measurement points are indicated by the directional vectors, colored by detected counts

7.4 Performance assessment

7.4.1 Initial Prototype

The radiation data obtained by the constructed prototype in the source search exercise is analyzed to assess the system's performance in aspects of both radiation mapping capability, as well as particle identification capability.

In regards to particle identification capabilities, TIPS spectra streamed by the sUAS did not exhibit distinct γ -ray and neutron histogram regions, and thus were not capable being fitted with separate Gaussian distributions to determine PSD FOM. For the cumulative

TIPS spectrum transmitted by the sUAS at the end of measurement, depicted in Fig. 7.10, the hypothetical PSD FOM is approximately zero, indicating PSD can not be performed for the detector configuration.

This lack of PSD capability is a result of a combination of multiple possible factors; the most significant of which, however, is the prototype’s suboptimal detector geometry in terms of LCE. The employed prototype detector geometry, consisting of structural scintillators 7.5 inches in length, is not conducive to efficient scintillation photon transport to the tapered photon collection site at the scintillator end. This initial prototype sUAS component geometry, while suboptimal for detection, was employed to ensure sufficient thrust generation accommodating larger-diameter 12-inch propellers.

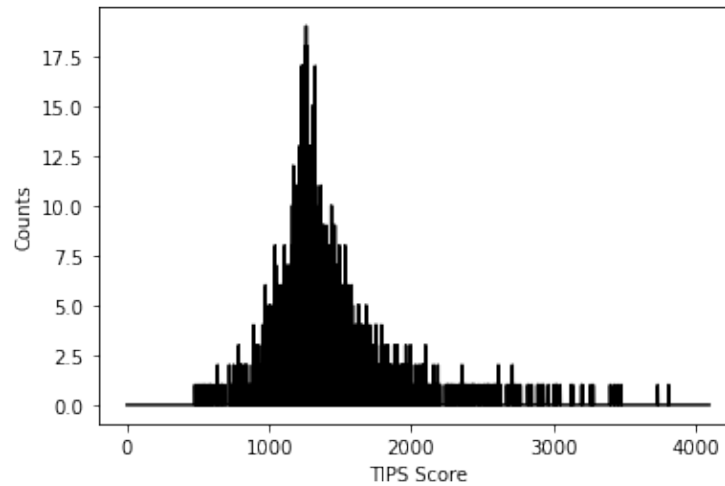


Figure 7.10: Cumulative TIPS spectrum streamed by prototype sUAS at the conclusion of field measurement exercise, indicating lack of separation between γ -ray and neutron TIPS differences

To assess the system’s radiation mapping performance, the results of the reconstruction can be interpreted in a meaningful real-world context by overlaying the reconstructed source pixel map onto an image indicating the original measurement course and the true source location. (Fig. 7.11). Removing the reconstruction plot axes and movement vectors reveals a simplified map comparing the reconstructed source location to the true source location (Fig. 7.12).

As indicated by the overlaid reconstruction map, the source location predicted by applying the KL divergence algorithm to the sUAS’ collected data is one meter (3.2 feet) north of the true source position. In reference to the GNSS horizontal position uncertainty of 1.2 meters (3.9 feet), this result demonstrates successful source localization capability of the system within its positional uncertainty limits.

As mentioned previously, the GNSS position resolution was obtained for this measurement following a dial-in time of 20 minutes during measurement setup. Reduced position uncertainty can be achieved by implementing longer system dial-in times, with resolution as low as 1cm potentially obtainable for RTK base station dial-in times greater than 24 hours. This approach may be appropriate for scenarios demanding high positional accuracy, such as long-term radioactivity distribution mapping of stable environments. For the conducted exercise, an initial setup time of 20 minutes demonstrates the system's rapid deployment capability for use in time-sensitive scenarios, such as in incident response. Using the initial constructed prototype and a dial-in time of 20 minutes, the total measurement time necessary to localize a source to within one meter of its true location in a search area of 625 m^2 was 2 minutes and 1 second.

Although acquired measurement data packets were recorded in real time by the GCS, analysis of the position-dependent radiation data was performed using algorithms in post processing, following the data acquisition measurements. While development and implementation of real-time algorithms for source localization, including adaptive search and multi-unit communication (swarm intelligence), were not pursued, the live streaming of sUAS data demonstrates the capability for their future implementation.

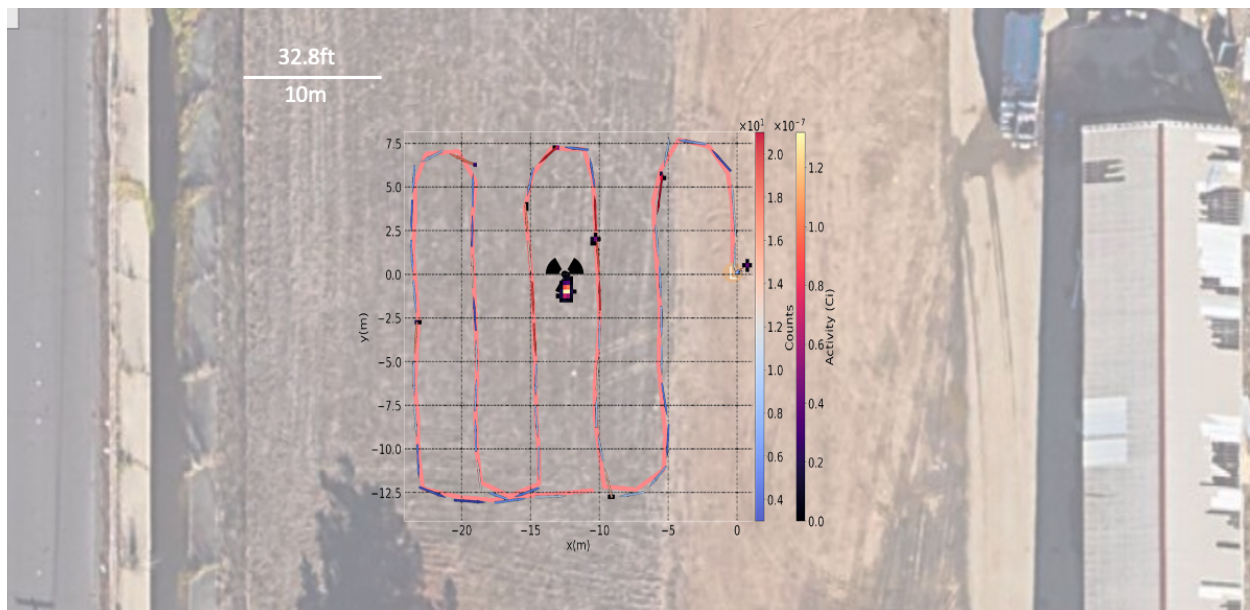


Figure 7.11: Reconstruction of measured source location predicted by KL-divergence MLEM overlaid onto the measurement flight path plotted on a 2D satellite image of the measured space. The true source location is indicated by the trefoil



Figure 7.12: Overlaid comparison of the reconstructed source location pixels to the true source location indicated by the trefoil, reference to the measurement path line in red

The results of the field exercise demonstrate the successful operation of a system constructed of structural PSD plastic scintillators, achieving source localization capability through proximity mapping. Thus, in order to accomplish the remaining task of accomplishing PSD capability for an implemented structural component, modifications were required to be made to the initial sUAS prototype design in order to increase LCE and consequently the SNR. Most prominently, these modifications involve shortening of the detector component geometry while maintaining sufficient thrust generation with the required incorporation of reduced propeller diameters.

7.5 Second-Generation Prototype

The design of an improved sUAS prototype achieving PSD centers about shortening of the structural PSD plastic component frame arms, from a length of 19 cm (7.5 inches), to a length of 11.4 cm (4.5 inches). This alteration consequently requires modifications of other aspects of the sUAS design. Shortening of frame dimensions restricts maximum propeller diameter, requiring powerful motors and/or changes to propeller pitch and blade number (at the cost of efficiency). In addition, reduction of overall structural detector mass demands the optimization of non-scintillating components in order to maintain 50% active mass utilization.

Incorporating these principles, mass-saving improvements to the sUAS design were implemented. The primary changes include reduction of the frame arms' center mounting components' masses, migration from the use of four individual ESCs and a PDB to a single four-in-one ESC (described in Chapter 5.3.1), replacement of the onboard Raspberry Pi model 3 B+ by a Raspberry Pi Zero model 2 W, migration from a 4-cell (14.8V nominal) a 6-cell (22.2V nominal) LiPo battery, and the use of 20 cm (8 inches) diameter propellers. Component arrangement modifications include repositioning of the GNSS from a standalone mast to atop the flight controller, in response to the reduced available physical system footprint. The second-generation sUAS design is depicted visually in the exploded component diagram of Fig. 7.13.

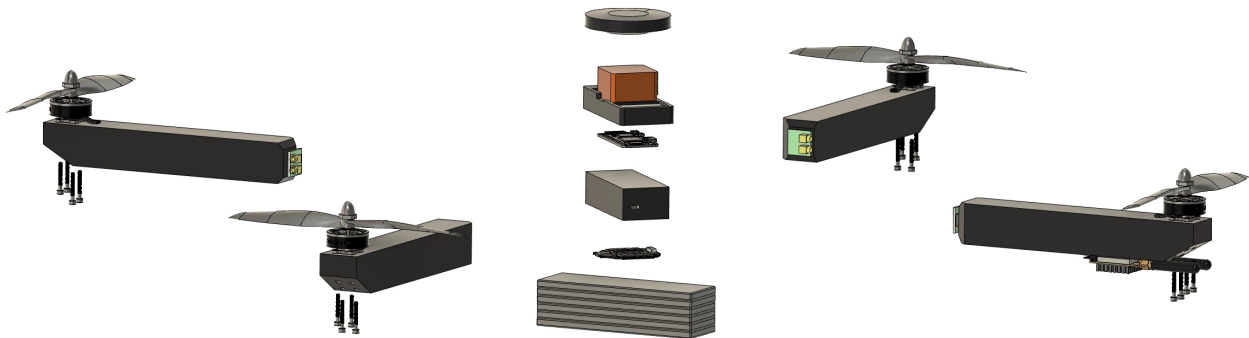


Figure 7.13: CAD exploded component diagram of second-generation structural PSD plastic scintillator sUAS configuration

In incorporating these modifications, total system dry weight was reduced from 1968 grams to 1280 grams. The system's active mass utilization is slightly below the target 50%, at 47%. Further reduction of non-scintillating system mass can be accomplished by the replacement of higher-cost electronics with components of reduced mass, such as the flight controller, GNSS, and the metal PSD spectrometer housing, accounting for approximately 200 grams. The constructed second-generation sUAS is photographed executing a guided (autonomous) flight mission shortly after takeoff, with the 14-inch Macbook Pro GCS for scale, in Fig. 7.14.



Figure 7.14: Photograph of second-generation sUAS prototype, composed of 4.5-inch structural PSD plastic frame arm components, in guided flight

7.5.1 Laboratory measurements

Prior to field testing, PSD capability of the constructed structural scintillator component geometry was characterized in a controlled laboratory measurement environment. Measurement configurations included component PSD characterization as conducted for the model validation geometries of Chapter 4.2, with signals routed to a Struck SIS3316 digitizer module, and as a fully assembled system with signals routed to the onboard labZY nanoPSD real-time PSD spectrometer. Following laboratory measurements, field tests commenced, with experimental measurements and data analysis in tandem with prototype refinements ongoing at the time of writing.

7.5.1.1 Procedure

In advance of sUAS assembly, the constructed structural arm geometry was characterized using the experimental setup established for characterizing the GEANT4 model validation geometries in Chapter 4.2. PSD measurements were performed for uncollimated source configurations using $1\mu\text{Ci}$ ^{137}Cs and ^{22}Na calibration γ -ray sources, and a 0.5 mCi γ -n ^{252}Cf source (0.25 mCi activity at time of measurement).

The sUAS was then assembled and its detection performance benchmarked in the laboratory prior to field operation. Two experimental conditions were evaluated, consisting of a source placed 12 inches (30.5cm) below the center of the sUAS with the sUAS powered on and disarmed, and with the sUAS armed with 50% throttle applied to the motors. The sec-

ond arrangement serves to emulate the noise environment representative of the sUAS hover conditions during flight, i.e., generating a thrust:mass ratio of 1.

It is noted that for the experimental setup involving live motor operation, a FlySky FS-IA6B receiver module with two antennas was added to the sUAS electronics stack to enable manual operation using a joystick FS-i6X transmitter, which may contribute to increased signal noise. This additional modification was implemented in order to bypass guided mode flight failsafes, triggered by the flight controller in response to potential thrust loss upon sensed increased current load for a stationary system.

Twenty-minute measurements of ^{137}Cs and ^{22}Na sources were performed, and used to calibrate the nanoPSD spectrometer. A 300 keVee low-energy threshold was applied for TIPS calculation. Sources were placed at a distance of 12 inches from the sUAS center. Following calibration, one-minute measurements were conducted of ^{252}Cf at a distance of 12 inches from the sUAS center, with lead shielding 4 inches thick placed in between the sUAS and the ^{252}Cf source to equalize the proportion of detected γ -ray and neutron radiation particle interactions. Measurements were repeated for the scenarios of an idle sUAS followed an sUAS armed and 50% motor throttle applied. The sUAS frame was secured in place to two lead bricks using velcro straps (Fig. 7.15).



Figure 7.15: Laboratory PSD characterization setup for assembled sUAS

7.5.1.2 Results

The laboratory measurement results of the sUAS component arm prior to assembly demonstrate a PSD FOM of 1.164 was achieved for detected interactions within the 475 ± 75 keVee energy region. While not fully meeting the FOM metric of 1.27 for 99% γ -ray and neutron particle discrimination confidence, clear separation exists between the two particle-respective tail pulse fraction regions of the generated PSD plot (Fig. 7.16). Particle separation threshold curves can still be established for the obtained data, albeit at a reduced confidence level. The results obtained in this laboratory environment can be used as a benchmark of the PSD performance for the constructed system, to assess the degree of signal degradation observed by operating the sUAS arm in an assembly.

In comparison to the PSD evaluation results of the GEANT4 model validation geometries of Chapter 4.2.1, the PSD FOM achieved by the structural scintillator component geometry is most comparable the PSD FOM of the 45° tapered model validation shape. In comparison, measured PSD FOM is 3.0% higher for the sUAS component, despite a scintillator geometry of 12.5% increased overall length. A comparison of the measured ^{137}Cs calibration spectrum to one predicted by the GEANT4 model of Chapter 4 is displayed in Fig. 7.17, demonstrating the GEANT4 model correctly predicts the experimentally-observed Compton edge.

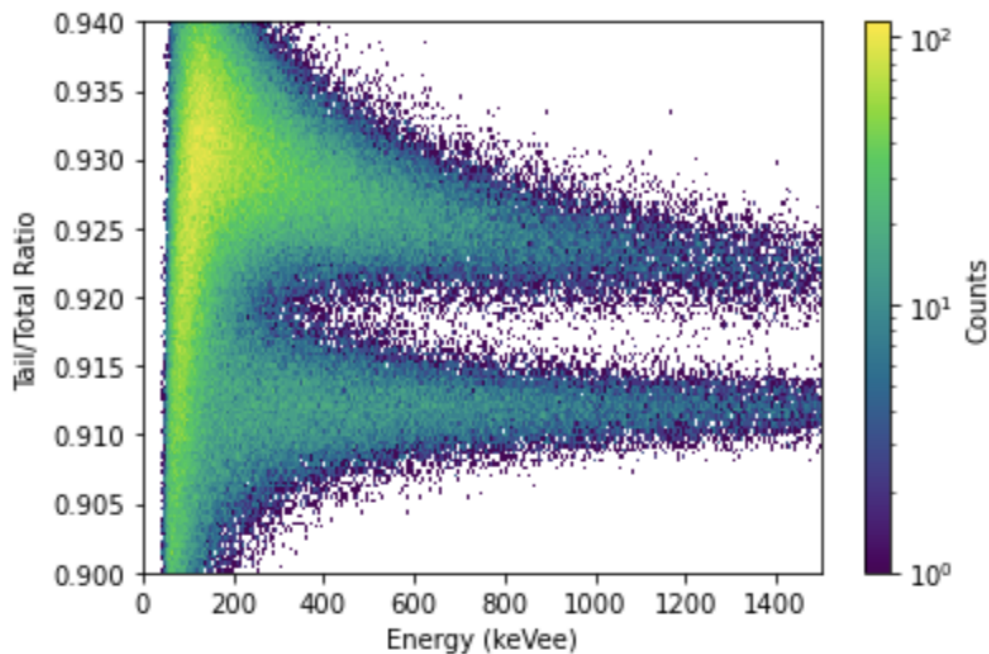


Figure 7.16: PSD plot of sUAS component arm prior to system assembly

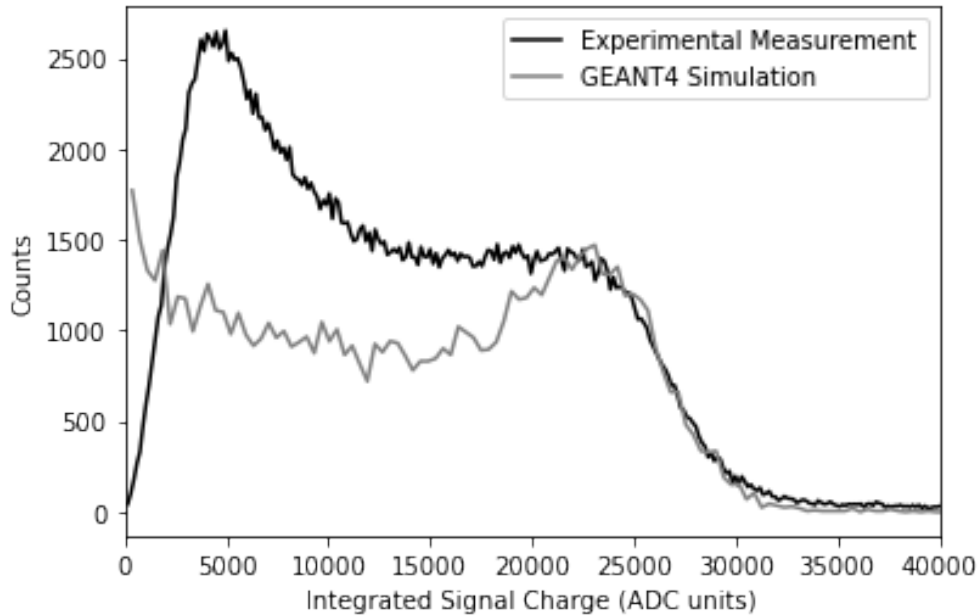


Figure 7.17: Comparison of simulated and experimental detected energy spectra of uncollimated incident 661.7 keV γ -rays

The sUAS arm's PSD FOM may potentially be improved by the expansion of the motor bolt hole diameters to provide clearance for additional PTFE reflector layers, painting of the motor bolts with a reflective paint, such as Eljen EJ-510, prior to wrapping with PTFE tape, or by the application of more aggressive tapers, which may potentially affect the structural integrity of the component or its mounting.

The sUAS was then assembled, and characterized for PSD in the laboratory. TIPS histograms were recorded using the onboard spectrometer and used to calculate PSD FOM. The obtained histograms for recorded signal pulses in the two described measurement configurations - disarmed and armed with 50% applied motor throttle, are plotted in Fig. 7.18. Despite the spectrometer possessing a built-in FOM calculation feature, FOM was calculated by applying Gaussian fits to the distribution, in order to maintain consistency in FOM determination method. Acquired FOM values for the two sUAS measurement configurations were 1.03 when disarmed, and 1.02 when armed with motors under 50% power.

These results indicate operation of the structural sUAS detector components in the noise environment expected aboard the sUAS during flight is not expected to significantly affect their particle identification capabilities. The demonstration of a negligible difference in FOM between disarmed and powered conditions in the laboratory confirm the consolidated sUAS design successfully maintains SiPM signal collection and pulse processing integrity onboard.

Nevertheless, obtained PSD FOM values aboard the assembled sUAS are lower than the measured PSD FOM for standalone component characterization measurements in the

laboratory. A portion of this discrepancy is attributed to the different energy bounds set by the onboard nanoPSD spectrometer (>300 keVee) and the Struck digitizer (475 ± 75 keVee). The current nanoPSD is limited to 2D FOM determination, meaning different measurements must be taken in order to determine FOM For different energy regions. In order to record as many usable counts as possible during measurements, a lower energy threshold of 300 keVee was set for the system. Further optimization of the nanoPSD’s calibrated signal energy thresholds can be performed by PSD measurement of different energy region “slices” to determine the system’s PSD FOM energy-dependence relationship, using which a low-energy threshold can be set to yield a desired particle discrimination confidence level.

A pulse energy threshold matching the energy threshold set for the nanoPSD was applied to the data of Fig. 7.16, yielding a calculated PSD FOM value of 1.10. While reduced in magnitude, a discrepancy between the onboard- and laboratory-achieved FOM values remains. Factors which may be responsible for the remaining difference may be a result of differences in the applied calibration curves, a performance differential between the tail pulse fraction and TIPS PSD methods, or increased bias and/or readout noise aboard the sUAS.

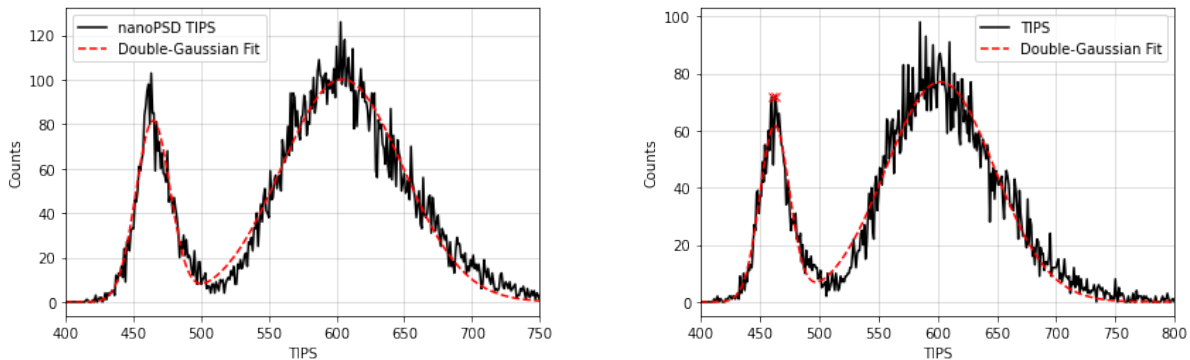


Figure 7.18: Comparison of Gaussian-fitted TIPS spectra for laboratory measurements of ^{252}Cf for disarmed sUAS (left) and armed sUAS with applied 50% motor throttle (right)

7.6 Discussion

Using the two constructed sUAS prototypes, proximity radiation mapping capability is demonstrated in a source search exercise by the initial extended-length detector component configuration. Source localization accuracy of 1 meter within a 625 m^2 search area is achieved using the constructed device, accomplished in a measurement time of 2 minutes.

Separately, the PSD capability of the second fabricated prototype’s structural scintillator component geometry is evaluated in laboratory measurements, yielding a PSD FOM of 1.164 at 475 ± 75 keVee. While not meeting the established FOM threshold for 3σ particle

discrimination confidence, PSD can nevertheless be conducted either at a reduced confidence level or for higher interaction energy thresholds.

The structural integrity of the sUAS frame was experimentally demonstrated for both systems in test flights and field measurement scenarios. Both systems endured multiple crashes, with no discernible damage to the radiation-detecting frame. Objectively, however, the second-generation sUAS configuration proved to be more resilient due to the greater durability of its smaller (8-inch) diameter propellers. In the aftermath of crash scenarios, the second prototype was able to be returned to the launch position and re-launched to resume the planned measurement course in all encountered cases, while crashes involving the extended-length frame configuration and its 12-inch diameter propellers necessitated the replacement of broken propellers in a large fraction of cases. While the cost of replacing propellers is minimal, the capacity to do so may be limited in real-world deployment scenarios.

By the time of writing, reliable field measurement data could not be collected for the second prototype as a result of necessary system refinements which remain to be implemented. Of these, extensive measures to reduce SiPM signal noise were accomplished, yielding similar PSD FOM values for disarmed and under-power conditions in the laboratory. Prior to these refinements, the system prototype exhibited a throttle-dependent reduction in accumulated spectrum counts when armed, to the extent of counts no longer being detected at 50% applied motor power. This behavior was attributed to the response of the spectrometer's automatic noise threshold adjustment, and ultimately resolved by eliminating a prevailing ground loop causing distortions to readout of the weak SiPM analog current signals.

Remaining points of refinement involve ensuring onboard sensors accuracy and overall system stability. The consolidated electronics footprint onboard and the relatively large coefficient of drag for a system of its size consequently require precise tuning of parameters to ensure smooth motor response to internal sensor readings. The majority of crashes experienced during self-guided mission flights were a result of incorrect noisy sensor readings and/or incorrect adjustment to the perceived system orientation, resulting in inconsistent flight altitudes. It should be noted that in a number of cases, the sUAS flight controller demonstrated successful crash recovery following impact with soft objects, such as tall brush and uneven ground.

Following the resolution of these issues, future planned flights to simultaneously demonstrate both the source localization and particle discrimination capabilities of the second constructed prototype will consist of source search exercises involving two separate sources - one γ -ray and one lead-shielded mixed γ -ray and neutron source - in close proximity. Analysis of measurement data will seek to evaluate the system's performance in localizing sources according to their distinct particle signatures within an expansive search area.

Chapter 8

Concluding Remarks

The outcome of this work is the demonstrated feasibility of using a new generation of organic scintillation detectors - PSD plastic scintillators - as structural components with radiation detection capabilities. A large range of PSD plastic scintillator compositions, with and without ^6Li -doping to enable tri-modal particle detection sensitivity, was systematically evaluated to determine composition-specific PSD capabilities and mechanical tensile strength and stiffness properties. Characterized properties were compared across different composition types and used to guide the development of novel scintillator compositions with enhanced mechanical strengths. The conclusions of the study identify that current difficulties in fabricating mechanically-robust ^6Li -doped PSD plastic scintillators can be overcome, while maintaining PSD capability, by the addition of a modest proportion (up to 10%) of poly-methacrylic acid (PMAA) to polystyrene scintillator base. In tested compositions, measured mechanical strength increased proportionally with added PMAA content beyond 10%, up to a yield strength of 61.02 MPa for 69:31 PS:PMAA scintillator base proportions, however at the cost of particle discrimination capability. Satisfactory particle discrimination capability for this work was defined as FOM > 1.27 for signal pulses of 475 ± 75 keVee energy deposition; the characteristic energy region of ^6Li thermal neutron capture interactions.

For this composition type, the effect of scintillator curing temperature and duration conditions was additionally investigated, suggesting a tradeoff relationship in which mechanical stiffness was found to have benefited from elevated curing temperatures and durations, while PSD FOM was observed to be reduced. Compositions not containing ^6Li were generally observed to possess tensile yield strengths above the computer-simulated minimum sUAS external component strength threshold of 30 MPa, with PS:PMAA compositions exhibiting higher strengths and reduced PSD FOM as compared to PS and PS:PMMA (poly-methyl methacrylate) compositions.

Using the identified structurally-viable material compositions, two proof-of-concept small unmanned aerial systems (sUASs) were constructed to demonstrate the potential for the development of new classes of mobile radiation-detecting systems enabled by these novel materials. By the incorporation of radiation-detecting structural scintillators serving the sUAS frame, the conventionally-necessary distinction between carrier vehicle and detection

payload was successfully eliminated in the deployed compact payload-less sUAS prototypes. Scintillator component geometries were optimized for scintillation photon collection efficiency using experimentally-validated GEANT4 simulations, demonstrating that a structurally-serving sUAS component geometry, incorporating motor mounting bolt holes drilled into the active volume, can accomplish a PSD FOM of 1.164 at 475 ± 75 keVee by strategic tapering of the scintillator volume.

Structural scintillator sUAS frame components were hand-fabricated from received bulk material as informed by simulation, and paired to an electronics suite providing self-guided flight control capability with real-time wireless streaming of position-tagged γ -ray and neutron PSD spectra. Source localization by proximity for a 0.25mCi mixed γ -n source using the initial constructed sUAS prototype - of 48 cm diameter and 2 kg mass - was successfully accomplished to within one meter by a two-minute measurement of a 625 m² search area. The PSD capability of these materials, while fulfilling a structural role, was demonstrated in the laboratory using a second constructed sUAS prototype of reduced component dimensions of 30 cm diameter and 1.3 kg mass, with structural integrity demonstrated separately in field tests. Future experiments evaluating the system's performance in localization exercises of distinct γ -ray and neutron signatures remain to be performed.

The development of novel PSD-capable structural scintillator materials coupled with their successful incorporation in a payload-less radiation-detecting sUAS, as demonstrated by this work, signify the potential of these materials to enable new technological development in the field of radiation detection. The creation of highly compact, payload-less aerial radiation detection systems bring forth novel capabilities, from backpack-transportable deployable units to economical multi-unit swarm configurations, expands the arsenal of tools available for radiation mapping and ultimately the protection of human lives from preventable exposure to unknown radiation hazards.

Bibliography

- [1] N. Zaitseva, B. L. Rupert, I. Pawełczak, A. Glenn, H. P. Martinez, L. Carman, M. Faust, N. Cherepy, and S. Payne, “Plastic Scintillators with Efficient Neutron/Gamma Pulse Shape Discrimination,” *Nucl. Instrum. Methods Phys. Res., Sect. A*, vol. 668, pp. 88–93, 2012, ISSN: 0168-9002. DOI: <https://doi.org/10.1016/j.nima.2011.11.071> (cit. on pp. 2, 7, 12).
- [2] O. Klitting, F. Sguerra, G. H. Bertrand, V. Villemot, and M. Hamel, “Preparation and characterization of cross-linked plastic scintillators,” *Polymer*, vol. 213, p. 123 214, 2021, ISSN: 0032-3861. DOI: <https://doi.org/10.1016/j.polymer.2020.123214>. [Online]. Available: <https://www.sciencedirect.com/science/article/pii/S0032386120310399> (cit. on pp. 2, 19).
- [3] S. Moser, W. Harder, C. Hurlbut, and M. Kusner, “Principles and practice of plastic scintillator design,” *Radiation Physics and Chemistry*, vol. 41, no. 1, pp. 31–36, 1993, ISSN: 0969-806X. DOI: [https://doi.org/10.1016/0969-806X\(93\)90039-W](https://doi.org/10.1016/0969-806X(93)90039-W). [Online]. Available: <https://www.sciencedirect.com/science/article/pii/0969806X9390039W> (cit. on p. 6).
- [4] Photomultiplier tubes and assemblies for scintillation counting high energy physics, TPMZ0003E01, Hamamatsu Photonics K.K., Apr. 2017 (cit. on p. 8).
- [5] Silicon photomultipliers, high pde and timing resolution sensors in a tsv package, MICROJSERIES/D, Rev. 7, Onsemi, Aug. 2021 (cit. on pp. 8, 51, 74).
- [6] G. F. Knoll, Radiation Detection and Measurement, en. John Wiley & Sons, Aug. 2010 (cit. on p. 10).
- [7] C. Awe, P. Barbeau, A. Haghghat, S. Hedges, T. Johnson, S. Li, J. Link, V. Mascolino, J. Runge, J. Steenis, T. Subedi, and K. Walkup, “Measurement of proton quenching in a plastic scintillator detector,” *Journal of Instrumentation*, vol. 16, no. 02, P02035–P02035, Feb. 2021. DOI: 10.1088/1748-0221/16/02/p02035. [Online]. Available: <https://doi.org/10.1088/1748-0221/16/02/p02035> (cit. on p. 11).
- [8] C. Bass, E. Beise, H. Breuer, C. Heimbach, T. Langford, and J. Nico, “Characterization of a 6Li-loaded liquid organic scintillator for fast neutron spectrometry and thermal neutron detection,” *Applied Radiation and Isotopes*, vol. 77, pp. 130–138, 2013, ISSN: 0969-8043. DOI: <https://doi.org/10.1016/j.apradiso.2013.03.053>.

- [Online]. Available: <https://www.sciencedirect.com/science/article/pii/S0969804313001437> (cit. on p. 11).
- [9] N. J. Cherepy, R. D. Sanner, P. R. Beck, E. L. Swanberg, T. M. Tillotson, S. A. Payne, and C. R. Hurlbut, “Bismuth- and lithium-loaded plastic scintillators for gamma and neutron detection,” *Nucl. Instrum. Methods Phys. Res., Sect. A*, vol. 778, pp. 126–132, 2015, ISSN: 0168-9002. DOI: <https://doi.org/10.1016/j.nima.2015.01.008>. [Online]. Available: <https://www.sciencedirect.com/science/article/pii/S0168900215000261> (cit. on p. 11).
- [10] J. BIRKS, in *The Theory and Practice of Scintillation Counting*, ser. International Series of Monographs in Electronics and Instrumentation, J. BIRKS, Ed., Pergamon, 1964, pp. 39–67, ISBN: 978-0-08-010472-0. DOI: <https://doi.org/10.1016/B978-0-08-010472-0.50008-2>. [Online]. Available: <https://www.sciencedirect.com/science/article/pii/B9780080104720500082> (cit. on p. 12).
- [11] N. Zaitseva, L. Carman, A. Glenn, R. Hatarik, S. Hamel, B. Rupert, M. Faust, B. Schabes, N. Cherepy, and S. Payne, “Pulse shape discrimination in impure and mixed single-crystal organic scintillators,” *IEEE Transaction on Nuclear Science*, vol. 58, no. 6, pp. 3411–2420, Nov. 2011. DOI: [10.1109/TNS.2011.2171363](https://doi.org/10.1109/TNS.2011.2171363). [Online]. Available: <https://www.osti.gov/biblio/1183547> (cit. on p. 12).
- [12] A. Hristova, E. Vapirev, L. Tsankov, and V. Jordanov, “Compton edge energy calibration of organic detectors,” *International Journal of Radiation Applications and Instrumentation. Part A*, vol. 41, no. 9, pp. 887–889, 1990, ISSN: 0883-2889. DOI: [https://doi.org/10.1016/0883-2889\(90\)90068-R](https://doi.org/10.1016/0883-2889(90)90068-R). [Online]. Available: <https://www.sciencedirect.com/science/article/pii/088328899090068R> (cit. on p. 18).
- [13] V. T. Jordanov, “Pile-up real time pulse-shape discrimination based on ballistic deficit measurement and digital time-invariant pulse shaping,” in *IEEE NSS/MIC Proceedings*, 2018, pp. 1–5. DOI: [10.1109/NSSMIC.2018.8824502](https://doi.org/10.1109/NSSMIC.2018.8824502) (cit. on p. 19).
- [14] N. Zaitseva, A. Mabe, M. Carman, A. Glenn, J. Inman, and S. Payne, “Plastic scintillators stable for operating in wide ranges of humidity and temperature variations,” *Nucl. Instrum. Methods Phys. Res., Sect. A*, vol. 954, p. 161 709, 2020, Symposium on Radiation Measurements and Applications XVII, ISSN: 0168-9002. DOI: <https://doi.org/10.1016/j.nima.2018.12.024>. [Online]. Available: <https://www.sciencedirect.com/science/article/pii/S0168900218318217> (cit. on p. 19).
- [15] M. Loyd, M. Pianassola, C. Hurlbut, K. Shipp, N. Zaitseva, M. Koschan, C. L. Melcher, and M. Zhuravleva, “Accelerated aging test of new plastic scintillators,” *Nucl. Instrum. Methods Phys. Res., Sect. A*, vol. 949, p. 162 918, 2020, ISSN: 0168-9002. DOI: <https://doi.org/10.1016/j.nima.2019.162918>. [Online]. Available: <https://www.sciencedirect.com/science/article/pii/S0168900219313257> (cit. on p. 19).

- [16] C. Redding, A. Hackett, M. Laubach, R. Feng, P. Feng, C. Hurlbut, P. Liaw, and J. P. Hayward, “Tensile, flexural, and light output measurements of selected organic scintillators for evaluation of their potential as structural materials,” *NIM Phys. Res., Sect. A*, vol. 954, p. 161448, 2020, Symposium on Radiation Measurements and Applications XVII, ISSN: 0168-9002. DOI: <https://doi.org/10.1016/j.nima.2018.10.126>. [Online]. Available: <https://www.sciencedirect.com/science/article/pii/S0168900218314402> (cit. on p. 20).
- [17] V. Baranov, Y. Davydov, R. Erasmus, C. Kureba, N. Lekalakala, T. Masuku, J. Mdhluli, B. Mellado, G. Mokgatitswane, E. Sideras-Haddad, I. Vasilyev, and P. Zhmurin, “Effects of neutron radiation on the optical and structural properties of blue and green emitting plastic scintillators,” *Nucl. Instrum. Methods Phys. Res., Sect. A*, vol. 436, pp. 236–243, 2018, ISSN: 0168-583X. DOI: <https://doi.org/10.1016/j.nimb.2018.10.002>. [Online]. Available: <https://www.sciencedirect.com/science/article/pii/S0168583X18305834> (cit. on p. 20).
- [18] H. Jivan, J. Mdhluli, E. Sideras-Haddad, B. Mellado, R. Erasmus, and M. Madhuku, “Radiation damage effects on the optical properties of plastic scintillators,” *Nucl. Instrum. Methods Phys. Res., Sect. B*, vol. 409, pp. 224–228, 2017, Proceedings of the 20th International Conference on Ion Beam Modification of Materials (IBMM 2016), ISSN: 0168-583X. DOI: <https://doi.org/10.1016/j.nimb.2017.05.061>. [Online]. Available: <https://www.sciencedirect.com/science/article/pii/S0168583X17306602> (cit. on p. 20).
- [19] M. Mizue Hamada, P. Roberto Rela, F. Eduardo da Costa, and C. Henrique de Mesquita, “Radiation damage studies on the optical and mechanical properties of plastic scintillators,” *Nucl. Instrum. Methods Phys. Res., Sect. A*, vol. 422, no. 1, pp. 148–154, 1999, ISSN: 0168-9002. DOI: [https://doi.org/10.1016/S0168-9002\(98\)01091-2](https://doi.org/10.1016/S0168-9002(98)01091-2). [Online]. Available: <https://www.sciencedirect.com/science/article/pii/S0168900298010912> (cit. on p. 20).
- [20] MatWeb. (2023). “Aluminum 2024-t3,” [Online]. Available: <https://www.matweb.com/search/DataSheet.aspx?MatGUID=57483b4d782940faaf12964a1821fb61> (visited on 07/17/2023) (cit. on p. 24).
- [21] —, (2023). “Overview of materials for acrylonitrile butadiene styrene (abs), extruded,” [Online]. Available: <https://www.matweb.com/search/DataSheet.aspx?MatGUID=3a8afcddac864d4b8f58d40570d2e5aa> (visited on 07/17/2023) (cit. on p. 24).
- [22] —, (2023). “Overview of materials for nylon 66, 30% glass fiber filled,” [Online]. Available: <https://www.matweb.com/> (visited on 07/17/2023) (cit. on p. 24).
- [23] —, (2023). “Overview of materials for nylon 66, 30% carbon fiber filled,” [Online]. Available: <https://www.matweb.com/search/datasheet.aspx?matguid=04c04b1466a24becb9f66a9404c4c37a> (visited on 07/17/2023) (cit. on p. 24).

- [24] —, (2023). “G-10 fiberglass epoxy laminate sheet,” [Online]. Available: <https://www.matweb.com/> (visited on 07/17/2023) (cit. on p. 24).
- [25] R. Pavlovsky, J. W. Cates, W. J. Vanderlip, T. H. Y. Joshi, A. Haefner, E. Suzuki, R. Barnowski, V. Negut, A. Moran, K. Vetter, and B. J. Quiter, “3d gamma-ray and neutron mapping in real-time with the localization and mapping platform from unmanned aerial systems and man-portable configurations,” 2019. arXiv: 1908.06114 [physics.ins-det] (cit. on p. 24).
- [26] J. ELDER, K. MA, and S. MANDOT, “Building radiation detecting drones using scintillating material,” https://funginstitute.berkeley.edu/wp-content/uploads/2020/05/ProjectBrief_RadiationDetectingDrone_Final_2019-20.pdf, May 2020 (cit. on pp. 24, 25).
- [27] J. ELDER and K. MA and S. MANDOT, “Building Radiation-Detecting Drones Using Scintillating Materials,” May 2020 (cit. on p. 26).
- [28] N. Zaitseva, A. Glenn, M. Carman, A. Mabe, S. Payne, N. Marom, and X. Wang, “Multiple dye interactions in plastic scintillators: Effects on pulse shape discrimination,” *Nucl. Instrum. Methods Phys. Res., Sect. A*, vol. 978, p. 164455, 2020, ISSN: 0168-9002. DOI: <https://doi.org/10.1016/j.nima.2020.164455>. [Online]. Available: <https://www.sciencedirect.com/science/article/pii/S0168900220308524> (cit. on p. 27).
- [29] Psd plastic scintillator ej-276d ej-276g, ELJEN TECHNOLOGY, Dec. 2022 (cit. on p. 50).
- [30] F. Sutanto, T. Classen, S. Dazeley, M. Duvall, I. Jovanovic, V. Li, A. Mabe, E. Reedy, and T. Wu, “SANDD: A directional antineutrino detector with segmented 6li-doped pulse-shape-sensitive plastic scintillator,” *Nucl. Instrum. Methods Phys. Res., Sect. A*, vol. 1006, p. 165409, Aug. 2021. DOI: [10.1016/j.nima.2021.165409](https://doi.org/10.1016/j.nima.2021.165409). [Online]. Available: <https://doi.org/10.1016/j.nima.2021.165409> (cit. on p. 50).
- [31] A. Mabe, personal communication, May 6, 2020 (cit. on p. 50).
- [32] McMaster-Carr. (2022). “High-density thread sealant tape,” [Online]. Available: <https://www.mcmaster.com/6802K87/> (visited on 11/17/2022) (cit. on p. 51).
- [33] Tie-31: Mechanical and thermal properties of optical glass, SCHOTT AG, Jul. 2004 (cit. on p. 51).
- [34] N. Das, “F450 quadcopter,” Accessed 08-11-2023, [Online]. Available: <https://grabcad.com/library/f450-quadcopter-2> (cit. on p. 59).
- [35] Avenger v3 2812-1115kv-6s-60a-hq 8x4.5x3 test report, BrotherHobby, 2022. [Online]. Available: <https://www.brotherhobbystore.com/avenger-2812-v3-motorcw-p0112.html> (cit. on p. 72).

- [36] Handling and soldering of onsemi tsv packaged sipm sensors, AND9793/D, ONSEMI, Aug. 2021. [Online]. Available: <https://www.onsemi.com/pub/Collateral/AND9793-D.PDF> (cit. on p. 84).
- [37] Readout methods for arrays of silicon photomultipliers, AND9778/D, ONSEMI, Sep. 2018. [Online]. Available: <https://www.onsemi.com/pub/Collateral/AND9778-D.PDF> (cit. on p. 84).
- [38] Signal driven multiplexing of silicon photomultiplier arrays, AND9772/D, Semiconductor Components Industries, LLC, Aug. 2018. [Online]. Available: <https://www.onsemi.com/pub/Collateral/AND9772-D.PDF> (cit. on p. 84).
- [39] Cdc7630/7631 and ddc2353/2354 series: Zero bias silicon schottky barrier detector diodes, Skyworks Solutions, Inc., Sep. 2014. [Online]. Available: https://www.mouser.com/datasheet/2/472/CDC_and_DDC_Series_Schottky_Diodes_200843I-1076471.pdf (cit. on p. 85).
- [40] V. T. Jordanov, G. F. Knoll, A. C. Huber, and J. A. Pantazis, “Digital techniques for real-time pulse shaping in radiation measurements,” *Nucl. Instrum. Methods Phys. Res., Sect. A*, vol. 353, no. 1, pp. 261–264, 1994, ISSN: 0168-9002. DOI: [https://doi.org/10.1016/0168-9002\(94\)91652-7](https://doi.org/10.1016/0168-9002(94)91652-7). [Online]. Available: <https://www.sciencedirect.com/science/article/pii/0168900294916527> (cit. on p. 86).
- [41] Software user manual labzy-psd versions 2.50 to 2.99, labZY (cit. on p. 87).
- [42] Open communication labzy firmware versions 30.19, 30.20, labZY (cit. on pp. 92, 93).
- [43] Fpga registers standard labzy fpga designs, labZY (cit. on p. 93).
- [44] J. Lee, R. Cooper, T. Joshi, and K. Vetter, “Single Detector 3D Source Imaging Using a Kullback-Leibler Divergence Based Prior,” in 2021 IEEE NSS/MIC, Oct. 2021 (cit. on p. 108).
- [45] J. Lee, “Extended radiological source mapping in 3d with single detector using a gaussian random field prior,” *IEEE NSS MIC Milan*, Nov. 2022 (cit. on p. 108).